CONTRIBUTIONS TO RADIO FREQUENCY INDOOR POSITIONING AND THROUGH-THE-WALL MAPPING

Rafael Saraiva Campos

Tese de Doutorado apresentada ao Programa de Pós-graduação em Engenharia Elétrica, COPPE, da Universidade Federal do Rio de Janeiro, como parte dos requisitos necessários à obtenção do título de Doutor em Engenharia Elétrica.

Orientadores: Marcello Luiz Rodrigues de Campos
Lisandro Lovisolo

Rio de Janeiro
Junho de 2017

CONTRIBUTIONS TO RADIO FREQUENCY INDOOR POSITIONING AND THROUGH-THE-WALL MAPPING

Rafael Saraiva Campos

TESE SUBMETIDA AO CORPO DOCENTE DO INSTITUTO ALBERTO LUIZ COIMBRA DE PÓS-GRADUAÇÃO E PESQUISA DE ENGENHARIA (COPPE) DA UNIVERSIDADE FEDERAL DO RIO DE JANEIRO COMO PARTE DOS REQUISITOS NECESSÁRIOS PARA A OBTENÇÃO DO GRAU DE DOUTOR EM CIÊNCIAS EM ENGENHARIA ELÉTRICA.

Examinada por:

Prof. Marcello Luiz Rodrigues de Campos, Ph.D.

Prof. Lisandro Lovisolo, D.Sc.

Prof. Eduardo Antônio Barros da Silva, Ph.D.

Prof. João César Moura Mota, D.Sc.

Prof. Maurício Henrique Costa Dias, D.Sc.

RIO DE JANEIRO, RJ – BRASIL
JUNHO DE 2017

Campos, Rafael Saraiva

Contributions to Radio Frequency Indoor Positioning and Through-the-Wall Mapping/Rafael Saraiva Campos. – Rio de Janeiro: UFRJ/COPPE, 2017.

XXIII, 131 p.: il.; 29, 7cm.

Orientadores: Marcello Luiz Rodrigues de Campos
Lisandro Lovisolo

Tese (doutorado) – UFRJ/COPPE/Programa de Engenharia Elétrica, 2017.

Referências Bibliográficas: p. 121 – 131.

1. Machine Learning. 2. Radio Frequency Fingerprinting. 3. Multi-Floor Positioning. 4. Situational Awareness. 5. Finite Element Method. 6. Through-the-Wall Mapping. I. Campos, Marcello Luiz Rodrigues de *et al.* II. Universidade Federal do Rio de Janeiro, COPPE, Programa de Engenharia Elétrica. III. Título.

Agradecimentos

Agradeço aos meus orientadores, Prof. Dr. Marcello Luiz Rodrigues de Campos e Prof. Dr. Lisandro Lovisolo, pelo apoio e confiança. Em especial ao meu amigo Prof. Lisandro, que me resgatou do mundo corporativo há 10 anos, e desde então tem ajudado a conduzir minha vida acadêmica.

"...nunca sabemos o que há atrás da porta..."
Major PM Valmor Saraiva Racorte
Comandante do GATE (Grupo de Ações Táticas Especiais)

Resumo da Tese apresentada à COPPE/UFRJ como parte dos requisitos necessários para a obtenção do grau de Doutor em Ciências (D.Sc.)

CONTRIBUIÇÕES À LOCALIZAÇÃO INDOOR E AO MAPEAMENTO ATRAVÉS DE PAREDES UTILIZANDO RADIOFREQUÊNCIA

Rafael Saraiva Campos

Junho/2017

Orientadores: Marcello Luiz Rodrigues de Campos
Lisandro Lovisolo

Programa: Engenharia Elétrica

A primeira parte deste trabalho introduz um novo sistema de localização baseado em aprendizado de máquina para aumentar a acurácia da identificação do andar na localização em prédios baseada em radiofrequencia (RF), enquanto preserva-se baixo o erro de localização bidiminensional. O método também reduz a complexidade computacional do cálculo da estimativa de posição. Um banco de dados de amostras de RF foi coletado em um prédio com 13 andares para avaliar a proposta. A segunda parte deste trabalho analisa o imageamento tomográfico não-invasivo utilizando RF, ou mapeamento através de paredes (TWM - *Through-the-Wall Mapping*). Quatro algoritmos de reconstrução – dois projetivos e dois algébricos – são comparados utilizando um modelo de perda de propagação corrompido por ruído Rayleigh em uma geometria de aquisição com feixes de raios paralelos. Em seguida, a tese propõe a aplicação do método dos elementos finitos (FEM - *Finite Element Method*) para simular diversas configurações de TWM, proporcionando um modelo de simulação mais acurado. Os parâmetros da discretização (*meshing*) do modelo FEM foram otimizados, reduzindo significativamente o custo computacional, sem comprometer a acurácia. A reconstrução de duas plantas-baixas é realizada empregando diferentes taxas de amostragem, frequências de operação e modelos de antena. Por fim, uma geometria de aquisição circular com múltiplos sensores (MCG - *Multi-Sensor Circular Acquisition Geometry*) é definida para reduzir o tempo de obtenção de amostras de RF em comparação com a geometria de raios paralelos. O esquema MCG é avaliado utilizando o modelo FEM proposto.

Abstract of Thesis presented to COPPE/UFRJ as a partial fulfillment of the requirements for the degree of Doctor of Science (D.Sc.)

CONTRIBUTIONS TO RADIO FREQUENCY INDOOR POSITIONING AND THROUGH-THE-WALL MAPPING

Rafael Saraiva Campos

June/2017

Advisors: Marcello Luiz Rodrigues de Campos
Lisandro Lovisolo

Department: Electrical Engineering

The first part of this work introduces a novel machine-learning based location engine aiming at improving floor identification accuracy in radio frequency (RF) multi-floor indoor positioning while preserving a low two-dimensional positioning error. The location engine also reduces the position fix computational complexity. A large database of RF samples was collected in a 13-storey building to evaluate the proposal. The second part of this work studies in detail radio tomographic imaging, also referred to as RF-based through-the-wall mapping (TWM). Four different reconstruction algorithms – two projective and two algebraic – are compared using a path-loss model corrupted by Rayleigh noise in a parallel-beam acquisition geometry. After that, the thesis proposes applying the Finite Element Method (FEM) to simulate several parallel-beam geometry RF TWM setups, providing a more accurate simulation model. The meshing parameters of the FEM model geometry have been optimized, enabling a significant computational cost reduction while preserving accuracy. Reconstruction of two floor maps is carried out using the FEM model with different sampling rates, operational frequencies, and antenna models. Finally, a multi-sensor circular acquisition geometry (MCG) is defined to reduce the time required to acquire the RF samples in comparison to the parallel-beam geometry. The MCG scheme is evaluated using the proposed FEM framework.

Contents

List of Figures

List of Tables

List of Symbols

$\Delta\rho$	Inter-sample distance in TWM parallel-beam geometry, p. 68
$\Delta\theta$	Angular step in TWM parallel-beam geometry, p. 59
$\Delta\xi$	Angular step in TWM multi-sensor circular acquisition geometry, p. 108
Δ_b	Multipath fading (dB) relative to the mean received power, p. 67
$\Gamma(\cdot)$	Computational complexity function, p. 31
$\alpha_i(\rho_j, \theta_k)$	Attenuation factor (dB/m) across the ith obstacle along the line defined by (ρ_j, θ_k), p. 64
β_{offset}	Propagation loss (dB) at d_0 meters from the transmitter, p. 65
β_{slope}	Path loss exponent or slope (dB/decade), p. 65
δ	Relaxation parameter in iterative algebraic reconstruction techniques, p. 63
ϵ_0	Electric permittivity of vacuum, p. 82
ϵ_r	Relative permittivity (dielectric constant), p. 82
$\hat{f}(x, y)$	Reconstructed floor map, p. 59
κ	Computational complexity reduction factor, p. 40
κ_{max}	Theoretical maximum computational complexity reduction factor, p. 39
λ	Carrier wavelength, p. 85
μ_0	Magnetic permeability of vacuum, p. 82
μ_r	Relative permeability, p. 82

ω	Angular frequency (rad/s), p. 82
$\overline{\mathrm{RSS}}_k$	kth AP mean RSS level considering all measurement points, p. 37
$\overline{\mathrm{RSS}}_{i,k}$	kth AP mean RSS level at the ith measurement point, p. 36
ϕ_i	Phase of the ith received multipath component, p. 18
$\psi_i(t)$	Learning step of the ith synapse at iteration t, p. 38
ρ	Radon transform radial coordinate, p. 57
ρ_s	Surface charge density ($\mathrm{C/m^2}$), p. 83
σ	Electrical conductivity (S/m), p. 82
τ_i	Delay of the ith received multipath component, p. 18
θ	Radon transform angular coordinate, p. 57
$\vec{\mathbf{B}}$	Magnetic flux density vector (Wb), p. 83
$\vec{\mathbf{D}}$	Electric flux density vector (C), p. 83
$\vec{\mathbf{E}}$	Electric field vector (V/m), p. 82
$\vec{\mathbf{H}}$	Magnetic field vector (A/m), p. 82
$\vec{\mathbf{K}}$	Surface current density (A/m), p. 83
$\mathcal{F}_n$	n-dimensional DFT operator, p. 60
$\mathcal{F}_n^{-1}$	n-dimensional inverse DFT operator, p. 60
S_0	Receiver sensitivity (dBm), p. 66
$\mathrm{S}_{\mathrm{Int},k}$	Total internal dispersion of the kth cluster, p. 38
$\mathrm{S}_{\mathrm{Int}}$	Total internal dispersion of the data set, p. 39
$\mathbf{G}$	Sinogram matrix, p. 60
$\mathbf{P}$	Principal Components Matrix, p. 37
$\mathbf{R}$	Zero-mean shifted input vectors matrix, p. 37
$\mathbf{u}_j$	jth eigenvector of the covariance matrix of $\mathbf{R}$, p. 37
$\mathbf{f}$	RF fingerprint, p. 27

$\mathbf{h}_j$	CIR to the impulse transmitted by the jth AP, p. 18
$\mathbf{m}_k$	Arithmetic mean of the elements in the kth cluster, p. 38
$\mathbf{w}_i$	Synaptic weight of the ith neuron in a Kohonen layer, p. 34
$f(x, y)$	Floor map, p. 57
C_{PCA}	Complexity factor of RF fingerprints comparison in the PCA space, p. 31
C_{RSS}	Complexity factor of RF fingerprints comparison in the RSS space, p. 31
$G(\mathrm{f}, \theta)$	Fourier Transform of a Radon projection taken at angle θ, p. 58
G_r	Receiver antenna gain (dBi), p. 65
G_t	Transmitter antenna gain (dBi), p. 65
$L_{\max}$	Maximum supportable over-the-air path loss (dB), p. 66
L_d	Propagation loss (dB) at d meters from the transmitter, p. 65
L_r	Cable and connection losses at the receiver (dB), p. 64
L_t	Cable and connection losses at the transmitter (dB), p. 64
N_{Tfing}	Number of Tfings, p. 39
N_a	Number of ANNs per committee, p. 35
N_c	Number of clusters, p. 31
N_k	Number of Rfings int the kth cluster, p. 31
N_l	Number of floors, p. 35
N_p	Number of Rfings in the CDB, p. 28
N_w	Number of WiFi networks, p. 27
P_r	Mean received power (dBm), p. 64
P_t	Mean transmitted power (dBm), p. 64
a_i	Amplitude of the ith received multipath component, p. 18
d_0	Reference distance in an offset-slope propagation model, p. 13

$g(\rho, \theta)$	Radon transform, p. 57
g_l^v	Output of the majority voting committee of the lth floor, p. 36
$g_{\max}$	Maximum detectable shadowing loss (dB), p. 66
$g_{j,l}$	Output of the jth binary classifier at the committee of the lth floor, p. 35
$l_i(\rho_j, \theta_k)$	Length (m) of the ith obstacle along the line defined by (ρ_j, θ_k), p. 64
n_i	Number of elements in the cluster which the ith Tfing was associated with, p. 40
p_i	Percentage of the ith neuron training, p. 38
u_i	Similarity measure between an input vector and $\mathbf{w}_i$, p. 34
$w_{i,0}$	Conscience bias of the ith neuron in a Kohonen layer, p. 34
f	Spatial frequency, p. 58

List of Abbreviations

1-D	One-Dimensional, p. 58
2-D	Two-Dimensional, p. 12
3-D	Three-Dimensional, p. 28
ANN	Artificial Neural Network, p. 17
AOA	Angle-of-Arrival, p. 7
AP	Access Point, p. 6
ART	Algebraic Reconstruction Technique, p. 58
BGM	Bayesian Graphic Model, p. 49
CDB	Correlation Database, p. 8
CDF	Cumulative Distribution Function, p. 42
CID	Cell Identity, p. 6
CIR	Channel Impulse Response, p. 17
CTF	Channel Transfer Function, p. 17
CTI	Computerized Tomographic Imaging, p. 55
CTS	Clear-to-Send, p. 20
CW	Continuous Wave, p. 80
DCM	Database Correlation Method, p. 7
DFR	Direct Fourier Reconstruction, p. 58
DFT	Discrete Fourier Transform, p. 18
EIRP	Effective Isotropic Radiated Power, p. 66

FBR	Filtered Backprojection Reconstruction, p. 58
FCF	Frequency Coherence Function, p. 17
FEM	Finite Element Method, p. 80
FIR	Finite impulse response, p. 97
FLD	Fisher's Linear Discriminant, p. 50
FT	Fourier Transform, p. 58
GNSS	Global Navigation Satellite System, p. 6
GPS	Global Positioning System, p. 23
HPBW	Half-power beamwidth, p. 98
IAP	Intersection of Access Points, p. 15
IDFT	Inverse Discrete Fourier Transform, p. 18
KNN	K-Nearest Neighbors, p. 10
LBS	Location-based System, p. 1
LOP	Line-of-Position, p. 7
LOS	Line-of-Sight, p. 10
MAC	Medium Access Control, p. 20
MCG	Multi-Sensor Circular Acquisition Geometry, p. 107
MLP	Multi-Layer Perceptron, p. 26
MOS	Mean Opinion Score, p. 70
MSE	Mean Squared Error, p. 41
MSSIM	Mean SSIM, p. 71
MS	Mobile Station, p. 6
NLOS	Non-Line-of-Sight, p. 7
NNSS	Nearest Neighbor in the Signal Space, p. 12
PARDISO	Parallel sparse direct linear solver, p. 81

PCA	Principal Components Analysis, p. 26
PC	Principal Component, p. 31
PDEs	Partial differential equations, p. 81
RAN	Radio Access Network, p. 9
RFID	Radio Frequency Identification, p. 14
RF	Radio Frequency, p. 6
RH	Relative Humidity, p. 15
RSS	Received Signal Strength, p. 7
RTD	Round-Trip-Delay, p. 7
RTS	Request-to-Send, p. 20
RTT	Round-Trip-Time, p. 20
Rfing	Reference Fingerprint, p. 9
SIRT	Simultaneous Iterative Reconstruction Technique, p. 58
SLAM	Simultaneous Localization and Mapping, p. 55
SSID	Service Set Identifier, p. 28
SSIM	Structural Similarity Index, p. 71
TDOA	Time Difference of Arrival, p. 7
TWM	Through-the-Wall Mapping, p. 54
TWRI	Through-the-Wall Radar Imaging, p. 54
Tfing	Target Fingerprint, p. 9
UAP	Union of Access Points, p. 15
UHF	Ultra-High Frequency, p. 55
WAF	Wall Attenuation Factor, p. 13
WLAN	Wireless Local Area Network, p. 6
WiFi	Wireless Fidelity, p. 1
w-KNN	Weighted K-Nearest Neighbors, p. 18

Chapter 1

Introduction

This introductory chapter clarifies the motivations driving the development of this thesis, as well as its main contributions. The chapter also presents the thesis structure and lists our related publications.

1.1 Motivations

1.1.1 Improving Floor Identification Accuracy in WiFi Indoor Positioning

There is a growing number of Mobile Stations (MS) equipped with built-in Global Positioning System (GPS) receivers. In open areas, GPS yields the highest location precision, but is usually unavailable in indoor environments. In this scenario, Received Signal Strength (RSS) based location techniques are used both in cellular and Wireless Fidelity (WiFi) networks [1]. In cellular mobile telephony, indoor positioning might rely on the reception of signals from indoor micro or even pico-cells, or from outdoor cells with strong indoor reception [2]. However, the increasingly denser deployment and availability of WiFi access points (APs), coupled with the fact that most mobile devices today are WiFi enabled, makes the use of WiFi signals a preferable choice for indoor positioning, in comparison to cellular mobile telephony signals [3].

When implementing or using a location-based system (LBS) for indoor positioning, one may not be troubled by small planar errors. For example, suppose that one is in a garage or mall, if the LBS estimates or indicates that an object or MS is within three or five meters from its actual location, this error may be acceptable. However, if the LBS reports that one is on the wrong floor this may not be acceptable at all, mostly due to the fact that buildings are built in such a way that it is much easier to move within the same floor than among floors.

From the above, it becomes evident that the most critical issue in WiFi indoor positioning is floor identification in multi-storey buildings. Surprisingly, only a minority of papers address this subject. Therefore, improving floor identification accuracy, while preserving a low two-dimensional positioning error, became the main motivation of the first part of this thesis.

1.1.2 Improving Tactical Situation Awareness in Critical Conditions in Indoor Environments

Situation awareness in a tactical level is the perception of environmental variables, in time and space, and the ability to understand and interrelate them, as a basis for quick decision making in crisis intervention [4]. Situation awareness in critical conditions – such as search-and-rescue, hostage situations and military urban operations – can be improved by non-invasive techniques that enable locating unspecific moving targets behind walls using reflected RF signals (TWRI – Through-the-Wall Radar Imaging) and obtaining the blueprint of a floor before entering it, using transmitted RF signals (TWM – Through-the-Wall Mapping). However, unlike TWRI, there are very few papers addressing TWM applications [5–8]. Therefore, TWM became the focus of the second part of this thesis.

1.2 Contributions

1.2.1 Contributions to RF Indoor Positioning

This thesis proposes a novel machine learning-based location engine for multi-floor indoor positioning. The location engine combines unsupervised and supervised learning and a database correlation method to improve floor identification accuracy, while maintaining the in-floor two-dimensional positioning error low. The proposal is evaluated through an experiment conducted in a 13-floor building, where the proposed localization scheme achieved floor identification accuracies ranging from 91% to 97%, with mean two-dimensional positioning errors spanning from 3.5 to 1.1 meters. A comprehensive literature review on the theme was conducted, so that the achieved results could be compared with those of other published methods.

1.2.2 Contributions to RF Through-the-Wall Mapping

This thesis carries out a detailed comparative analysis of four reconstruction techniques than can be applied to through-the-wall mapping problems (Filtered Backprojection Reconstruction, Direct Fourier Reconstruction, Algebraic Reconstruction

Technique and Simultaneous Iterative Reconstruction Technique), all of them originally used in computerized X-ray tomography. This analysis uses two simulation models: a path-loss model corrupted by Rayleigh noise to account for static multipath reception and a finite element-based model. A metric for image quality assessment is tentatively selected to allow an objective comparison of the reconstructed images under different conditions.

After that, the thesis proposes using finite element method (FEM) to allow accurate simulations of the reconstruction of floor blueprints, using ultra-high frequency narrowband continuous-wave signals under a parallel-beam acquisition geometry. This framework makes it possible to quickly and accurately evaluate different algorithms without the need to assemble a full test setup, which might not be available due to budgetary and time constraints. Considering all the drawbacks associated with such a complex problem, a robust and reliable computational setup based on a flexible method such as FEM can be very useful. To the best of our knowledge, this is the first attempt to use FEM in an RF-based TWM problem.

Finally, the thesis introduces an alternative acquisition geometry – the Multi-Sensor Circular Acquisition Geometry (MCG) – capable of reducing the time required to obtain the reconstructed floor map, in comparison to the traditional parallel-beam geometry. Unlike the latter, MCG is capable of detecting on-going floor layout changes, such as door barricading or collapsing. MCG performance is evaluated using the previously defined FEM model.

1.3 Thesis Structure

1.3.1 Part I: RF Indoor Positioning

- Chapter 2 brings a literature review on WiFi positioning, with a comparative analysis of several localization techniques for indoor single-floor environments;
- Chapter 3 presents the proposed machine learning-based location engine for multi-floor indoor positioning.

1.3.2 Part II: RF-Based TWM

- Chapter 4 studies the fundamentals of parallel-beam RF-based TWM and sets up a simulation model using path-loss equations corrupted by Rayleigh noise to account for multipath reception. Two test floor maps are defined, and a comparative analysis of the selected reconstruction methods is carried out. A metric for image quality assessment is tentatively selected to allow an objective comparison of the reconstructed images under different conditions.

- Chapter 5 proposes using FEM to allow accurate simulations of floor maps reconstruction. The FEM model is used to simulate parallel-beam RF-based TWM with different sets of systemic parameters (sampling rate, antenna models, operational frequency, etc.).

- Chapter 6 defines a multi-sensor circular acquisition geometry to allow faster reconstruction (with respect to the parallel-beam geometry used in chapters 4 and 5) and detection of floor layout changes (e.g., door barricading).

1.4 List of Publications

1.4.1 Published Books

1. CAMPOS, R. S., LOVISOLO, L.,"*RF Positioning: Fundamentals, Applications and Tools*", 1st ed., 328 pages, Boston, USA, Artech House, 2015.

1.4.2 Journal Publications

1. CAMPOS, R. S., LOVISOLO, L., DE CAMPOS, M. L. R. "*Wi-Fi Multifloor Indoor Positioning considering Architectural Aspects and Controlled Computational Complexity*", Expert Systems with Applications, v. 41, n. 14, pp. 6211-6223, October, 2014.

2. CAMPOS, R. S. "*Evolution of Positioning Techniques in Cellular Networks, from 2G to 4G*", Wireless Communications and Mobile Computing, v. 2017, pp.1–17, January, 2017.

1.4.3 Conference Publications

1. CAMPOS, R. S., LOVISOLO, L., DE CAMPOS, M. L. R. "*Search space reduction in DCM positioning using unsupervised clustering*", In: Proceedings of IEEE 10th Workshop on Positioning Navigation and Communication (WPNC), pp. 1–6, Dresden, Germany, March 2013.

2. CAMPOS, R. S., LOVISOLO, L. "*Genetic Algorithm Optimized DCM Positioning*", In: Proceedings of IEEE 10th Workshop on Positioning Navigation and Communication (WPNC), pp. 1–5, Dresden, Germany, March 2013.

3. CAMPOS, R. S., LOVISOLO, L., DE CAMPOS, M. L. R. "*WiFi Multifloor Indoor DCM Positioning*", In: Proceedings of the 31st Brazilian Telecommunications Symposium - SBrT2013, pp. 1–5, Fortaleza, CE, Brazil, September 2013.

4. CAMPOS, R. S., LOVISOLO, L. "*A Priori Selection of High Accuracy Mobile Station Position Estimates*", In: Proceedings of 2014 IEEE International Telecommunications Symposium (ITS), pp. 1–5, São Paulo, Brazil, August 2014.

5. CAMPOS, R. S., LOVISOLO, L., DE CAMPOS, M. L. R. "*Physical Modeling of RF Through-the-Wall Mapping using FEM*", In: Proceedings of the 34th Brazilian Telecommunications Symposium - SBrT2016, pp. 1–5, Santarém, PA, Brazil, August 2016.

6. CAMPOS, R. S., LOVISOLO, L., DE CAMPOS, M. L. R. "*Finite element method framework for RF-based through-the-wall mapping*", In: Proceedings of SPIE Defense + Security 2017, pp. 1–20, Anaheim, CA, USA, April 2017.

Chapter 2

A Survey of WiFi Indoor Positioning Techniques

This chapter brings a literature review on Wireless Fidelity (WiFi) positioning, with a comparative analysis of several localization techniques for indoor single-floor environments [9]. This survey was the starting point for the study which ultimately led to the proposal of the location engine for multi-floor positioning, which is introduced in Chapter 3.

2.1 Introduction

Since 1997, when the first IEEE 802.11 WiFi networks became available, Wireless Local Area Networks (WLANs) based on that standard have spread enormously. Nowadays, WiFi networks are ubiquitous in domestic, corporate and public areas. This fact, coupled with the availability of WiFi enabled smartphones, makes positioning of mobile stations (MS) in WLANs a crucial issue.

Positioning in WiFi WLANs is by no means restricted to indoor environments. However, it is in such scenarios that WiFi positioning becomes more useful, mainly due to:

(i) the unavailability of Global Navigation Satellite System (GNSS) signals in the majority of indoor environments;

(ii) the lower availability of cellular signals in indoor environments (unless there are dedicated micro and pico-cells deployed specifically to provide indoor coverage);

(iii) the high density of WiFi Access Points (APs) in indoor environments.

Practically all radio frequency (RF) positioning solutions use one of the following basic techniques:

(i) **cell identity** (CID): which assumes that the MS is located at the coordinates of the serving station;

(ii) **centroid**: the target MS position is given by the centroid of the polygon whose vertexes are the reference stations;

(iii) **multi-lateration**: provides the MS positioning based on distance estimates between the MS and the reference stations; those estimates are obtained using time or received signal strength (RSS) measurements; multi-lateration can be either circular or hyperbolic (time difference of arrival (TDOA));

(iv) **multi-angulation**: uses angle-of-arrival (AOA) measurements between the MS and the reference stations to yield a position estimate;

(v) **database correlation methods** (DCM): also referred to as scene analysis, pattern matching or RF fingerprinting;

Fig. 2.1 shows the basic geometric representation of the centroid and triangulation (multi-angulation e multi-lateration) methods. In Fig. 2.1a, the centroid of the polygon whose vertexes are the reference stations gives the position estimate (M). In Fig. 2.1b, three reference stations provide three circular lines-of-position (LOPs)[1] for an unambiguous MS position estimate. In Fig.2.1c, four reference stations provide three hyperbolic LOPs for an unambiguous MS position estimate. In Fig.2.1d, two non-collinear reference stations provide two linear LOPs for an unambiguous MS position estimate. In all cases, one must know the coordinates of the reference stations with the highest possible accuracy.

At first, all those techniques would apply to WiFi networks. However, even though there are a few exceptions (such as [10, 11]), most publications on the topic do not use methods **(i)** to **(iv)**. This is mainly due to the following issues:

(i) unlike cellular networks, round-trip delay (RTD) values are not available in WiFi networks; therefore, time-based multi-lateration would require the deployment of additional hardware;

(ii) APs antennas are typically omnidirectional; therefore AOA positioning would also require additional hardware (i.e., the installation of directional antenna arrays);

(iii) WiFi positioning is most relevant in indoor environments; however at such scenarios there are severe obstructions (such as walls, columns and furniture)

[1] A LOP is the set of points at which the target MS can be located. LOPs are generated when positioning methods based on triangulation (multi-lateration or multi-angulation) are used. Different positioning techniques yield different types of LOPs: linear, circular or hyperbolic. The MS estimated position is given by the intersection of two or more LOPs.

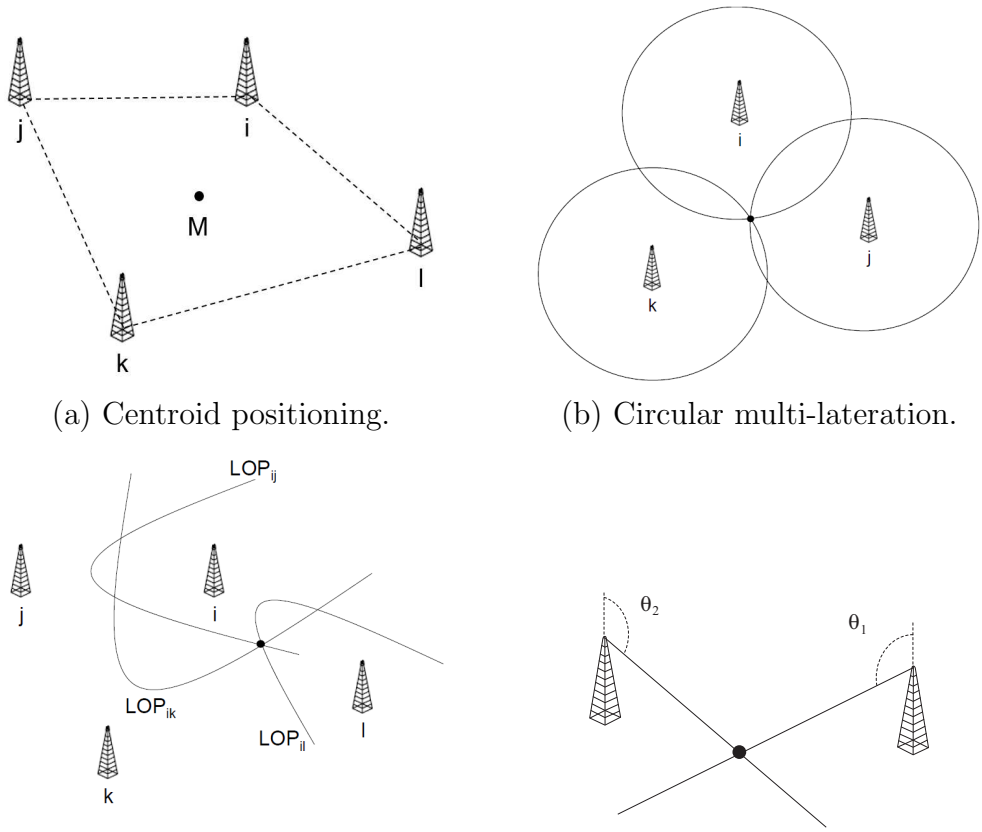

(a) Centroid positioning.

(b) Circular multi-lateration.

(c) Hyperbolic multi-lateration (TDOA).

(d) Multi-angulation (AOA).

Figure 2.1: Centroid and triangulation (multi-lateration and multi-angulation) positioning methods.

between the AP and the MSs; therefore, non-line-of-sight (NLOS) propagation is prevalent, and this condition severely hinders the accuracy of circular multi-lateration, TDOA and AOA positioning;

(iv) CID and centroid positioning require that the locations of the APs are known; however, this is hardly the case, as the APs are deployed in a chaotic manner, without a centralized coordinated effort as in cellular networks [12].

As a result, DCM becomes the mainstay technique in WiFi positioning, both in outdoor and indoor environments. This conclusion stems from the vast number of papers published on the subject if compared to other techniques. However, implementing WiFi indoor fingerprinting positioning systems is not an undertaking deprived of challenges:

(i) typically, extensive and time-consuming off-line training phases are required, to gather reference fingerprints to be stored in the correlation database (CDB);

(ii) the RF environment is not stable over time: new APs are deployed, others are shut down or moved to another location, the WLANs channel frequency might

change, furniture might be moved or added to the floor; consequently, the fingerprint map must be periodically updated to prevent accuracy degradation;

(iii) implementation differences between manufacturers might result in different devices reporting distinct RSS values at the same location (the so-called cross-device effect);

(iv) WiFi networks use an unlicensed band, so they are prone to suffer interference from external sources.

The remainder of this chapter is organized as follows: Section 2.2 introduces the basic DCM elements; Section 2.3 analyzes RF fingerprinting techniques for MS location in single floor scenarios; Section 2.4 studies other techniques used in such environments. Finally, Section 2.5 discusses some multi-floor positioning related issues, followed by a conclusion.

2.2 RF Fingerprinting Specificities

DCM, also known as RF fingerprinting, is a class of MS positioning methods that can be applied to any wireless network. Despite their variability and broad application scope, conceptually, all RF fingerprinting location systems share the same fundamental elements: RF fingerprint, correlation database, matching function, location server, and search space reduction technique.

2.2.1 RF Fingerprint

An *RF fingerprint* is a set of location dependent RF signal parameters gathered by an MS in a given position. Those parameters can be measured by either the MS to be located or by its anchor stations [2]. Just like a human fingerprint, which is assumed to uniquely identify a person, an RF fingerprint is expected to unambiguously identify a geographic position. An RF fingerprint can be classified as either a *target* (Tfing) or *reference* (Rfing) fingerprint. A Tfing is the RF fingerprint associated with the MS which is to be localized, i.e., it contains signal parameters measured by the MS or by its anchor cells. The Rfings are the RF fingerprints collected or generated during the training phase and stored in the correlation database.

Several RF fingerprinting location systems employ parameters that are already available in the radio access network (RAN). These parameters are *a priori* location

[2] A reference or anchor station is either a fixed or mobile station, which might contain a transmitter, receiver and/or a transponder, and whose signals are used by the target MS to estimate its position, or that uses the target MS transmissions to calculate the target position. The coordinates of the reference stations must be known at all times, and with the highest possible degree of confidence [9].

dependent and therefore each RF fingerprint can be associated with an specific position. If only RAN inherent parameters are included in the RF fingerprint, then the DCM technique can be entirely network-based. As a result, the deployment of the location system does not require any modification to existing MS.

Multi-angulation and multi-lateration positioning use signal parameters that change with the relative position between the target MS and a set of reference stations to estimate the MS location. Those techniques compute the position estimate from basic geometry, electromagnetic and signal processing principles. Those methods and RF fingerprinting differ on how they use the parameters to estimate the MS position. While in multi-angulation and multi-lateration, the position is estimated by inverting some signal parameters properties based on geometry and physics concepts, in RF fingerprinting there is no such inversion. The RF fingerprints collected by the MS are compared to previously obtained RF fingerprints to estimate the position of the collecting MS. As a result, RF fingerprinting, unlike multi-angulation and multi-lateration, does not rely on line-of-sight (LOS) geometric assumptions.

2.2.2 Correlation Database

The *Correlation Database* (CDB) is built during the DCM training phase [13, 14], using radio propagation modeling, field measurements or a combination of both [15]. Each CDB entry is described by $(\mathbf{f}, x, y, z)$, where $\mathbf{f}$ is the Rfing associated to the point defined by coordinates (x, y, z). The structure of $\mathbf{f}$ may vary depending on the radio access network (RAN) technology, but some common parameters are RSS, round trip-time (RTT) and delay profiles [16]. The CDB entries should be compared to the Tfing to yield a position estimate for the MS. The MS is assumed to be located at the point whose Rfing has the largest correlation or similarity with the Tfing. Alternatively, it is possible to select the K best matches, in which case the MS location is given by a weighted average of the K best matches coordinates (i.e., the K-Nearest Neighbors (KNN)) [17].

2.2.3 Pattern Matching

The main engine of RF fingerprinting is the *pattern matching* or *scene analysis* algorithm. It is used to compare the Tfing to the Rfings, previously stored in the CDB. From these comparisons, one finds candidates (the positions associated to the Rfings) to estimate the location where the target RF fingerprint has been collected.

2.2.4 Location Server

Location Server is a term typically used to refer to network elements (hardware and software) responsible for computing the position estimate. It receives location requests from different applications or devices, consults CDBs, and estimates the location of the target MS from its RF fingerprint. In the location server, the position estimate can be computed using any supported positioning technique. In the case of RF fingerprinting, it is important to emphasize that the location server must have access to the CDB.

2.2.5 Search Space Reduction Technique

The CDB might be quite large and analyzing all RF fingerprints stored in it might be very time consuming. To acquire a position fix within an acceptable time, some reduction in the search space (initially, all entries in the database) is welcome. Therefore, most fingerprinting location techniques employ strategies to reduce the search space within the CDB. As a consequence, the time required to produce a position fix is also reduced. Some of the techniques used in the literature are deterministic filtering [18] and optimized search using genetic algorithms [19], both applied upon RSS maps built with empirical propagation models [20]. In [21], the search space is reduced by clustering the candidate solutions. This clustering is based on the identity of the WiFi networks with the highest RSS at each measurement point.

2.2.6 Simplified Diagram of a DCM MS Originated Position Request

Fig. 2.2 shows the simplified diagram of an MS originated position request. First (step 1), the MS sends a position request containing the Tfing to the location server through the radio access network (RAN). After that (step 2), the RAN communicates with the location server. The location server receives the Tfing and then queries the CDB (step 3) for the reference RF fingerprints (Rfings), returned in sequence (step 4). The location server then compares the Tfing with the returned Rfings to obtain the MS position estimate (step 5), which is sent back to the RAN (step 6) and subsequently to the MS (step 7).

From this brief description, one notes that any fingerprinting location technique has two phases. The first is the training or building phase when the CDB is built. The second is the test or operational phase, during which MS position estimates are produced from gathered RF fingerprints.

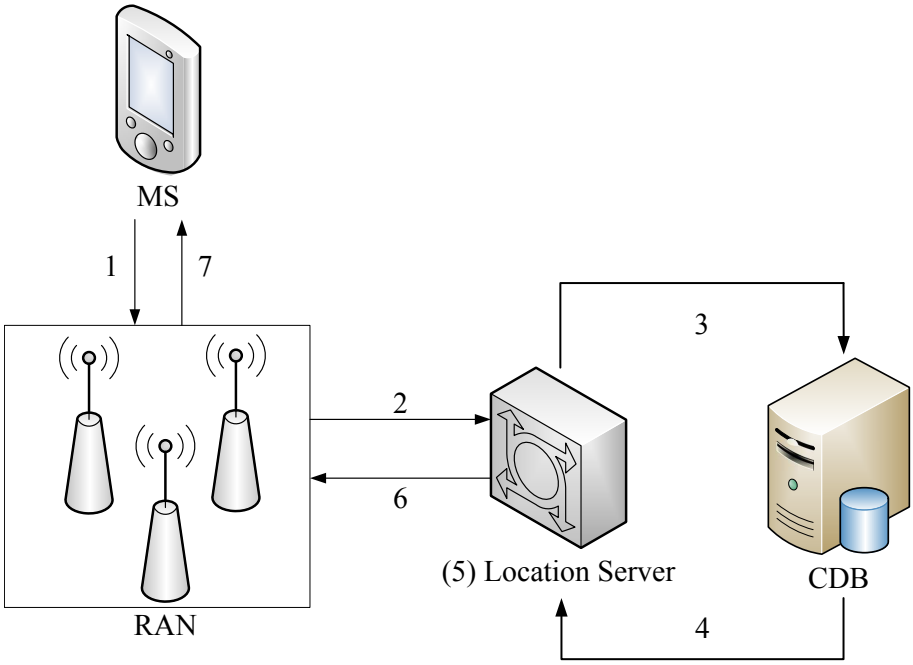

Figure 2.2: Diagram of RF fingerprinting location.

2.3 Single Floor Positioning using RF Fingerprinting

2.3.1 Nearest Neighbor in the Signal Space

One of the first RF systems for locating and tracking indoor users in WiFi networks was RADAR [22], published in the year 2000. The authors tested it in a 22×43 m^2 single-floor with 3 APs and 70 measurement points. At each measurement point, at least 20 samples (WiFi scans) were collected at four different directions (north, south, east, west), as the authors verified that, depending on the direction the user was facing, the RSS of a given AP might vary ± 5 dB. For each 3-tuple (x, y, ζ), at least 20 samples were collected, where (x, y) are the measurement point coordinates and ζ is the direction the user was facing. The mean RSS per AP at each point/orientation was then calculated, yielding 70×4 reference fingerprints.

To compare the target and reference fingerprints, the authors introduced the concept of *Nearest Neighbor in the Signal Space* (NNSS), i.e., the similarity between the fingerprints was measured by the Euclidean distance in the N-dimensional RSS space. In the RADAR test bed, $N = 3$, as only 3 APs were used. To test the algorithm, one of the four directions at the ith measurement point was selected to be the target fingerprint (Tfing). The reference fingerprint (Rfing) of the ith point was then excluded from the fingerprint map, and the Tfing was compared to the remaining 69×4 Rfings. The process was repeated for $i = 1, \ldots, 70$. The authors

in [22] reported a median two-dimensional (2-D) positioning error of 2.94 meters.

The authors conducted another experiment at the same test site, with a fingerprint map (for the same 70 measurement points) built using the empirical propagation model given by

$$P(d) = P(d_0) - 10n \log_{10}\left(\frac{d}{d_0}\right) - m \times \text{WAF} \tag{2.1}$$

where $P(d)$ is the RSS (in dBm) at d meters from the AP, d_0 is a reference distance in meters, n is the path loss exponent or slope, m is the number of walls between the AP and the current position, and WAF is the wall attenuation factor , i.e., the additional loss (in dB) introduced by each wall. Parameters d_0, n and WAF were empirically defined.

In the second experiment, the median 2-D positioning error increased to 4.3 meters. CDBs built from propagation models can reduce the time consumed in the off-line phase, either at the initial CDB acquisition or its periodic updates. However, it represents a trade-off between pre-processing time (off-line) and accuracy. Besides that, modeling RF propagation in indoor environments is not an easy endeavor. In [22], the authors were able to use equation (2.1) to build the fingerprint map only because the locations of the three APs on the floor were known.

For clarification, consider Fig. 2.3a, which shows a floor blueprint with the locations of four APs (white squares). The graphic scale indicates the additional loss in dB per R meters, where R is the blueprint matrix planar resolution. The floor dimensions are 20×40 m^2. It has a large entrance hall (left), a long corridor and three rooms, each one with just one entrance. The floor blueprint is represented as a matrix, where each element (pixel) corresponds to an $R \times R$ m^2 area. In this example, $R = 0.1$ m and, therefore, the blueprint is a 200×400 matrix.

The luminance level of the pixels is proportional to the additional loss (in dB) due to the presence of the barrier at the pixel location. Zero luminance indicates the absence of an obstacle at the pixel position. This simulation considers two types of obstacles: 30-cm thick concrete walls, with a 20 dB loss per meter, and 10-cm thick wooden doors, with a 8 dB loss per meter. Equation (2.1) defines the RF propagation model. The parameters values are $n = 3.43$, $d_0 = 2.5$, $P(d_0) = -43$ dBm [23]. The APs have omnidirectional antennas, so no radiation patterns were applied to generate the 2-D RSS coverage maps. The simulation does not consider multipath due to reflections from surfaces and diffraction around corners. Fig. 2.3b shows the best server map that represents, at each pixel, the highest RSS value. Figs. 2.3c and 2.3d depict the RSS (dBm) coverage maps of APs 3 and 4, respectively. The effect of the obstacles on the RF propagation is clearly distinguishable on both maps. The four RSS maps (one for each AP) can be "piled up," yielding a $200 \times 400 \times 4$

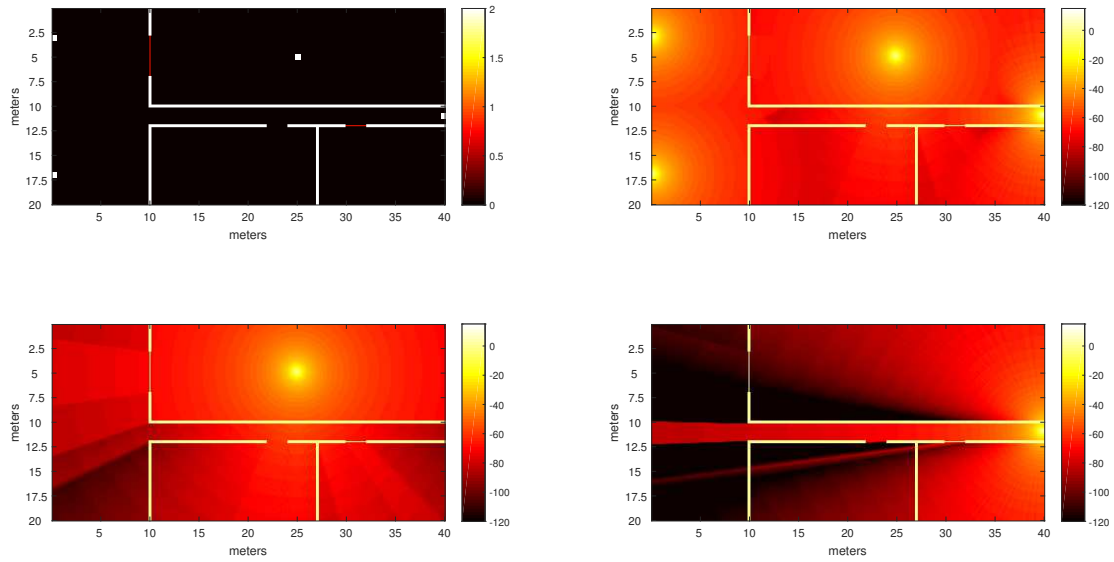

Figure 2.3: (a) APs locations and floor blueprint; (b) Best server map; (c) AP-3 RSS map; (d) AP-4 RSS map.

radio map that provides a 4-element RSS vector for each pixel in the floor grid.

2.3.2 Context-Aware Radio Maps

Changing environmental factors – such as air humidity, open or closed doors, and the presence of people – can interfere with the propagation conditions, altering the RSS at each point, in relation to the time when the fingerprint map was built. The authors in [24] tried to evaluate the quantitative effect of those environmental factors (air humidity, doors, and people) in WiFi indoor positioning accuracy. The presence of people has an effect similar to obstacles blocking the RF propagation. Open and closed doors have an effect comparable to changes in the floor layout. An atmosphere with high humidity is expected to absorb more energy of the propagating RF signal than a dry one.

They built *context-aware radio maps* which the target MS selects based on the current indoor environmental conditions. As the authors assumed two possible states for each of the three environmental factors (humidity – high or low; doors – all closed or all open; people – no people or people blocking the RF path), they built six fingerprint maps. They deployed one AP in each of the five rooms on a single floor and collected at least 200 WiFi scans along a corridor for each set of environmental factors. During the on-line test phase, the target MS queried humidity sensors, radio frequency identification tags (RFID) and Bluetooth devices, so that it could select

the best context-aware radio map to use. Such map is the one that better matches the environmental conditions at the time of the test. The RFID tags detected if the doors were open or closed. The changes in the average propagation loss between fixed Bluetooth transmitters and the target MS identified the no-people or people-blocking condition.

Tables 2.1 and 2.2 show accuracy degradations of 1.1 meters – when a low-humidity radio map is applied in a high-humidity environment – and 1.9 meters – when a no-people-blocking radio map is employed in a people-blocking test environment. However, Table 2.3 indicates that the worst scenario occurs when there is a mismatch in the open/closed doors condition: the average location error increases from 2.1 meters to 7.2 meters (more than three times the original value) when an all-doors-closed radio map is used in an all-doors-open test environment.

The system proposed in [24] can still be classified as DCM for WiFi 2-D indoor positioning because even though it employs non-WiFi devices – humidity sensors and Bluetooth transmitters – those were not used in the position fix. They just helped to select the context-aware radio map better suited to the current test conditions.

To the best of our knowledge, this is the first experimental setup developed to quantitatively evaluate the effect of changing environmental dynamics in WiFi indoor localization. However, it has some severe limitations, if considered for a practical large-scale implementation, as it requires:

(i) the deployment of additional hardware;

(ii) that users carry Bluetooth-enabled devices;

(iii) that users keep their MSs' built-in Bluetooth adapters on.

Even tough item **(ii)** is a quite reasonable requirement considering currently available smartphones, item **(iii)** is not, as the majority of users keep their Bluetooth adapters off most of the time to increase battery lifetime.

Table 2.1: Impact of Relative Humidity (RH) on average DCM positioning accuracy (all-doors-closed and no-people-blocking).

Average Accuracy	40% RH Radio Map	70% RH Radio Map
40% RH environment	2.1 m	3.7 m
70% RH environment	3.1 m	2.6 m

Table 2.2: Impact of people blocking on average DCM positioning accuracy (40% RH and all-doors-closed).

Average Accuracy	No-people-blocking Radio Map	People-blocking Radio Map
No-people-blocking environment	2.1 m	4.3 m
People-blocking environment	4.0 m	2.5 m

Table 2.3: Impact of open/closed doors on average DCM positioning accuracy (40% RH and no-people-blocking).

Average Accuracy	All-doors-closed Radio Map	All-doors-open Radio Map
All-doors-closed environment	2.1 m	4.6 m
All-doors-open environment	7.2 m	2.8 m

2.3.3 On-demand Radio Maps for Client-Based Solutions

DCM indoor positioning solutions might be classified either as MS-assisted or MS-based. In the MS-assisted case, a location server calculates the MS position using fingerprints sent by the target MS and querying a server-based CDB. In the MS-based case, the MS calculates its position querying a client-based CDB, i.e., a fingerprint map stored in the MS itself [3]. In the case of a server-based CDB, the location server might have to deal with several simultaneous location requests, and a search space reduction technique might significantly reduce the delay of each position fix. In the case of a client-based CDB, a search space reduction technique, besides speeding up the position fix acquisition time, also reduces the network load (as the MS downloads smaller fingerprint maps) and the required storage space at the MS. In [25], the authors proposed two techniques to diminish the search space in client-based solutions: Intersection of Access Points (IAP) and Union of Access Points (UAP).

In IAP, the target MS downloads only the Rfings containing at least all the APs detected in the WiFi scan. In UAP, the MS downloads the Rfings containing at least one of the APs detected in the WiFi scan. The authors also defined a criterion called N-Group to trigger a fingerprint data query (i.e., the query and download of an updated search space from the location server to the client-based CDB) whenever more than N APs changed in two consecutive WiFi scans. The higher the N, the lower the frequency of fingerprint data queries. The objective of N-Group was to reduce the frequency of data queries, without degrading positioning accuracy.

[3]The client-based CDB is usually a subset of the server-based CDB.

Their experimental testbed comprised 25 APs and was set on the second floor of an office building with 57×32 m^2 on the campus of the University of Manheim. The off-line training phase used 130 measurement points disposed in a regular grid with 1.5-meter spacing. In the test phase, 46 points were randomly chosen. Both in the training and test phases, 110 WiFi scans were collected per point. The average accuracy was 3 meters, using no search space reduction [4]. Then, the value of N was progressively increased when using IAP and UAP, and three parameters were monitored: positioning accuracy, fingerprint map query frequency, and search space size (measured by number of points, i.e., Rfings). The authors in [25] observed that, when using UAP, the search space reduction was negligible: the average search space size was 129. However, when using IAP, the average search space size shrank to 12. With IAP, when increasing N from 1 to 10, the positioning error augmented almost 20% (from 3 meters to 3.5 meters).

2.3.4 ANN-Based Pattern Matching

The authors in [27] use a feed-forward artificial neural network (ANN) to establish a relationship between input WiFi RSS vectors and locations. In an indoor environment, they deployed three APs in a 28×15 m^2 floor and selected 125 points, collecting 400 samples per point. The samples collected at 110 points were used to train the ANN. The remainder points were used to test it. The ANN had three inputs (the RSS values of each AP), 18 neurons in the hidden layer and two outputs (planar coordinates x and y). As in [28], the experimental accuracy was excellent: 61% of the test patterns had errors lower than 1.8 meters, and 85% had errors smaller than 3 meters. However, there is no guarantee that ANN-based pattern matching algorithms will yield such high accuracy in more complex scenarios, such as in multi-storey buildings, or when radio maps built with propagation models are used in the supervised training.

2.3.5 RF Fingerprinting using Parameters other than RSS

All DCM techniques studied so far in this chapter used RF fingerprints containing only mean RSS values, which are relatively simple to measure and are readily available in WiFi networks. These traits made RSS fingerprinting a practical solution for WiFi localization systems. The core difference between distinct implementations lies mostly on how the target and reference fingerprints are compared, i.e., on which pattern matching technique (NNSS, RSS rank correlation, ANN-based) is used. However, other parameters can be employed in the RF fingerprint.

[4] The probabilistic positioning algorithm used in [25] is defined in [26].

The aforementioned possibility is explored in [16], where the authors compared the accuracy of DCM techniques applied to 2.4 GHz WiFi indoor positioning using RSS, Channel Impulse Response (CIR), Channel Transfer Function (CTF) and Frequency Coherence Function (FCF)-based fingerprints. The CIR to the impulse transmitted by the jth AP is given by

$$\mathbf{h}_j(t) = \sum_{i=1}^{M} a_i e^{-j\phi_i} \delta(t - \tau_i) \tag{2.2}$$

where a_i, ϕ_i and τ_i are the amplitude, phase and delay of the ith received multipath component; M is the number of multipath components and $\delta(t)$ denotes the impulse function. Equation (2.2) shows that, in multipath propagation conditions, the receiver detects multiple delayed and attenuated copies of the transmitted impulse. By taking the CIR with respect to different APs at the same position, it is possible to build an RF fingerprint given by $[\mathbf{h}_1(t) \dots \mathbf{h}_N(t)]$, where N is the number of APs. Note that each element of the fingerprint is an M-element vector, so the CIR-based fingerprint is an $M \times N$ matrix. The CIR is expected to carry the multipath information that is unique to each location. However, the possible accuracy is limited by the signal bandwidth: higher bandwidths are equivalent to higher time-domain resolution, which allows detecting (separating) more multipath components (i.e., increasing M).

CTF is the Discrete Fourier Transform (DFT) of the CIR [5]. A CTF-based fingerprint can then be formed, which will have the same dimensions of the CIR-based fingerprint. The same applies when using FCF-based fingerprints, where the FCF for the jth AP at a given measurement position is the complex autocorrelation of the CTF.

The authors set up an experimental testbed in a 30×25 m^2 single-floor with 3 APs. A total of 152 measurement points were chosen with a fixed distance of 1 meter between adjacent points. Amidst those points, 51 were randomly selected for the test, and the remainder composed the CDB. Euclidean distance in the signal space was used to compare the target and reference RSS-based fingerprints (the higher the distance, the lower the similarity). For the CIR, CTF and FCF-based fingerprints, vector correlation (dot-product) was used (the higher the dot-product, the higher the similarity). Then, weighted K-Nearest Neighbors (w-KNN) was applied. In w-KNN, the position estimate is given by

$$(\hat{x}, \hat{y}) = \frac{\sum_{i=1}^{K} w_i (x_i, y_i)}{\sum_{i=1}^{K} w_i}, \tag{2.3}$$

[5] In [16] the authors measured the RSS and the CTF (frequency-domain). Then the CIR was obtained calculating the Inverse Discrete Fourier Transform (IDFT) of the CTF.

where K is the number of neighbors, w_i and (x_i, y_i) are the weight and the reference coordinates of the ith neighbor point, respectively. The weight w_i is directly proportional to the similarity between the target and ith reference fingerprints. As in any weighted average calculation, $\sum_{i=1}^{K} w_i = 1$.

FCF-based fingerprints achieved the best results: an average error of 2.5 meters, with almost no variation as the number of neighbor points in the w-KNN algorithm increased from 1 to 10. RSS-based fingerprinting was the technique that benefited the most from the use of w-KNN: the average error dropped from 3.5 meters (for $K = 1$) to 2.8 meters (for $K = 9$). CTF performance was a little worse than FCF, and CIR was the worst of all, with errors between 3 and 4 meters for K ranging from 2 to 10 (for $K = 1$, the CIR-based fingerprinting error was 4.2 meters). Even though FCF-based fingerprinting performed better in the test, if one considers practical larger implementations, the accuracy gain will most likely not compensate the increased complexity of obtaining those measurements (which would involve the deployment of additional hardware to the pre-existing WiFi network infrastructure), if compared to the relative simplicity of measuring RSS.

2.4 Single Floor Positioning using Other Techniques

2.4.1 Fingerprinting + RSS-Based Multi-Lateration

In [23] the authors proposed a hybrid positioning scheme with two phases. In the first phase, RF fingerprinting identifies the room where the MS is most probably located. In the second phase, RSS-based multi-lateration locates the MS within the pre-selected room.

The testbed was a 17×23 m^2 floor (comprising 7 rooms and a large corridor) with 5 APs. The radio map for the fingerprinting algorithm was built using RSS mean values obtained from WiFi scans collected at 14 locations. The DCM similarity measure was the Euclidean distance. The WiFi 802.11b/g scans collected at another 100 points (12 samples per point) were used to calibrate the empirical propagation models. Path loss equation (2.1) was employed to estimate the RSS. The distances between the MS and the APs were obtained by taking the inverse of the path loss equation. A total of nine symbolic locations were defined: the seven rooms plus two sections of the corridor. For each AP and each symbolic location, different path loss equation parameters – reference distance [6], RSS at the reference distance [7],

[6]The reference distance d_0 can be chosen arbitrarily. In the experiment conducted in [23], it was fixed as 2.5 meters for all APs.

[7]The value of $P(d_0)$ can be obtained from the hardware specifications provided by the AP

attenuation slope – were defined.

As the floor blueprint and the APs locations are known, by identifying which room the target MS is located in, it is possible to select a specific propagation model and also compute additional losses due to obstructions (walls). Attenuation factors obtained during the experiment for different types of walls are listed in Table 2.4. The values of $P(d_0)$ for each AP (WX-1590 SparkLAN) were measured at a reference distance of $d_0 = 2.5$ meters, and their values ranged from -46.7 dBm to -43.7 dBm.

In the test phase, 30 locations were selected. In the first stage, fingerprinting achieved a symbolic location identification accuracy (room or corridor section) of 97%. In the second stage, multi-lateration using specific (for each AP and each symbolic location) calibrated propagation models achieved a mean 2-D positioning accuracy of 1.83 meters. However, when applying fingerprinting only (using a radio map with 33 reference fingerprints instead of only 14), the planar error was 1.78 meters, i.e., approximately the same accuracy.

Table 2.4: Wall Attenuation Factor (WAF) for different types of walls [23].

Type of Obstacle	**WAF (dB)**
Very Thick Concrete Wall	12.6
Thick Concrete Wall	9.5
Concrete Wall	5.5
Soft Partition	0.8

2.4.2 Multi-Lateration using an RTS/CTS Distance Estimator

In [10] the authors explored the use of the Request-to-Send (RTS)/Clear-to-Send (CTS) two frame exchange mechanism [8] in the WiFi Medium Access Control (MAC) sub-layer to obtain range estimates between the MS and the AP. These distances would later be applied to locate the target MS by circular multi-lateration. As there is no synchronization between the AP and the MSs in WiFi networks, the time-of-flight cannot be measured directly. Instead, it is obtained from the round-trip-time (RTT) between the MS and the AP. The target MS transmits an RTS at

manufacturer or derived empirically. The authors in [23] observed variations of ± 1.5 dB in the APs output power (with respect to the values informed by the manufacturer), so the latter method was selected.

[8] The RTS/CTS scheme is part of the medium access control in WiFi WLANs [29]. It reduces collisions by defining periods during which the wireless medium is reserved for only one station. Before transmitting a data frame, a station sends an RTS frame to the AP. The RTS informs the time that will be needed to transmit the subsequent data frame. Upon reception of the RTS, the AP sends a CTS frame. All nearby stations, on reception of the RTS and/or the CTS frames, refrain from transmitting for the required duration.

instant t_i. Upon reception, the AP replies with a CTS, which is received by the target MS at instant t_f, yielding

$$\mathrm{RTT} = \mathrm{t}_f - \mathrm{t}_i \tag{2.4}$$

If the processing time Δt at the AP is known, it can be subtracted from the RTT value. The outcome is divided by two, producing a time-of-flight, that, once multiplied by the speed of propagation of the radio wave (c), provides a distance estimate given by

$$d = \frac{c\,(\mathrm{RTT} - \Delta t)}{2} \tag{2.5}$$

At least three distance estimates from different APs are required for a position fix. The authors performed an indoor test along a 50×4.3 m^2 corridor. During the test, there was always a line-of-sight between the target MS and each AP. On average, the ranging estimates had an error under 4 meters. However, the authors did not report the positioning accuracy achieved using those range estimates in circular multi-lateration. This location technique has two major drawbacks:

(i) it requires the deployment of additional hardware (a printed circuit board with an Intersil HFA3861B base-band processor) at each MS to allow measuring the RTT;

(ii) to operate, the system needs that the RTS/CTS exchange is activated; however, in most networks this scheme is disabled (or is only used to reserve the medium for the transmission of large data frames), as it introduces additional traffic and delay in the network.

2.5 Multi-Floor Positioning

In WiFi outdoor and single floor positioning, one is concerned in estimating the MS coordinates over a plane, i.e., 2-D localization [9]. However, when it comes to multi-floor indoor environments, a practical solution has to find out not only the MS planar coordinates on any given floor but also the floor on which the MS is located. In fact, most frequently one is not interested in knowing the MS height on a given floor, but simply on which floor it is on. Therefore, the vertical coordinate can be treated as a discrete variable, conveying only the floor number. Such problem –

[9] One could indicate the work presented in [28] as an exception, as there the ANN's output yielded the estimated MS position with three coordinates (x, y, z). However, the MS antenna during the training and test phases was essentially always at the same height above the ground – placed on the roof a moving vehicle driving along four parallel lanes. Consequently, there was practically no variation in the MS estimated height, and the problem could be reduced to 2-D positioning.

when there are two continuous planar coordinates (x, y) and one discrete vertical coordinate z – is referred to as 2.5-D positioning [30].

If one considers structural aspects of the majority of multi-storey buildings, it is obvious that planar positioning errors are much less relevant than errors of the same magnitude along the vertical direction. For example, a 15-meter error along a corridor is much less important than the same error along the z-axis. In the former, the distance between the MS estimated and real location would be traversed in a few seconds. In the latter, that same error would be equivalent to three or four floors below or above the floor where the MS is located, which would require much more time to traverse. If one considers security applications, the importance of this comparison becomes even more evident. Nevertheless, even though there is a vast number of papers on WiFi indoor positioning, surprisingly very few address the multi-floor scenario.

2.6 Conclusions

This chapter presented a comprehensive survey on WiFi indoor positioning techniques, grouping and analyzing the key aspects of several papers on the subject. Most solutions rely on RSS fingerprinting, applying features as NNSS, context-aware radio maps and ANN-based pattern matching to improve accuracy. A few researchers use other parameters to compose the RF fingerprint (such as CIR, CTF, and FCF), as well as alternative techniques to reduce the search space within the radio map (such as IAP and UAP).

As a conclusion of this study, one could add that an arbitrarily high location precision in WiFi networks can certainly be obtained in well-controlled environments with the deployment of a very high number of APs. Nonetheless, the main research focus on this area lies in seeking the best precision in chaotic environments, where most of the times not even the location of the APs is known. This allows the easy deployment and use of localization systems in a wider range of situations, with minimum cost and delay. Another conclusion is that, due to the intrinsic characteristics of in-building RF propagation, fingerprinting seems to be the best alternative for WiFi indoor positioning.

From this survey, it became evident that the most critical issue in WiFi indoor positioning is floor identification in multi-storey buildings. Surprisingly, only a minority of papers address this subject. Therefore, improving floor identification accuracy, while preserving a low 2-D positioning error, became the main objective driving the development of the location engine presented in Chapter 3.

Chapter 3

Machine Learning-Based Location Engine for Multi-Floor Positioning

This chapter proposes a machine learning-based location engine for multi-floor indoor positioning. Considering the peculiarities of multi-storey environments – both architectural and RF propagation aspects – the location engine combines unsupervised and supervised learning and a database correlation method to improve floor identification accuracy, while maintaining the in-floor two-dimensional positioning error low. The chapter also brings the details of an experiment conducted in a 13-floor building, where the proposed localization scheme achieved floor identification accuracies ranging from 91% to 97%, with mean two-dimensional positioning errors spanning from 3.5 to 1.1 meters. A comprehensive literature review on the theme was conducted, so that the achieved results could be compared with those of other published methods [31].

3.1 Introduction

There is a growing number of Mobile Stations (MS) equipped with built-in Global Positioning System (GPS) receivers. In open areas, GPS yields the highest location precision but is usually unavailable in indoor environments. In this scenario, Received Signal Strength (RSS) based location techniques are used both in cellular and WiFi networks [1]. These techniques employ the measured RSS from distinct network nodes to estimate the MS position.

In cellular mobile telephony, indoor positioning might rely on the reception of signals from indoor micro or even pico-cells, or from nearby outdoor cells with strong RSS [2]. However, the increasingly denser deployment of WiFi access points (AP), coupled with the fact that most mobile devices today are WiFi enabled, makes the use of WiFi signals a superior choice for indoor positioning, in comparison to

cellular mobile telephony signals [3]. Besides that, the literature review carried out in Chapter 2 highlighted that database correlation methods (DCM) have already been established as a viable alternative for indoor WiFi positioning [25, 32–34]. However, even tough there is a wide variety of papers on single-floor indoor WiFi positioning, very few address localization in multi-storey buildings.

Multi-floor positioning is usually approached considering that radio frequency (RF) fingerprints collected at nearby locations – specially if gathered on the same floor – are similar and will group together, when some sort of clustering is used. This means that there is an implicit assumption that similarities among data points in the RSS space will correspond to similarities in the architectonic space, i.e., reflect the geometry of the building. However, due to the inherent complexity of radio-wave propagation in indoor environments, this is hardly the case. In the RSS space, the similarities among data points may not reflect their proximity in the architectonic space. For example, referring to Fig. 3.1, although the distances from the AP to the measurement points may be ordered as $d_B < d_{C_2} < d_A < d_{C_1}$, propagation conditions might be such that $\mathrm{RSS}_B > \mathrm{RSS}_A > \mathrm{RSS}_{C_2} > \mathrm{RSS}_{C_1}$. That is, the RSS order does not map into the distance order. Obviously, the actual figures for these examples will depend on the geometry of the building, materials, transmission frequency, among other physical parameters.

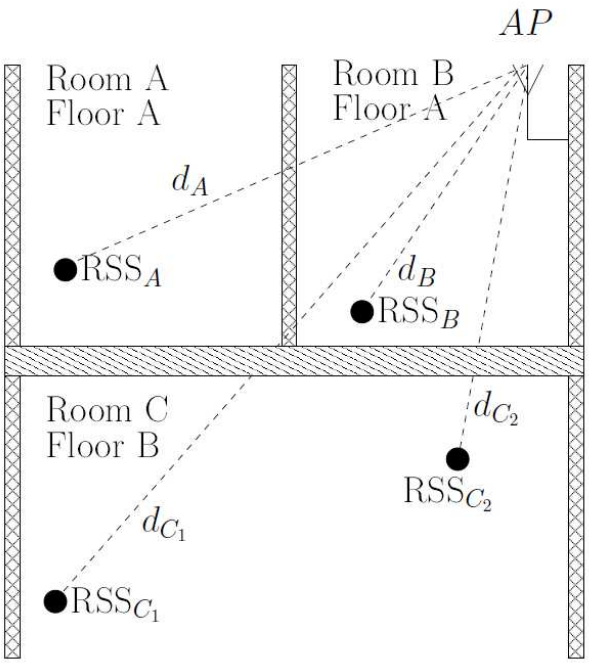

Figure 3.1: Example of WiFi multi-floor environment.

When implementing or using an indoor location system, one may not be troubled by small planar errors. For example, suppose that one is in a garage or mall. If the system indicates that an MS is within three or five meters from its actual location, this error may be irrelevant. However, for the majority of indoor positioning applications, floor error might be unacceptable – mostly because buildings are built in such a way that it is much easier to move on the same floor than among floors. In the case of emergency call location, response teams (firemen, paramedics, policemen), more than an accurate two-dimensional (2-D) position fix of the target terminal, need a floor identification accuracy close to 100% [35, 36]. The same applies for indoor positioning applications designed to help people with special needs, like children and elderly tracking [36], or to help the blind finding the floor of destination in multi-storey buildings [37]. Moreover, as usually one is not interested in knowing the MS height on a given floor, but simply on which floor it is most probably located, the vertical coordinate can be treated as a discrete variable, conveying only the floor number. Such problem – when there are two continuous planar coordinates (x, y) and one discrete vertical coordinate z – is referred to as 2.5-D positioning [30].

Thus, to enhance accuracy in floor identification, this chapter proposes a location engine that combines both approaches: natural (data points grouped directly without considering building structural characteristics) and architectonic (data points grouped considering room and floor separation, among other possible building architectural features). For the natural or RF approach, a single Kohonen layer with conscience is used. This tries to accommodate the similarities among data gathered in the signal/natural (RSS) space using an unsupervised clustering technique. After that, a supervised classifier is employed for considering the architectonic aspects (floor classification). In this context, a majority voting committee of feedforward artificial neural networks (ANNs) is used within each cluster for identifying the floor on which the MS is located. Outputs of joint voting classifiers are expected to have a lower variance than outputs of single binary classifiers [38], smoothing the stochastic component inherent to the ANN training and providing a more reliable and stable classification.

The proposed strategy is tried with actual data collected in a massive 13-floor building. Particular care has been taken regarding data collection, obtaining a high number of measurement samples so that the experimental results could be more reliable and representative of the type of environment under analysis. Notably, not many papers that approach the indoor positioning problem use datasets spanning more than one floor [11, 35, 39–44].

The remainder of this chapter is organized as follows: Section 3.2 provides a diagram of the proposed location engine; Section 3.3 details the data collection phase; Section 3.4 approaches issues related to unsupervised clustering. Within

the latter, Section 3.4.1 formulates a technique to estimate the optimal number of clusters and Section 3.4.2 outlines the unsupervised clustering techniques that are explored in this work (K-medians and Kohonen layer); Section 3.5 describes the floor classification procedure. Finally, Section 3.6 presents the experimental evaluation and Section 3.7 brings a brief conclusion.

3.2 Diagram of the Proposed Location Engine

Fig. 3.2 shows a diagram of the proposed location engine, in the post-training phase or *on-line* phase. Initially, the Tfing is transported to the principal components subspace, through principal components analysis (PCA) (step 1). This step is performed to reduce the number of components of the input vectors that shall be fed to the classifiers. Although there are other alternatives for dimension reduction, PCA is chosen here as it is simple and provides good results, as confirmed by the experiments.

Then, the input vector is fed to both an unsupervised classifier and a committee of supervised classifiers (step 2). The unsupervised classifier identifies the cluster which the Tfing belongs to. As already discussed in Section 3.1, those clusters are created allowing the Rfings to group freely in the RSS (or natural) space. However, as Fig. 3.8 shows, a cluster might span several floors. That is where the committee of supervised classifiers steps in. It is composed of committees of feed-forward ANNs, one committee per floor. For simplicity and improved accuracy, each ANN (also referred to as a multi-layer perceptron (MLP)) is trained as a binary classifier. So, each ANN in the committee of the jth floor indicates if a given Tfing was collected on the jth floor, or not. Therefore, the reduced search space is defined by the intersection of the following sets of Rfings:

(i) the set of Rfings within the cluster selected by the unsupervised classifier;

(ii) the set of Rfings within the floor indicated by the committees of feed-forward ANNs (step 3).

Not all committees are activated, but only those pertaining to the floors spanned by the RSS cluster identified by the unsupervised classifier. The darker section in the CDB represents the reduced search space, defined in step 3.

After that, back to the N_w-dimensional RSS space, the Tfing is compared to all the Rfings within the reduced search space (step 4). Finally, the process returns the coordinates (x, y, z) of the measurement point containing the Rfing with the highest similarity with the Tfing (step 5). These coordinates provide the estimated MS position.

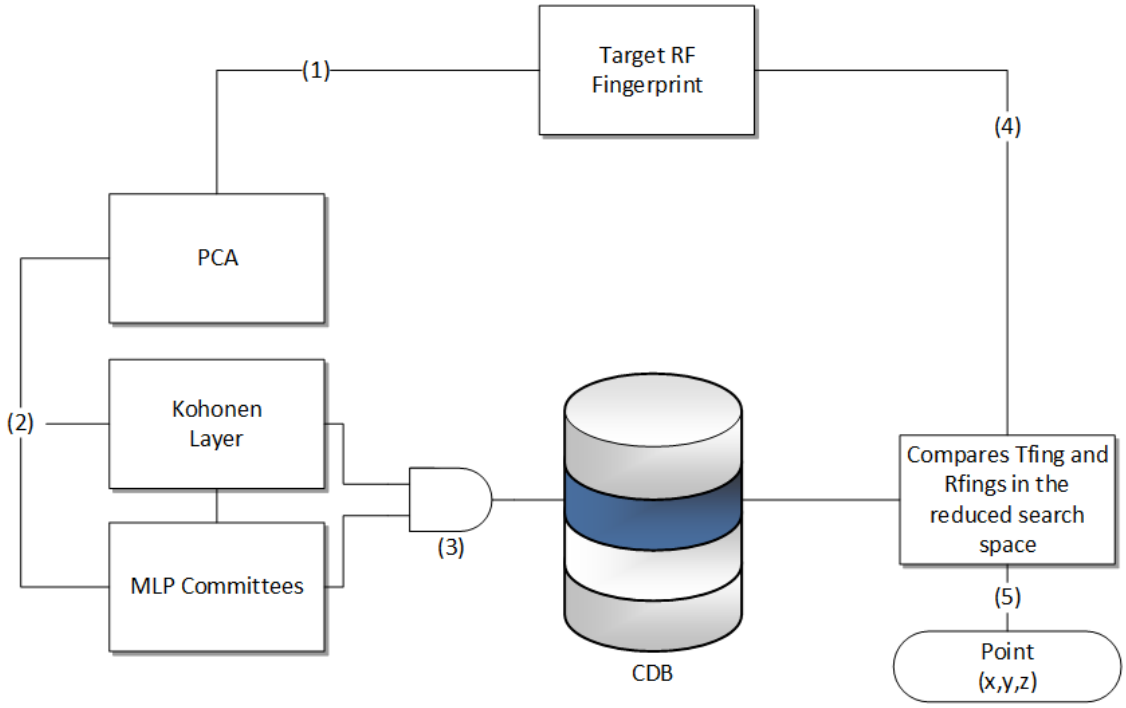

Figure 3.2: Diagram of the location engine proposed in this work.

The fingerprint structure used in this work, common to both Rfings and Tfings, is defined by the vector

$$\mathbf{f} = [\mathrm{RSS}_1 \ldots \mathrm{RSS}_{N_w}], \tag{3.1}$$

where RSS_k denotes the RSS from the kth AP and N_w informs the number of WiFi 802.11b/g networks used to estimate the MS position.

Comparison of the Tfing and the Rfings is performed by computing a distance metric between these fingerprints in the N_w-dimensional RSS space. Let $\mathbf{f}$ be the Tfing associated with the MS to be localized. The Rfing $\mathbf{f}_i$ most similar to $\mathbf{f}$ can be given by

$$i = \arg\min_j \left[(\mathbf{f} - \mathbf{f}_j) (\mathbf{f} - \mathbf{f}_j)^{\mathrm{T}} \right], \ \forall \mathbf{f}_j \ \in \ \mathcal{A}, \ \mathcal{A} \subseteq \mathcal{T} \tag{3.2}$$

where $\mathcal{T}$ is the set of Rfings in the CDB and $\mathcal{A}$ is the set of Rfings in the search space. Equation (3.2) measures the similarity between $\mathbf{f}$ (the Tfing) and $\mathbf{f}_j$ (the jth Rfing), seeking the minimum of the Euclidean distance [45]. This choice of search criterion outputs the index i of the $\mathbf{f}_j$ closest to $\mathbf{f}$. This metric considers the actual RSS values in $\mathbf{f}$. It is important to highlight that other distance metrics could be employed as the Mahalanobis [45] (for which the Euclidean distance is a particular case), Tanimotto [46] or the Hamming or Manhattan distance, among others. The MS estimated position is given by the coordinates associated with $\mathbf{f}_i$, obtained from the 4-tuple $(\mathbf{f}_i, x_i, y_i, z_i)$.

3.3 Data Collection

The WiFi RSS measurement campaign was carried out in the 13 floors of Reitor João Lyra Filho Pavilion at the Rio de Janeiro State University (UERJ). Fig. 3.3 depicts the outline of the building's six blocks. Corridors and ramps (not shown in the figure) interconnect the blocks.

The software used to collect the WiFi scans was *NetStumbler* version 0.4, running on a Toshiba A75-S211 laptop with an Atheros AR5005GS built-in 802.11b/g adapter. *NetStumbler* forces the WiFi adapter to carry out a passive scan of 802.11 networks, i.e., without sending probe requests. During the passive scan, the WiFi adapter remains a certain period on each channel, waiting to receive a beacon. The beacon, which is sent by every WiFi access point (AP), contains the network identifier (SSID – Service Set Identifier) and the AP MAC (Medium Access Control) address. For each detected AP, *NetStumbler* stores the MAC, SSID, carrier number, noise level and signal-to-noise ratio. The laptop was placed on a wheeled table, and at each of the 924 measurement points, the WiFi adapter gathered between 180 and 240 WiFi scans, at a rate of one per second.

Fig. 3.3 indicates the location of the measurement points on the sixth floor. The separation between adjacent points is 3 meters. This distance is the planar resolution of the CDB. Each measurement point is identified by a unique Rfing containing the mean RSS values (stored in the logarithmic scale, ranging from -120 to -30 dBm) of each WiFi network detected at that particular point. If a WiFi network is detected in less than 10% of the WiFi scans at a given point, its mean RSS value is not included in that point's Rfing. A total of $N_w = 136$ WiFi networks were detected at N_p=924 different positions [1].

Fig. 3.4 illustrates the mean RSS levels of four distinct APs. Points where they are not detected (or are detected in less than 10% of the WiFi scans) are not shown. Each AP has a different RSS distribution in the building. As previously discussed, using RSS levels collected from distinct APs may allow estimating the MS location. However, for that to be feasible, the fingerprints of RSS levels must allow a good separation of the data according to the position where they are gathered.

Ideally, the Rfings gathered in distinct floors would group in the RSS space into different clusters, directly allowing floor identification. However, this is hardly the case. Fig. 3.5a shows points collected in three distinct floors – different markers are used on each floor. Figs. 3.5b,c show how the RSS levels distribute in the three-dimensional (3-D) RSS space. For that, the three strongest APs detected at the measurement points indicated in Fig. 3.5a are used. It is perceivable – particularly in Fig. 3.5c – that it is possible to separate (group into an individualized cluster)

[1] The full dataset can be downloaded from *us.artechhouse.com/Assets/Downloads/campos.zip* [9].

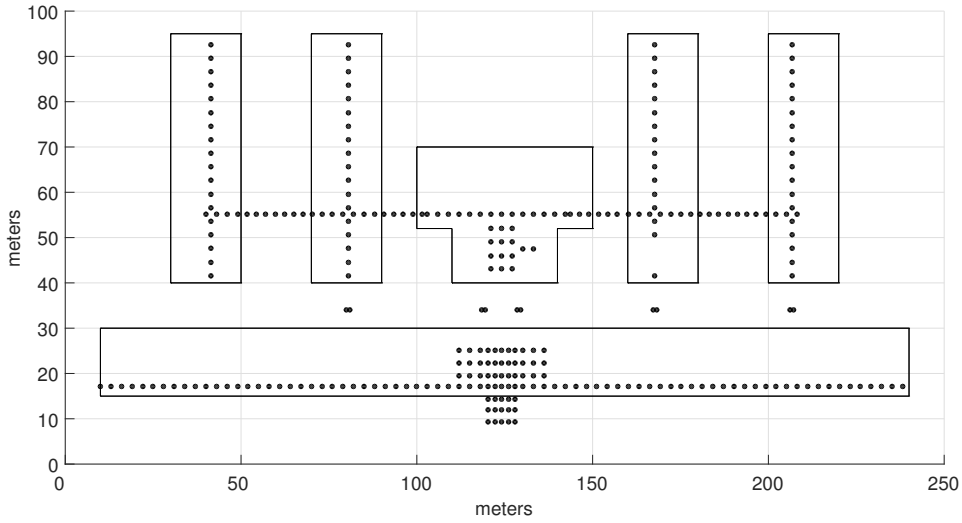

Figure 3.3: Planar distribution of measurement points within one of the floors of UERJ's main building.

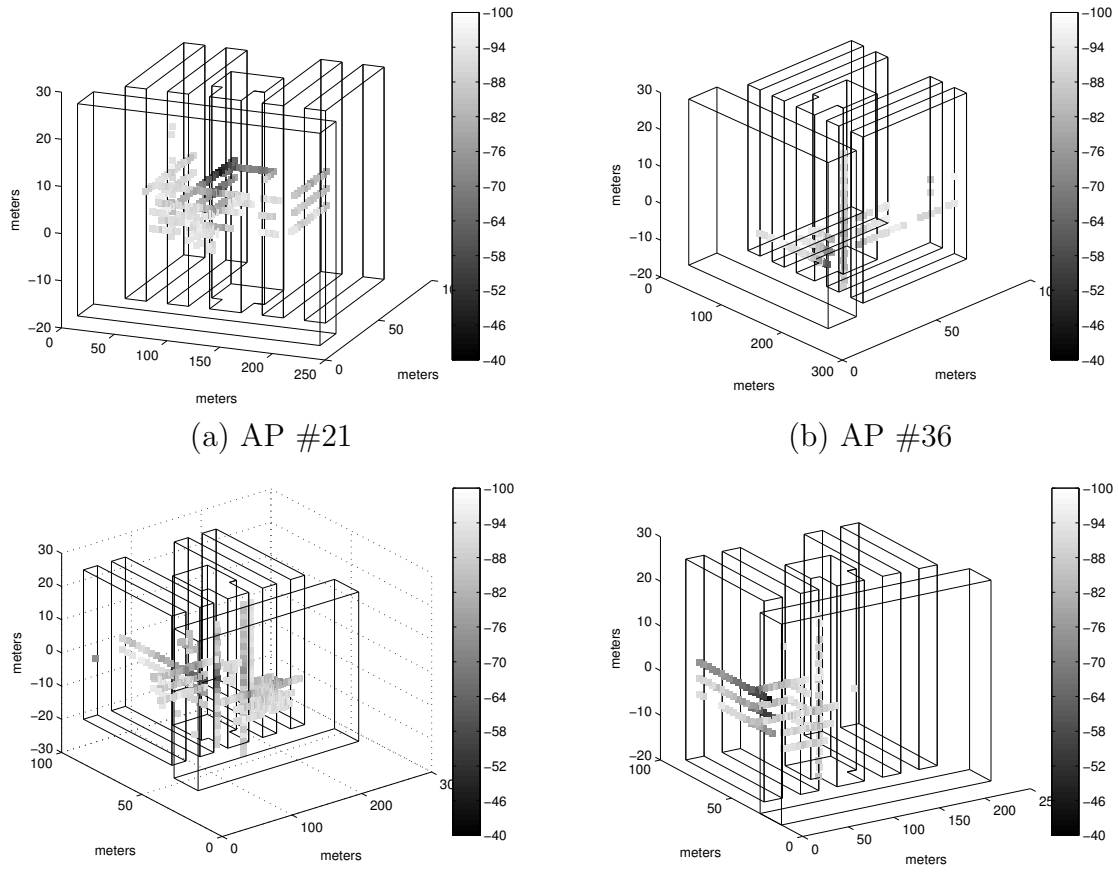

(a) AP #21

(b) AP #36

(c) AP #94

(d) AP #95

Figure 3.4: Examples of RSS (dBm) distribution in the building for different APs.

the data gathered on the lowest floor (black circles) from the data collected in the other two floors. However, the same is not possible for the data gathered in the remaining floors (the non-filled circles and the crosses). Analogous results (for WiFi samples collected data on one single floor) can be found in [32].

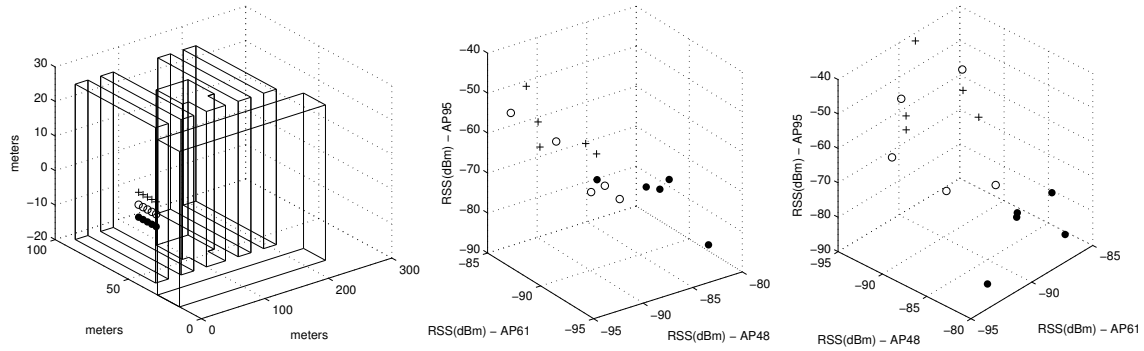

(a) (b) (c)

Figure 3.5: An example of how the Rfings distribute in the RSS space: (a) locations of selected measurement points in three different floors; (b) and (c) show the corresponding points in the 3-D RSS space (considering only APs #48, #61 and #95), with different viewing angles.

3.4 Clustering Techniques

If one estimates a position fix without clustering or any other search space reduction technique, then the Tfing would be compared with all Rfings stored in the CDB. With clustering, the position fix is performed in two phases:

(i) the Tfing is provided to the trained classifier, which identifies the cluster that the Tfing belongs to;

(ii) the Tfing is compared only to the Rfings belonging to the selected cluster.

In the first phase, the comparison is carried out in the subspace of the principal components. In the second phase, the comparison is performed in the N_w-dimensional RSS space. Those two phases correspond to steps 3 and 4 respectively in the scheme depicted in Fig. 3.2.

3.4.1 Number of Clusters

Considering that the computational complexity depends on the number of comparisons between RF fingerprints during a position fix, then the scheme using clustering

to restrict the search space within the CDB results in the reduction of the computational complexity of the DCM algorithm. Without clustering, each Tfing would be compared to N_p Rfings, where N_p is the number of RF fingerprints stored in the CDB. With clustering, each Tfing is compared, in the first phase, to N_c fingerprints, corresponding to the centers of each cluster. In the second phase, the Tfing is compared to the N_k Rfings belonging to the kth cluster ($k = 1, \ldots, N_c$) selected in the first phase.

In the system depicted in Fig. 3.2, PCA is employed as a compression technique so that one can process vectors with fewer components. The principal components (PCs) are computed considering all Rfings and its decomposition is not applied differently in each cluster, being the same for any Tfing fed to the localization engine. Therefore, the PCs do not change with N_c, being a characteristic of the building and the APs localization within the building. Therefore, the complexity of the search would be given by

$$\Gamma\left(N_c, N_k, N_p, C_{\mathrm{RSS}}, C_{\mathrm{PCA}}\right) = \begin{cases} C_{\mathrm{PCA}} N_c + C_{\mathrm{RSS}} N_k, & N_c > 1 \\ C_{\mathrm{RSS}} N_p, & N_c = 1 \end{cases}. \tag{3.3}$$

The C_{PCA} factor accounts for the complexity of comparing RF fingerprints in the PCA space, while C_{RSS} accounts for the complexity of the comparison in the RSS space. The optimum number of clusters would be the one that minimizes function Γ. Unfortunately, there is no analytical solution for this minimization problem and the values of N_k, $k = 1, \ldots, N_c$, would have to be explicitly considered. However, when using a Kohonen Layer with conscience, one may assume that the resulting clusters have a similar number of elements [47]. The experimental results will verify the validity of such assumption.

Let us evaluate the distribution of the number of elements per cluster resulting from the use of a Kohonen layer with conscience. Initially, let us group the collected RF data into 40 clusters. Fig. 3.6a and Fig. 3.6b show the number of elements per cluster for a Kohonen layer clustering approach, with and without conscience, respectively. In that example, adding conscience to the Kohonen layer reduces the standard deviation of the number of elements per cluster from 24 to just 5 points. These data suggest that, when using a Kohonen layer with conscience, the assumption that each cluster is composed of a similar quantity of elements is a reasonable one.

With that simplification and considering a database with N_p entries, each cluster would be composed by $\frac{N_p}{N_c}$ elements, in which case the computational complexity of the positioning method could be expressed as a function of the number of clusters

N_c as

$$\Gamma\left(N_c, N_p, C_{\mathrm{RSS}}, C_{\mathrm{PCA}}\right) = \begin{cases} C_{\mathrm{PCA}} N_c + C_{\mathrm{RSS}} \frac{N_p}{N_c}, & N_c > 1 \\ C_{\mathrm{RSS}} N_p, & N_c = 1 \end{cases}. \tag{3.4}$$

The theoretical optimal value of N_c is the one minimizing function Γ. By solving

$$\frac{\partial \Gamma}{\partial N_c} = 0 \tag{3.5}$$

one obtains

$$N_c = \left\lfloor \left(\frac{C_{RSS}}{C_{PCA}} N_p \right)^{1/2} \right\rfloor \tag{3.6}$$

which depends on the dimensions of the PCA and RSS spaces employed. However, one should note that depending on the distribution of the Rfings in the RSS space, and on the clustering technique applied, it might not always be possible to create a quantity of clusters equal to the theoretical optimal value provided by equation (3.6).

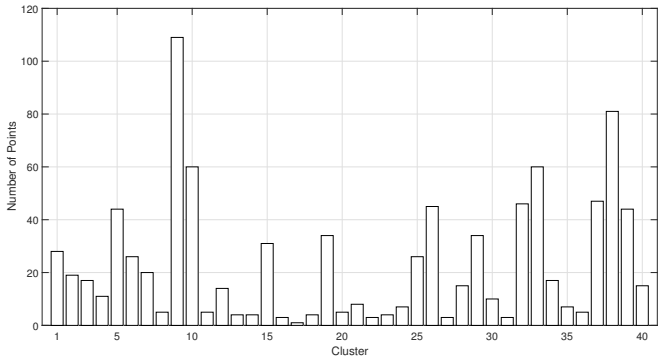

(a) Without conscience

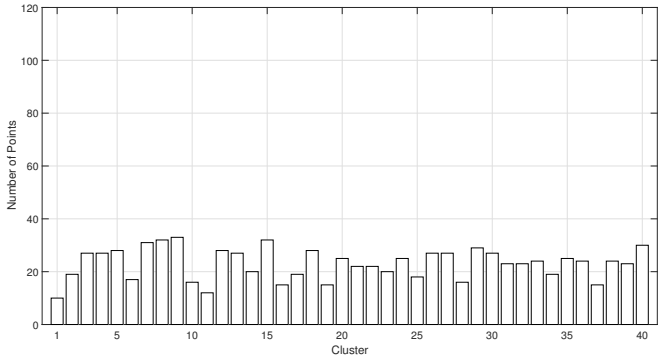

(b) With conscience

Figure 3.6: Number of points per cluster when using a Kohonen layer.

3.4.2 Unsupervised RSS Clustering

As each Rfing is georeferenced – i.e., associated with a measurement point with known (x, y, z) coordinates – by grouping Rfings in the N_w-dimensional RSS space, one is indirectly grouping the measurement points in the Euclidean 3-D space. Under certain propagation conditions, measurement points far away from each other in the Euclidean space might have RF fingerprints which are close together in the N_w-dimensional RSS space (or in the p-dimensional principal components subspace, where $p < N_w$). That is, due to the inherent complexity of the RF channel, it is not possible to know beforehand how the Rfings – and consequently the measurement points where they were gathered – will cluster in the RSS space. For instance, it is not possible to ascertain that measurement points on the same floor will belong to the same cluster, as illustrated in Fig. 3.5. Therefore, unsupervised clustering is employed here to allow collected Rfings to group freely in the RSS or natural space, without precluding – through the imposition of architectural constraints – any natural arrangement of the gathered fingerprints.

Three unsupervised clustering techniques are assessed in this section: K-medians [47], Kohonen layer and Kohonen layer with conscience [48].

K-Medians is a variation of K-means, which is a classic unsupervised clustering technique. Both follow the same steps:

(i) N_c clusters centers are defined;

(ii) for each input vector, the distances between the vector and each cluster center are calculated;

(iii) the input vector is associated with the cluster whose center is the closest one.

Steps **(ii)** and **(iii)** are repeated for every input vector. At the end of the first epoch, i.e., after all input vectors have been presented to the classifier once, the clusters centers are re-calculated, as well as the distances between each input vector and the new clusters centers. If any vector switches clusters, the process is repeated until no vector switches clusters or until a maximum number of epochs is reached. The difference between K-means and K-medians lies on how the clusters centers are calculated. Whilst in K-means, the clusters centers are given by the barycenter of the vectors of each cluster, in K-medians, instead of the arithmetic mean, the median is used. The advantage of using the median is that it is a more robust estimator, less susceptible to outliers, i.e., input vectors with much noise [48].

The Kohonen layer used in this work is one-dimensional with a neighbor radius equal to zero, which means that only the winner neuron is activated. As Fig. 3.7 shows, this classifier has an input layer and a competitive layer. For each input vector $\mathbf{x} = [x_1\, x_2 \ldots x_N]$, the winner neuron at the competitive layer is the one

whose synapse $\mathbf{w}_i$ is the most similar to the input vector $\mathbf{x}$. Each synapse (or synaptic weight) $\mathbf{w}_i$, $i = 1, \ldots, M$, is an N_w-component vector, just like the input vector $\mathbf{x}$. The output of the winner neuron is activated (y_i=1), while the outputs of all other neurons remain equal to zero (y_j=0, $\forall j \neq i$) [49]. The similarity measure used in the neurons is

$$u_i = -\left[w_{i,0} + (\mathbf{x} - \mathbf{w}_i)(\mathbf{x} - \mathbf{w}_i)^T\right], \forall i \in [1, \ldots, N_c] \tag{3.7}$$

where $w_{i,0}$ is the ith neuron conscience bias, which is defined by equation (3.15), and N_c is the number of neurons in the Kohonen layer.

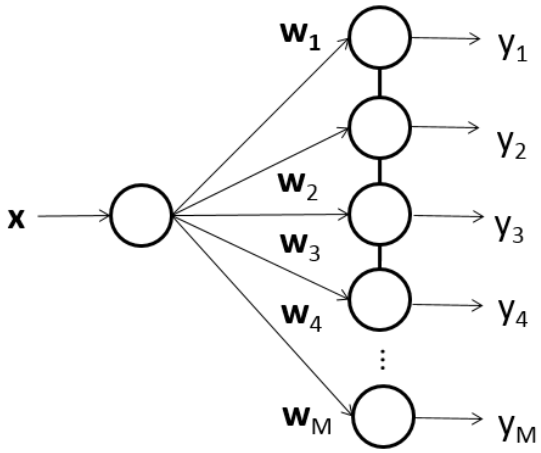

Figure 3.7: Example of a Kohonen layer (input layer + competitive layer).

Just like in K-means, the initialization of the synaptic weights is critical for the algorithm convergence. Section 3.6 describes the technique used for the initialization. To distribute the training approximately evenly among all neurons in the competitive layer, conscience is used [47]. With conscience, neurons which are constantly winning receive a progressively decreasing negative *bias*. This allows less trained neurons to become more similar to the input vectors. With the conscience mechanism, neurons in the Kohonen layer naturally represent approximately equal amount of information [50]. To improve the algorithm convergence, individual decreasing learning steps per neuron are also used [49].

3.5 Floor Classification using Committees of Feed-Forward ANNs

The Kohonen layer and K-medians are used to cluster the target RF fingerprints in an unsupervised manner. After training, each neuron in the Kohonen layer (or

each cluster center in K-medians) maps one cluster within the CDB. Fig. 3.8 shows some clusters in the RSS space. It is important to note that clusters in the RSS space might span several floors. Moreover, in multi-floor indoor positioning, it is crucial to correctly identify the floor where the MS is located, before estimating the MS 2-D position on that floor. It is particularly relevant for certain types of positioning applications, such as emergency call location [35, 36] and applications designed to help blind people locate the floor they are in [37]. Unlike clustering in the natural or RSS space, the grouping of the Tfings into distinct floors can be done in a supervised way, as the targets - i.e., the floor at which each Tfing was collected - are known before hand.

A common practice to design classifiers aiming at pre-defined outputs (as the floor number is) is the use of supervised clustering systems. A usual strategy for that are feed-forward ANNs. Therefore, the proposed location engine uses committees of feed-forward ANNs to identify the floor where the MS might be located, within the selected cluster (indicated by the Kohonen layer). The output of the joint classifier – the committee – is expected to be more accurate and show a smaller variance than any of its individual binary classifiers [38, 51]. There are several strategies to combine the output of the individual ANNs composing a committee [52]. The one selected here, for its simplicity and performance, is majority voting.

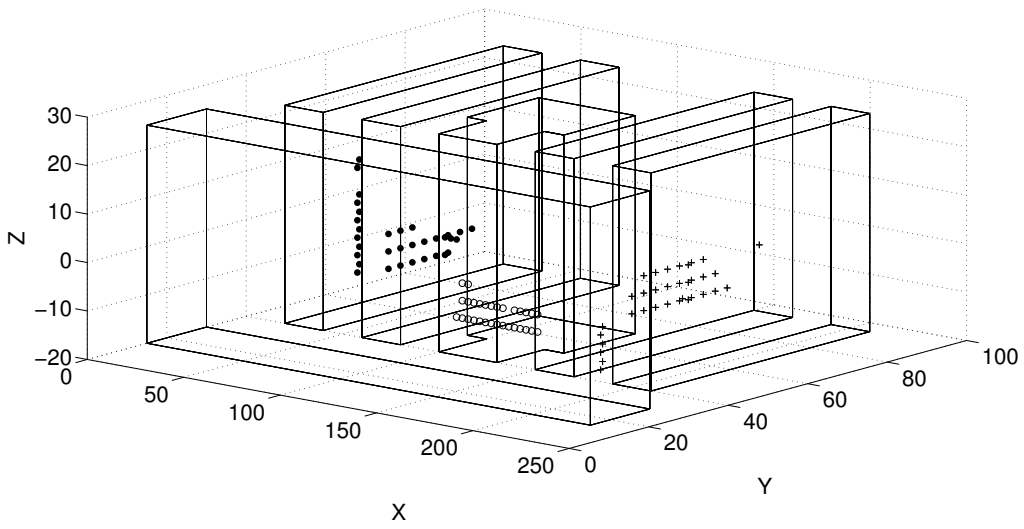

Figure 3.8: Examples of clusters defined by the Kohonen layer and that span several floors. All distances are expressed in meters.

Each of the N_l floors has a committee with N_a feed-forward ANNs. Each ANN is trained as a binary classifier, identifying if a given RF fingerprint belongs to the current floor (output 1) or not (output 0). On the lth floor, the outputs $g_{j,l}$ of the individual classifiers, where $j \in [1, \ldots, N_a]$ and $l \in [1, \ldots, N_l]$, are combined into a

unique majority voting classifier, whose output g_l^v is the class which the majority of the single classifiers voted for, i.e.,

$$g_l^v = \begin{cases} 0 \ , \text{ if } \sum_{j=1}^{N_a} g_{j,l} < \frac{N_a}{2} \\ 1 \ , \text{ if } \sum_{j=1}^{N_a} g_{j,l} \geq \frac{N_a}{2} \end{cases} . \tag{3.8}$$

In some spurious and rare situations, it might happen that two or more committees vote 1 (a Tfing cannot belong to more than one floor), or all committees vote 0 (a Tfing must belong to a floor). In these cases the committee with the largest joint output – i.e., having the highest number of ANNs voting 1 – wins.

3.6 Experimental Evaluation

During the data collection campaign described in Section 3.3, WiFi samples were gathered at 924 different points. At each point up to 240 WiFi scans were collected. From these the first 50 scans are used as input vectors of the positioning system, i.e., they compose the test set. The rest is used to build the CDB entries (the Rfings) and train the system [2]. After that, the proposed location engine is evaluated using these data.

3.6.1 Rfings Definition

The CDB entries are composed of averages of RSS values from each AP collected at N_p georeferenced points. In this sense, the ith CDB entry is given by the 4-tuple $(\mathbf{f}_i, x_i, y_i, z_i)$, where

$$\mathbf{f}_i = [\overline{\text{RSS}}_{i,1} \ \ldots \ \overline{\text{RSS}}_{i,N_w}] \tag{3.9}$$

and N_w is the number of distinct WiFi networks detected during the data collection and $\overline{\text{RSS}}_{i,k}$ is the kth AP mean RSS level at the ith measurement point, given by

$$\overline{\text{RSS}}_{i,k} = \frac{1}{N_{i,k}} \sum_{h=1}^{N_{i,k}} \text{RSS}_{i,k,h} \tag{3.10}$$

where $i = 1, \ldots, N_p$, $k = 1, \ldots, N_w$, $\text{RSS}_{i,k,h}$ is the RSS level of the kth AP at the hth WiFi scan collected at the ith point, and $N_{i,k}$ denotes the number of occurrences of network k at point i[3].

[2] Therefore, approximately 20% of the samples collected at each point is reserved for the test set, while 80% composes the validation and test set. This 20%–80% figure is typically used in machine learning.

[3] i.e., the number of WiFi scans gathered at the ith point in which the kth AP was detected.

3.6.2 PCA Data Conditioning for the Clustering Processes

Both the Tfings given to the classifier and the Rfings stored in the CDB are composed of RSS values ranging from -120 to -30 dBm. As Fig. 3.2 shows, PCA is applied to reduce the number of components of the input vectors. PCA generates a new set of mutually orthogonal variables called principal components (PCs). First, the training set, with N_p input vectors, is translated by extracting the sample mean at each dimension, obtaining matrix

$$\mathbf{R} = \left[\overline{\mathrm{RSS}}_{i,k} - \overline{\mathrm{RSS}}_k\right]_{i=1,\ldots,N_p \;;\; k=1,\ldots,N_w} \tag{3.11}$$

where $\overline{\mathrm{RSS}}_{i,k}$ is the kth WiFi network RSS mean value at the ith point – calculated as defined by equation (3.10) – and $\overline{\mathrm{RSS}}_k$ is the kth network RSS sample mean for all measurement points, i.e.,

$$\overline{\mathrm{RSS}}_k = \frac{1}{N_p} \sum_{i=1}^{N_p} \overline{\mathrm{RSS}}_{i,k} \tag{3.12}$$

Let the $N_w \times 1$ column vector $\mathbf{u}_j$ be the jth eigenvector of the covariance matrix of $\mathbf{R}$. The PCs matrix of the training set is then given by

$$\mathbf{P} = \mathbf{R} \cdot \left[\mathbf{u}_j\right]_{j=1,\ldots,N_w} \tag{3.13}$$

Both $\mathbf{R}$ and $\mathbf{P}$ are $N_p \times N_w$ matrices. The columns in $\mathbf{P}$ are sorted in descending order of variance, each one of them corresponding to a PC. To reduce the training patterns dimension, only the first p PCs are held. The value of p was selected so that at least 99% of the training set total variance was preserved, resulting in $p = 78$.

The sample means $\overline{\mathrm{RSS}}_k$, $k = 1, \ldots, N_w$, and matrix $\left[\mathbf{u}_j\right]_{j=1,\ldots,N_w}$, both obtained during the application of PCA to the training set, are also used to project each vector of the validation and test sets into the subspace of PCs. As with the training set, only the first p PCs are held.

3.6.3 Training the Unsupervised Classifier

The cluster central patterns, in the case of the K-medians, or the synaptic weights, in the case of the Kohonen layer, are defined in the PCs subspace. So, there is a $N_c \times p$ matrix of cluster central patterns, where N_c is the number of clusters and p is the number of PCs that are kept ($p = 78$). The theoretical optimum value of N_c is given by equation (3.6). For $N_p = 924$, and assuming $C_{\mathrm{RSS}} = N_w = 136$ and $C_{\mathrm{PCA}} = p = 78$, one has $N_c = 40$.

For the initialization of the clusters central patterns in the PCs subspace, the

maximum variance dimension (the first PC) has been divided into N_c equal length sections. In each section, the input vector (from the training set) whose first PC value is closest to that section median is selected. The chosen input vectors provide the initial values for the N_c clusters central patterns [53].

During the Kohonen layer training, individual decreasing learning steps per synapse were used, as defined by

$$\psi_i(t) = \psi_0 \exp(-t/N_0) \tag{3.14}$$

where $\psi_i(t)$ is the ith synapse learning step at iteration t, $\psi_0 = 0.45$ and $N_0 = 120$. The values of ψ_0 and N_0 were empirically set so that the neurons' individual learning steps did not decrease too fast – which would lead to a premature convergence to a bad solution – neither too slowly, in which case the synapses vectors would be bouncing around the optimal solution, without ever reaching it.

Conscience was used in the training phase. Conscience is implemented by adding a negative bias to the neuron similarity function, which is defined by equation (3.7). The negative bias is given by

$$w_{i,0} = \Delta^2 \{0.5 [1 - \tanh(k(p_i - p^*))] - 1\}, \tag{3.15}$$

where Δ is equal to the diameter of the single class[4] in the PCs subspace, p_i is the percentage of the ith neuron training [5], $p^* = 1/N_c$ and $k = 4.5$. Function $\tanh(x)$ is the hyperbolic tangent of x.

At each training epoch, all $N_p = 924$ training patterns are presented to the Kohonen layer. Training continues until a maximum number of epochs has been reached (20 epochs), or the maximum variation of the synaptic weights between two consecutive epochs is below a given threshold (0.0001).

After that, the performances of the three non-supervised classifiers – K-medians, Kohonen layer and Kohonen layer with conscience – are assessed. Fig. 3.9 shows the total internal dispersion per cluster ($S_{\text{Int},k};\ k = 1, \ldots, N_c$), as defined by

$$S_{\text{Int},k} = \sum_{j=1}^{N_k} \|\mathbf{x}_{k,j} - \mathbf{m}_k\|^2, \tag{3.16}$$

where N_k is the number of elements in the kth cluster, $\mathbf{x}_{k,j}$ is the jth element of the kth cluster, and $\mathbf{m}_k$ is the arithmetic mean of the elements in the kth cluster. The total internal dispersion of a cluster is a measure of the similarity among that

[4]This diameter is equal to the largest distance between any pair of input vectors.

[5]The number of times the neuron won, i.e., was activated, over the total number of input vectors presented to the classifier.

cluster elements. The total internal dispersion for all clusters, given by

$$S_{\text{Int}} = \sum_{k=1}^{N_c} S_{\text{Int},k} \tag{3.17}$$

is a parameter to be minimized during the classifier training. Among the three evaluated classifiers, the Kohonen layer with conscience is the one that produces the lowest total internal dispersion ($\text{S}_{\text{Int}} = 1.64 \times 10^6$), followed by the Kohonen layer without conscience ($\text{S}_{\text{Int}} = 1.86 \times 10^6$) and by K-medians ($\text{S}_{\text{Int}} = 1.99 \times 10^6$).

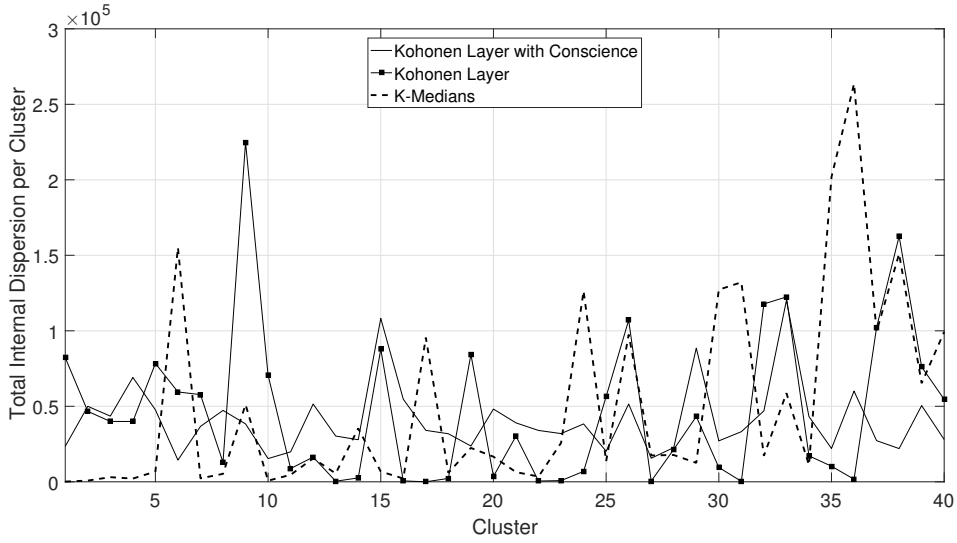

Figure 3.9: Total internal dispersion per cluster.

Another parameter used to evaluate the classifier performance is the accuracy, defined by the ratio of correct classifications over the total number of input vectors N_{Tfing}. So, the accuracy is given by the ratio $(\text{TP} + \text{TN})/N_{\text{Tfing}}$, where TP is the number of true positives (*number of input vectors belonging to a given cluster and which are properly identified as such*) and TN is the number of true negatives (*number of input vectors not belonging to a given cluster and which are correctly identified as such*). Fig. 3.10 shows the accuracy per cluster per classifier. The Kohonen layer with conscience achieves the best results, reaching accuracies higher than 99% in 39 out of 40 clusters.

From equation (3.4), it is possible to calculate a factor κ_{max}, which expresses the theoretical maximum reduction of computational complexity achieved by the proposed location engine in comparison to pure DCM positioning. This maximum would be reached if all clusters had the same number of elements, and is given by

$$\kappa_{max} = \frac{\Gamma\left(1, N_p, C_{\text{RSS}}, C_{\text{PCA}}\right) - \Gamma\left(N_c, N_p, C_{\text{RSS}}, C_{\text{PCA}}\right)}{\Gamma\left(1, N_p, C_{\text{RSS}}, C_{\text{PCA}}\right)} \tag{3.18}$$

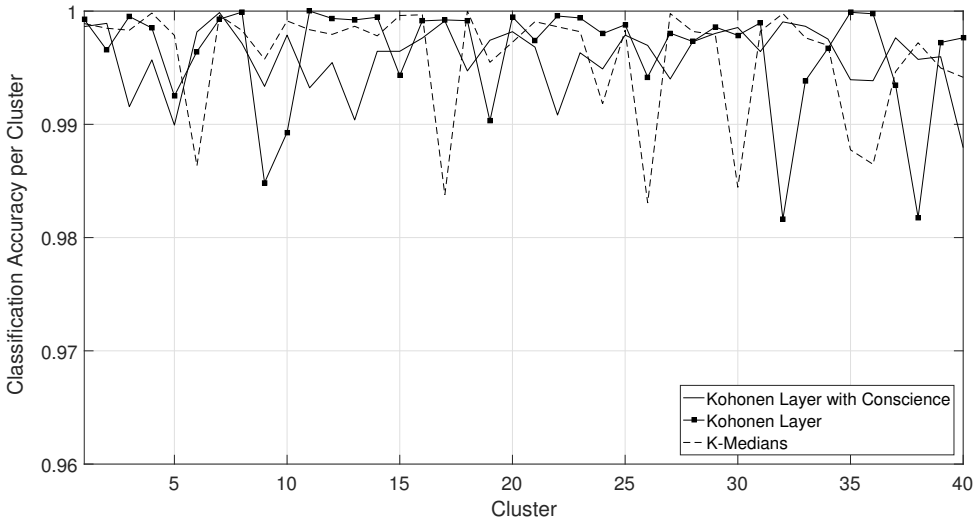

Figure 3.10: Classification accuracy per cluster.

For $N_p = 924$ and $N_c = 40$, $\kappa_{max} = 95\%$. However, clusters do not necessarily have the same number of elements, so the computational complexity reduction factor is given by

$$\kappa = \frac{N_{\text{Tfing}} \cdot \Gamma\left(1, N_p, C_{\text{RSS}}, C_{\text{PCA}}\right) - \left[N_{\text{Tfing}} \cdot C_{PCA} \cdot N_c + C_{RSS} \cdot \sum_{i=1}^{N_{\text{Tfing}}} n_i\right]}{N_{\text{Tfing}} \cdot \Gamma\left(1, N_p, C_{\text{RSS}}, C_{\text{PCA}}\right)} \tag{3.19}$$

where n_i is the number of elements in the cluster which the ith Tfing was associated with, and N_{Tfing} is the number of Tfings. Note that κ will always be less than κ_{max}, as long as the number of Tfings per measurement point is constant. The experimental value of κ was assessed for the three classifiers: Kohonen layer with conscience (94.9%) and without conscience (92.3%), and K-medians (92.2%). The Kohonen layer with conscience is the classifier which most reduces the computational complexity of the DCM algorithm, almost reaching κ_{max}. It happens because conscience tends to make the neurons in the competitive layer map equal regions of the input space, resulting in clusters with approximately the same number of elements. This result confirms the reasonability of the assumption made in Section 3.4.1, that the number of elements per cluster would be approximately the same when using a Kohonen layer with conscience.

Table 3.1 summarizes the results of the evaluation of the three non-supervised clustering techniques. Regarding accuracy, their performances are quite similar, but the Kohonen layer with conscience achieves the lowest accuracy standard deviation, and, more importantly, the highest minimum accuracy (98.8%) among all assessed classifiers. Moreover, as seen in Fig. 3.10, the Kohonen Layer with conscience has

an accuracy below 99% in just one out of 40 clusters. It also has the lowest average internal dispersion per cluster, and achieves the highest computational complexity reduction (94.9%), almost reaching the theoretical optimum value $\kappa_{max} = 95\%$. For those reasons, the Kohonen layer with conscience was the selected non-supervised clustering technique for the proposed location engine.

Table 3.1: Evaluation of the non-supervised classifiers.

	Dispersion / cluster			Accuracy / cluster			Complexity
	Average	Std.Dev.	Max.	Average	Std.Dev.	Min.	Reduction
K-Medians	4.9×10^4	6.4×10^4	2.6×10^5	99.6%	0.005%	98.3%	92.2%
Kohonen Layer	4.6×10^4	5.1×10^4	2.2×10^5	99.6%	0.004%	98.2%	92.3%
Kohonen Layer with Conscience	4.1×10^4	2.3×10^4	1.2×10^5	99.6%	0.002%	98.8%	94.9%

3.6.4 Training the Committees of Feed-Forward ANNs

For each of the 13 floors, there is a joint majority voting classifier composed by a committee of $N_a = 7$ ANNs. So, there are 91 single binary classifiers, evenly divided into $N_l = 13$ committees. The optimum size of classifiers per committee ($N_a = 7$) was determined by increasing the number of classifiers during the training phase until no further relevant improvement in floor identification accuracy was detected, as Fig. 3.11 shows.

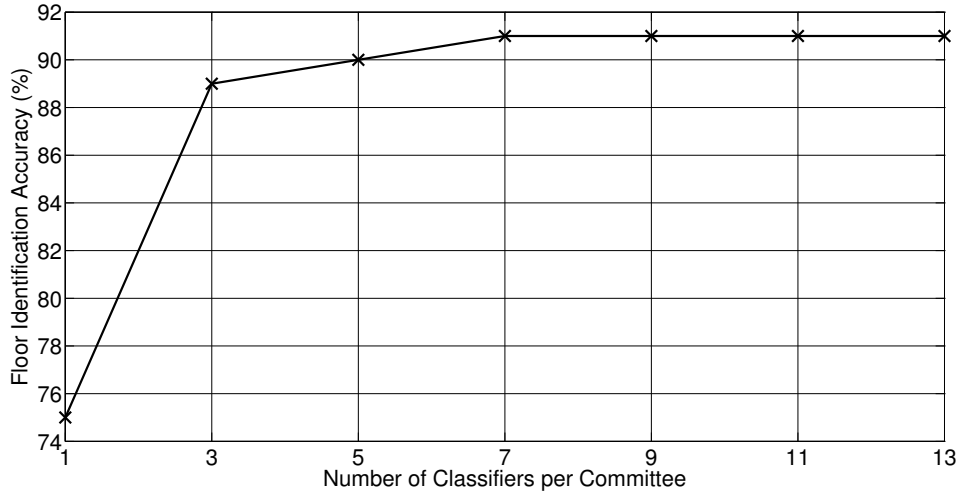

Figure 3.11: Floor identification accuracy as a function of the ANN committee size.

All ANNs have the same topology, with $p = 78$ inputs, $q = 10$ neurons in the hidden layer and one neuron in the output layer. The activation function of all neurons is the hyperbolic tangent. The training method is Levenberg-Marquardt backpropagation [54], with mean squared error (MSE) as the performance function.

The optimum size of the hidden layer was determined by increasing the number of neurons during the training phase, until no further relevant reduction in the MSE was detected. Training continues until one of the following conditions is met:

(i) a maximum number of epochs is reached (50 epochs);

(ii) the MSE reaches a goal (equal to or below 0.01);

(iii) a maximum number of consecutive validation fails occur (6 fails).

Of the total $N_p = 924$ Rfings in the CDB, N_j belong to the jth floor and $(N_p - N_j)$ belong to other floors. As there are 13 floors, $N_j < (N_p - N_j)$. So, to prevent biasing the training of the classifiers in the jth floor voting committee, the Rfings belonging to the jth floor are repeated $\lfloor \log_2 \left[(N_p - N_j) / N_j \right] \rfloor$ times. So, the training sets for each g_j^v are such that the number of Rfings that belong to the jth floor will be approximately the same of the remainder Rfings in the CDB. Therefore, each committee has a different training set.

Validation vectors are used to prevent overtraining [49]. They stop training early if the network performance on the validation vectors fails to improve or remains the same for a maximum number of consecutive epochs. Within the training set of each ANN, 10% of the Rfings are randomly selected for the validation set. Therefore, not only each committee has a different training set, but also each ANN within each committee.

The output of each ANN is a hyperbolic tangent function, which is continuous within the range $[-1, +1]$. The location engine assumes that a classifier has voted 1 (Tfing belongs to the current floor) if its output is positive, and 0 if otherwise. The joint output of a committee is defined by equation (3.8).

3.6.5 Experimental Positioning Accuracy

2-D Positioning Accuracy

The planar or 2-D positioning accuracy is given by the Euclidean distance between the estimated and the real location of the target MS when both locations are on the same floor[6]. Fig. 3.12 compares the experimental 2-D positioning error cumulative distribution function (CDF) of the following implementations:

(I) Pure DCM, which carries out in the RSS space the correlation of the Tfing with the Rfings composing the CDB, without applying any search space reduction technique;

[6] i.e., when the floor where the target MS is located has been properly identified.

(II) DCM with unsupervised search space reduction, using a Kohonen Layer with conscience [55];

(III) Proposed location engine, with a two-stage search space reduction technique: unsupervised clustering (Kohonen Layer with conscience) and supervised classification (committees of feed-forward ANNs). The first stage allows for the Rfings to group freely (without the imposition of architectural constraints) in the RSS space. The second stage allows for floor identification. DCM provides the position estimate within the selected floor.

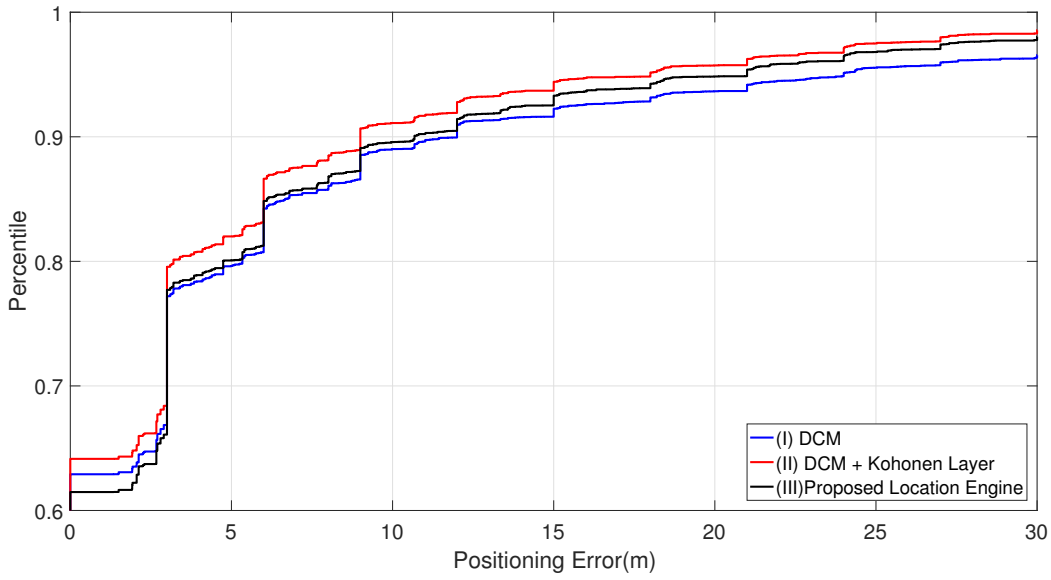

Figure 3.12: CDF of the 2-D positioning error.

Fig. 3.12 shows that all methods have approximately the same planar positioning error distribution[7]. However, this 2-D error metric can be misleading, as it considers only the location estimates where the floor has been correctly identified. As Table 3.2 indicates, such correct identification rises from 78% in pure DCM (I) to 91% in the proposed scheme (III). Thus, Fig. 3.12 compares the location error for different sets of points. The following subsection defines an alternative metric, in an attempt to better compare the positioning error of the evaluated methods.

2.5-D Positioning Accuracy considering Architectural Aspects

One might use the 2-D Euclidean distance to assess planar location errors in multi-floor positioning, as it does provide a valid error metric when both the real and

[7]One might note some discontinuities in the CDF plots. Those occur because the test points distribution is discrete, forming a planar grid with 3 meters separation between adjacent points. In fact, the largest "jump" occurs precisely at 3 meters. Smaller discontinuities occur at multiples of that distance.

Table 3.2: 2-D positioning error in meters and floor identification accuracy.

Method	Avg Error	90th Percentile	Floor Id Accuracy	Floor acc. within ±1	Floor acc. within ±2
(I)	4.0	12.0	78%	93%	97%
(II)	3.0	9.0	85%	95%	98%
(III)	3.5	11.0	91%	97%	99%

estimate MS position lie on the same floor. However, when considering all position estimates, its 3-D extension (the 3-D Euclidean distance) is not suitable, as it does not account for building architectural aspects. Consider the following example. In a building with N_l floors, an MS placed at coordinates (x, y, l) has a position estimate given by coordinates $(\hat{x}, \hat{y}, \hat{l})$, where the first two components of the 3-tuple provide the planar coordinates in meters, and the third indicates the floor number. Assuming that each floor has a height of L meters, the 3-D Euclidean distance between the real and estimated MS location is

$$\hat{e} = \sqrt{(x-\hat{x})^2 + (y-\hat{y})^2 + \left[L \cdot \left(l - \hat{l}\right)\right]^2} \tag{3.20}$$

However, the distance that somebody going from the estimated to the actual MS locations would have to traverse is larger than the one provided by equation (3.20), as one cannot follow a straight line between the two points, passing through the floors and walls. In calculating the real traversed distance, one must account for the building architectural aspects. Assuming, for simplicity, that there are no inner walls on each floor[8] and that a lift is the only connection between floors, this distance becomes

$$\hat{e} = \sqrt{(\hat{x} - x_{\text{shaft}})^2 + (\hat{y} - y_{\text{shaft}})^2} + L \cdot \left(\hat{l} - l\right) + \sqrt{(x_{\text{shaft}} - x)^2 + (y_{\text{shaft}} - y)^2} \tag{3.21}$$

where the first term accounts for the planar distance between the estimated MS location and the lift, the second term represents the vertical distance between the estimated and real floors, and the third term expresses the planar distance between the lift and the real MS location. The pair $(x_{\text{shaft}}, y_{\text{shaft}})$ are the lift shaft planar coordinates.

Fig. 3.13 shows the CDF of the 2.5-D position error, using the metric given by equation (3.21) with the aforementioned assumptions[9]. Here the improvement provided by method (III) becomes evident: while 80% of the location estimates of method (III) have a 2.5-D error below 9 meters, the error for that same percentile

[8] i.e., one is assuming that it is possible to follow a straight line from any point to the lift shaft.

[9] At UERJ's main building, $L \approx 3.6$ meters and there are several elevator shafts. For this analysis, only the shaft at $(x_{\text{shaft}}, y_{\text{shaft}}) = (123.2, 50)$ has been selected (see Figure 3.3).

rises to 15 meters and 51.5 meters in methods (II) and (I), respectively. This result is directly related to the higher floor identification accuracy achieved by method (III).

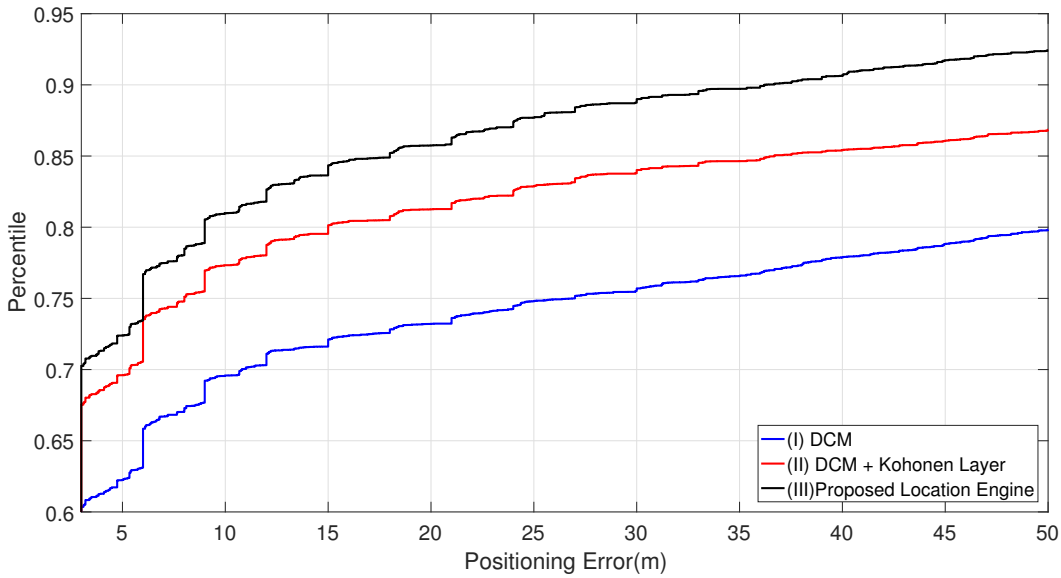

Figure 3.13: CDF of the 2.5-D positioning error.

3.6.6 Use of Averaged Target Fingerprints

In practical positioning systems, there may be a compromise between the time required to provide a position fix and the attained accuracy, not just in terms of the employed positioning algorithm but also regarding the time spent collecting the necessary data. The collection of several WiFi scans falls in this category. It is natural to expect that the larger the gathering interval (which augments the time required to provide the position fix), smaller is the error in the obtained position. This alternative may cope with variations of RSS levels, typically observed in indoor scenarios [56]. For example, in [13] the use of a moving average to filter subsequent RSS scans to composing the target fingerprint is investigated. Other works apply the term "windowing" to this process [35, 40, 42, 43] since the RSS data gathered in distinct scans within a time window are averaged to compose the Tfing. This section briefly assesses the effect of employing time windows for averaging collected data to compose Tfings. The localization system is not changed in any sense nor retrained for this, just the Tfings are different (averages) from the ones employed in the previous subsection, which were composed of a single RSS scan. The results are evaluated using the same metrics as in the previous subsection.

Tables 3.3, 3.4 and 3.5 present the outcome of these tests. In Table 3.5 the

window length column indicates the number of RSS subsequent measurements that are averaged to compose the Tfing fed to the localization system. Columns "Floor acc. $\pm n$" ($n = 1, 2$) indicate the percentage of cases in which the estimated floor is within n floors of the real floor, i.e., n floors above or n floors below.

As one can note, as the window length increases the localization error diminishes and the floor identification accuracy increases. However, this is done at the expense of larger time to produce a position fix. Whilst this presents no problem for the location of static MSs, it may be an issue for non-stationary MSs tracking.

Table 3.3: 2-D positioning error as a function of the window length.

Method	Window Length	Avg Error (m)	90th Percentile (m)
(I)	1	4.0	12.0
	5	2.6	6.1
	10	2.1	5.4
	25	1.2	3.0
(II)	1	3.0	9.0
	5	2.0	6.0
	10	1.6	3.5
	25	1.0	3.0
(III)	1	3.5	11.0
	5	2.3	6.1
	10	1.8	5.4
	25	1.1	3.0

Table 3.4: 2.5-D positioning error (considering architectural aspects) as a function of the window length.

Method	Window Length	Avg Error (m)	90th Percentile (m)
(I)	1	27.4	116.4
	5	19.3	80.6
	10	16.0	62.1
	25	9.9	12.0
(II)	1	18.8	74.6
	5	12.8	39.2
	10	10.2	21.0
	25	5.6	5.9
(III)	1	12.0	36.2
	5	8.2	18.2
	10	6.4	11.0
	25	4.1	4.7

Table 3.5: Floor identification accuracy as a function of the window length.

Method	Window Length	Floor Id Accuracy	Floor acc. within ±1	Floor acc. within ±2
(I)	1	78%	93%	97%
	5	85%	95%	98%
	10	87%	96%	99%
	25	92%	98%	99%
(II)	1	85%	95%	98%
	5	89%	97%	99%
	10	91%	97%	99%
	25	95%	98%	100%
(III)	1	91%	97%	99%
	5	93%	98%	99%
	10	95%	98%	99%
	25	97%	99%	100%

3.6.7 Assessing Empirical Computational Complexity Reduction through Processing Time

This section compares the processing time of methods (I), (II) and (III). This provides an empirical measure of the computational complexity reduction achieved by methods (II) and (III), in respect to method (I) [57]. The processing time reduction percentages are correlated with the theoretical formulation of the computational complexity reduction factor κ, defined by equation (3.19). Both the theoretical formulation and the empirical measure are calculated with the dataset described in Section 3.3. Though there is no proof that those results will hold for any distribution of test points in any building, the very size of the test set provides reasonable confidence to the comparison results, without loss of generality.

Table 3.6 informs the absolute processing time (cumulative for all 46200 samples in the test set) for each method at each stage:

1. presenting the input patterns in the PCA space to the Kohonen layers;
2. forwarding the input patterns in the PCA space to the committees of MLPs;
3. comparing in the RSS space the target and reference fingerprints contained in the reduced search set.

One sees that the additional time spent in stage 2 in method (III) (proposed location engine) is more than compensated by the reduction of the search space size in relation to methods (I) (pure DCM) and (II) (DCM+Kohonen). Table 3.6 also informs the average reduction of processing time achieved by methods (II) and (III) in relation to method (I). Figure 3.14a displays the processing time per position fix using methods (I) and (III). Figure 3.14b shows the reduction in processing

time achieved by method (III) in relation to method (I). The proposed location engine attains the highest reduction, 86.8%. This result is just 8.1% lower than the theoretical value of $\kappa = 94.9\%$ indicated in Table 3.1.

Table 3.6: Total processing time (seconds) per stage and average processing time reduction in relation to method (I).

Method	Stage 1	Stage 2	Stage 3	$\Delta(\%)$
(I)	0	0	74.8	0
(II)	7.5	0	2.7	86.4
(III)	7.5	0.9	1.5	86.8

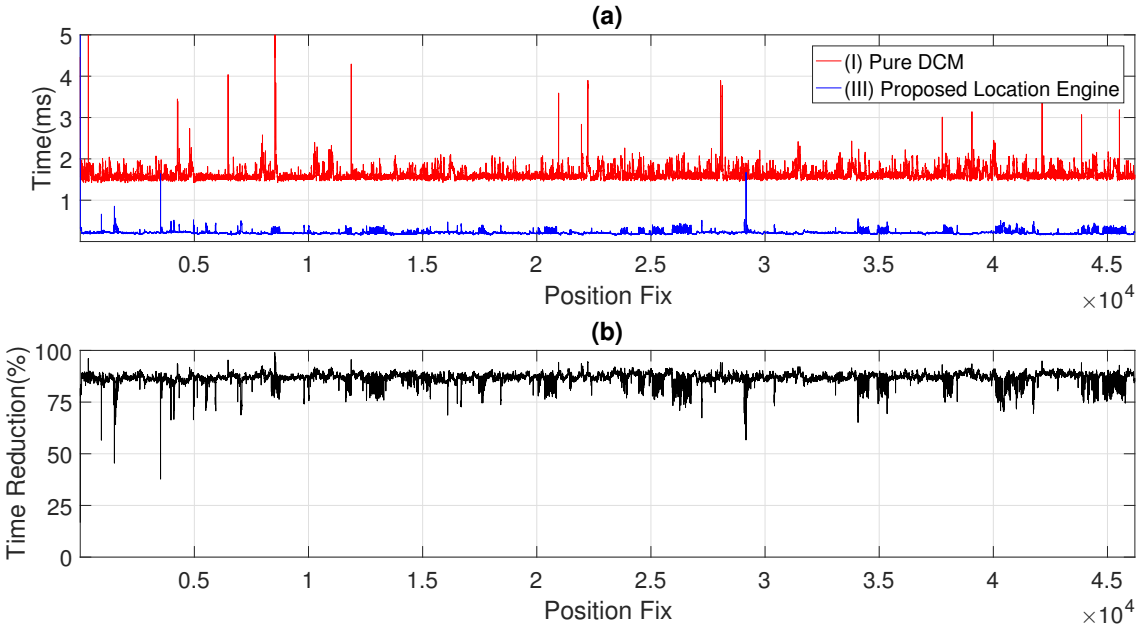

Figure 3.14: (a) Processing time per position fix; (b) Relative reduction in time per position fix.

3.6.8 Comparison with Other Published Results

There is a wide list of papers about the RF indoor positioning problem, but, surprisingly, only a few addressing multi-floor scenarios. On this section some of the very few papers on WiFi indoor localization that address the multi-floor scenario are assessed. Tables 3.7 and 3.8 summarize their features. The first eight lines of Tables 3.7 and 3.8 bring the characteristics of each experiment:

(i) reference to the paper where it was published;

(ii) the positioning technique that was used;

(ii) the search space reduction technique (if applicable);

(iv) the number of floors covered in the test;

(v) the number of calibration points, i.e., the number of locations where RF fingerprints were gathered during the off-line training phase;

(vi) the number of collected RF fingerprints, i.e., the number of samples (WiFi scans), obtained during the off-line phase;

(vii) the number of test points, i.e., of locations where WiFi scans were gathered during the test phase;

(viii) the window length, i.e., the number of Tfings that were used to yield each position fix; if the window length was N, then the RSS values of N Tfings were averaged; the resulting Tfing was then compared to the Rfings in the search space.

The last two lines list the experimental results: the floor identification accuracy and the 2-D mean positioning error. Within Tables 3.7 and 3.8 a (-) indicates that the information was not provided in the reference and (n/a) indicates that the parameter does not apply to the location technique.

In [11] the authors developed an RSS-based multi-lateration positioning system called SaskEPS (Saskatchewan Enhanced Positioning System). It achieved 100% floor identification accuracy, in a testbed comprising two buildings with three floors each; 25 test points were selected per floor per building, totalizing 150 test locations. As it is not a DCM technique, SaskEPS does not demand an off-line training phase. The system, however, requires careful calibration of the propagation models used to estimate the distance between the target MS and each of the APs listed in the WiFi scan, and that the coordinates of all APs are very accurately known – this latter requirement might be prohibitive in some scenarios [31].

In [39] the authors used a Bayesian Graphic Model (BGM) to obtain position fixes. Such implementation does not require an off-line training phase. As they do not need an initial profiling to populate the CDB with fingerprints, single-phase implementations are also referred to as zero profiling techniques [30]. The authors reported an average planar positioning error of 2.3 meters in a testbed with 600 samples gathered in 30 test points distributed in two floors. The floor identification accuracy was not informed.

In [41] the authors applied a hybrid two-step technique, combining DCM for floor identification (first step) with RSS multi-lateration for 2-D positioning (second step). Unlike the SaskEPS system [11], where the locations of the APs needed to be known *a priori* and with high accuracy, the system presented in [41] is capable of

estimating the unknown AP coordinates on-the-fly, before triangulating the target MS location. A floor identification accuracy of 100% was reported, but just three test points were used. RSS triangulation estimates the APs locations. Other alternatives for obtaining the APs coordinates are presented in [58, 59].

In [42] the authors used DCM with KNN – in what was called Nearest Floor Algorithm – for floor identification only (achieving 86% accuracy), so the corresponding 2-D positioning accuracy is not available.

In [43] the authors used DCM with distinct similarity functions (Euclidean, Manhattan, and Tanimoto distances) and a sequence of filtering steps and majority rules, to progressively identify the building, the floor, the room, and then the geometric position of the target MS within the room. As in [23], there are two stages in the position fix: first, a symbolic location is determined (the room where the target MS is located); then, a physical location (within the room) is determined. The CDB filtering was based on the strongest AP (i.e., the one with the highest RSS) detected by the target MS: only the Rfings with the same strongest AP as the one reported by the target MS were included in the CDB. To account for the RSS variability, if the difference between the strongest and the second strongest APs reported in the Tfing were smaller than a given threshold, all Rfings where either AP was the best server [10] were added to the search space. A 99.5% floor identification accuracy was reported in a test bed comprising 2 buildings and 3 floors per building.

In [44], the authors defined a floor discriminative model using Fisher's Linear Discriminant (FLD) [60]. FLD can not only reduce input features dimensionality, but also act as a classifier in the reduced feature space. Within the selected floor, they applied DCM to find the Rfing most similar to the Tfing. For the fingerprints correlation, they used the Euclidean distance in the RSS space, with different weights for each dimension. For the final location estimate, KNN was used. The CDB was built using the Rfings collected in a six-floor building at 815 locations with a 1.6-meter separation between adjacent points. During the test phase, 600 measurement positions were randomly selected. The authors reported a 94.3% floor identification accuracy.

The location engine introduced in this chapter employs a two-stage search space reduction technique: unsupervised clustering (Kohonen Layer with conscience) and supervised classification (committees of feed-forward ANNs). The first stage allows for the Rfings to group freely (without the imposition of architectural constraints) in the RSS space. The second stage allows for floor identification. DCM provides the 2-D position estimate within the selected floor. In a testbed with 924 points distributed over 13 floors, floor identification and average 2-D positioning accuracy ranged from 91% and 3.5 meters (for a window length of 1) to 97% and 1.1 meters (for

[10] At any given position, the best server is the AP whose signal has the highest RSS.

a window length of 25). As expected, it is possible to improve accuracy increasing the window length, but this is done at the expense of a larger time to acquire a position fix.

Table 3.7: Some published results on multi-floor positioning (Part 1).

Reference	[11]	[39]	[41]	[42]
Positioning Technique	Multi-Lateration (RSS)	BGM	DCM + Multi-Lateration (RSS)	DCM with KNN (Nearest Floor Algorithm)
Search Space Reduction Technique	(n/a)	(n/a)	none	none
Number of floors	3	2	8	3
No. of calibration points	(n/a)	(n/a)	57	150
No. of collected RF fingerprints	(-)	600	3420	(-)
No. of test points	150	30	3	150
Window Length	(-)	20	(-)	6
Correct Floor Id.(%)	100%	(-)	100%	86%
Mean 2-D Positioning Accuracy (m)	7.5	2.3	1.6	(n/a)

One final word about the results shown in Tables 3.7 and 3.8: there is a high variability in the database sizes, which affects any comparative analysis. Even more critical is the presence of small number of floors in some experiments [11, 39, 42, 43], what may compromise conclusions on the floor identification accuracy.

3.7 Conclusions

This chapter has introduced a novel machine learning-based location engine for WiFi 2.5-D indoor positioning with controlled computational complexity. In most buildings, it is much easier to move around the same floor than it is to move between floors. Based on that, the main objective driving the development of the proposed location engine was maximizing the floor identification accuracy. With that purpose, it has a two-stage search space reduction technique: unsupervised clustering using a

Table 3.8: Some published results on multi-floor positioning (Part 2).

Reference	[43]	[44]	This work
Positioning Technique	DCM with Filtering and Majority Rules	DCM with KNN	DCM
Search Space Reduction Technique	Strongest AP	FLD	unsupervised clustering in the RSS space + MLP committees for floor id.
Number of floors	3	6	13
No. of calibration points	392 (distributed in 2 buildings)	815	924
No. of collected RF fingerprints	9358 (distributed in 2 buildings)	4075	46200
No. of test points	236/building $\times$ 2 buildings	600	924
Window Length	3	(-)	1, 5, 10, 25
Correct Floor Id.(%)	99.5%	94.3%	91%, 94%, 95%, 97%
Mean 2-D Positioning Accuracy (m)	3.3	1.2	3.5, 2.3, 1.8, 1.1

Kohonen layer with conscience, followed by supervised classification with committees of feed-forward ANNs.

The first technique, following a natural or RF approach for the multi-floor positioning, is based on an unsupervised clustering method. It applies natural data clustering, grouping the data vectors (formed by RSS levels) without considering building structural data. This tries to accommodate the similarities among data collected in the signal/natural (RSS) space. A single Kohonen Layer clusters the RF fingerprints in the CDB and reduces the search space. Conscience is also used in the Kohonen layer to improve the input space mapping, which results in higher positioning accuracy and lower computational complexity. This technique allows collected Rfings to group freely in their natural space, without preventing any natural arrangement of the collected fingerprints.

The second technique tries to accommodate architectonic aspects, i.e., floor identification (desired system output). In this context, majority voting committees of feed-forward ANNs are employed for identifying the floor on which the MS is located. Only the committees of the floors spanned by the cluster identified by the unsupervised classifier are activated. Therefore, the concatenation of the Kohonen layer and the committees of feed-forward ANNs results in a reduced search space,

comprising only the Rfings within the cluster selected by the Kohonen layer and the floor indicated by the activated ANNs committees.

Prior to forwarding the data to the classifiers, PCA pre-conditioning is used to produce input vectors with uncorrelated components. Then, 43% of the PCs were discarded, and the remaining set comprised 99% of the input data variance. PCA is therefore employed as a compression technique so that the classifiers can process vectors with fewer components. The PCs are computed considering all Rfings and its decomposition is not applied differently in each cluster, being the same for any Tfing fed to the localization engine. Therefore, the PCs do not change with the number of clusters, being a characteristic of the building and the APs localization within the building.

The proposed location engine is assessed with actual data. Particular care has been taken regarding data collection, obtaining a high number of samples so that the experimental results could be more reliable and representative of the type of environment under analysis. The proposed location engine shows a good performance with actual data gathered in a multi-storey building, achieving a floor identification accuracy ranging from 91% to 97%, and an average 2-D positioning error between 3.5 to 1.1 meters.

Chapter 4

Evaluation of RF Through-The-Wall Mapping Reconstruction Methods

This chapter explores RF-based through-the-wall mapping (TWM), a technique to map stationary obstacles without sensing them directly. It can obtain a floor map before entering a building. Therefore, as through-the-wall radar imaging (TWRI), TWM aims at improving situational awareness in critical conditions in indoor environments [4]. However, unlike TWRI, there are very few papers addressing TWM applications [5–8]. This chapter reviews the fundamentals of the reconstruction techniques than can be applied to TWM problems, all of them originally used in computerized X-ray tomography. Then, a simulation model is set up, using path-loss equations corrupted by Rayleigh noise to account for multipath reception. This model is based on geometric optics postulates, thereby diffraction is not explicitly considered. Two test floor maps are defined, and a comparative analysis of the reconstruction methods is carried out. A metric for image quality assessment is tentatively selected to allow an objective comparison of the reconstructed images under different conditions.

4.1 Introduction

Indoor positioning techniques allow locating and tracking RF mobile devices, which can improve tactical situation awareness in critical conditions, such as search-and-rescue and military operations in urban areas [4]. Situation awareness in a tactical level is the perception of environmental variables, in time and space, and the ability to understand and interrelate them, as a basis for quick decision making in crisis intervention [61]. Situation awareness in critical conditions can be further improved

by techniques that enable:

- mapping a floor with mobile units using RF and other specialized sensors (infra-red, ultrasonic, laser) (SLAM – Simultaneous Localization and Mapping);
- locating unspecific moving targets behind walls using reflected RF signals (TWRI – Through-the-Wall Radar Imaging)
- obtaining the blueprint of a floor before entering it, using transmitted RF signals (TWM – Through-the-Wall Mapping)

TWRI and TWM are non-invasive techniques, as they perform their tasks from the outside of the building. On the other hand, SLAM is invasive, as the mobile unit gathering measurements must enter the floor and directly sense the obstacles being mapped.

4.1.1 Direct Sensing Techniques: SLAM

SLAM employs a mobile unit to build a map of an area, by measuring the distance between the device and selected landmarks (and other mobile units, in the case of cooperative SLAM [62]), while enabling the mobile unit to locate itself. Therefore, it must be equipped with range measuring devices, such as ultrasound, infrared, laser or RF [63]. Typically, the mobile unit uses odometry-based dead reckoning to estimate its relative location based on its displacements (translation and rotation). Within the SLAM context, the mobile unit is usually a mobile robot, but it might also be a smartphone [64]. The landmarks must be fixed and well distinguishable features in the area to be mapped, such as walls and corners. The selected landmarks must be sensed directly by the mobile unit.

4.1.2 Non-Invasive Sensing Techniques: TWRI and TWM

TWRI: this technique aims at locating moving targets behind walls using active radar principles, i.e., successive pulses are transmitted to illuminate the target, and their echoes are received and processed [65]. The ability to locate non-cooperative individuals inside a room, before entering it, is of paramount importance for law enforcement under certain critical scenarios, such as hostage situations. It might also be quite useful in search-and-rescue operations. There are several TWRI prototypes available, capable of detecting motion through non-metallic walls. Several implementations are handheld [66], though others employ large antenna arrays [67]. Most solutions operate in the Ultra-High Frequency (UHF) band.

TWM: its objective is to map static obstacles without sensing them directly. Therefore, it provides a non-invasive way to build a floor map. The capability to obtain an estimate of the floor blueprint, before entering it, might provide valuable information in military operations, such as urban combat and hostage situations. In such cases, direct obstacle mapping with specialized sensors on-board a mobile robot is not an option, for example, due to the presence of hostile forces inside the building. TWM can also be used in situations when the area to be mapped is not accessible due to physical constraints, such as in damaged buildings. TWM can be treated as a discrete inverse problem [68]. TWM floor map reconstruction employs algorithms originally applied to X-ray Computerized Tomographic Imaging (CTI) [5, 8, 69, 70].

4.1.3 Chapter Outline

Section 4.2.1 clarifies some TWM-related concepts, such as the parallel-beam geometry, the Radon Transform, and the Fourier Central Slice Theorem. Section 4.2.2 reviews the key aspects of the reconstruction methods traditionally used in X-Ray CTI for image reconstruction from parallel-beam projections. Section 4.3 explains the RF TWM simulation model and its parameters, as well as the tentative selection of an objective comparison metric for the evaluation of the reconstructed images quality. Section 4.4 analyzes the results of RF TWM simulations using the reconstruction methods described in Section 4.2.2. Finally, Section 4.5 draws a brief conclusion and points out some relevant issues to be explored in the remainder of this work.

4.2 RF-Based TWM Fundamentals

4.2.1 Parallel-Beam Projections

The first generation of X-ray CTI used the parallel-beam geometry [71]. This geometry was selected for the RF TWM simulations in this chapter because it is the simplest to reproduce in a real scenario. It requires just one transmitter and one receiver, which follow parallel paths and whose directive antennas must be aligned. The Radon transform and the Fourier Central Slice theorem provide the mathematical foundation for the reconstruction techniques used with this acquisition geometry [72]. To simplify the introduction of these principles, this section addresses only the continuous case, i.e., all spatial (referenced both in rectangular and polar coordinates) and frequency variables are assumed to be continuous. The practical discrete case is dealt with in Section 4.2.2.

Radon Transform

Consider line r in Fig. 4.1a, defined by $y = (\tan\gamma)\,x + b$, where $(0, b)$ are the coordinates of point B, which is the intersection between r and the y-axis. From triangle OCA, one gets that $\gamma = \theta_k + \pi/2$, so $\tan\gamma = -1/\tan\theta_k$. From triangle OCB, one verifies that $b = \rho_j/\sin\theta_k$. Therefore, $y = -x/\tan\theta_k + \rho_j/\sin\theta_k$, which can be rewritten as $x\cos\theta_k + y\sin\theta_k = \rho_j$. A parallel-beam can be defined by a set of such lines (rays), varying ρ for a fixed θ, as Fig. 4.1b depicts.

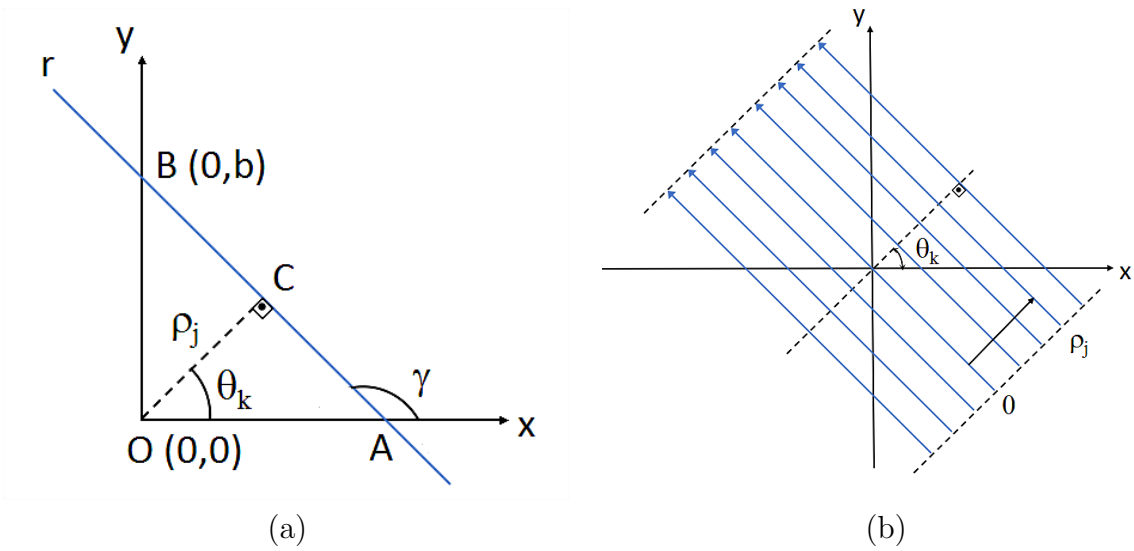

(a) (b)

Figure 4.1: (a) Defining the line equation using polar parameters; (b) Parallel-ray beam for $\theta = \theta_k$.

Assume that each ray in the parallel beam represents the propagation path of electromagnetic energy traveling between a transmitter-receiver pair, moving along L-meter parallel paths, as shown in Fig. 4.1b. If the ray passes through an object positioned along the propagation path, part of its energy is absorbed by the object. Then, a projection is obtained at the receiver end, where the absorption characteristics of that object are imprinted. Assuming that the output power is known, the absorption along the trajectory specified by θ_k and ρ_j can be inferred from the received energy. This absorption is given by the line integral

$$g(\rho_j, \theta_k) = \int_{-\infty}^{+\infty} \int_{-\infty}^{+\infty} f(x, y)\delta(x\cos\theta_k + y\sin\theta_k - \rho_j)dxdy \qquad (4.1)$$

where $f(x, y)$ is the absorption rate of the object cross-section at coordinates (x, y). The impulse function indicates that the integration is carried out along the line $x\cos\theta_k + y\sin\theta_k = \rho_j$.

Equation (4.1) is the Radon transform of function f in the xy-plane along the direction defined by θ_k and ρ_j [72]. Projection $g(\rho, \theta_k)$ is obtained applying equa-

tion (4.1) for all $\rho \in [-L/2; L/2]$. After calculating the projections for all $\theta \in [0; \pi)$, one obtains the *sinogram* of the original image.

Fourier Central Slice Theorem

The Fourier Central Slice theorem states that the one-dimensional (1-D) Fourier Transform (FT) of a Radon projection of an image taken at angle θ_k is equal to the slice of the two-dimensional (2-D) FT of that image, taken at that same angle. The 1-D FT of a Radon projection at angle θ_k with respect to spatial variable ρ is given by

$$G(\mathrm{f}, \theta_k) = \int_{-\infty}^{+\infty} g(\rho, \theta_k) e^{-j2\pi \mathrm{f}\rho} d\rho \tag{4.2}$$

where f is the spatial frequency. Replacing $g(\rho, \theta_k)$ in equation (4.2) by the expression provided by equation (4.1), and solving the innermost integral using the impulse sampling property, one gets

$$G(\mathrm{f}, \theta_k) = \int_{-\infty}^{+\infty} \int_{-\infty}^{+\infty} f(x, y) e^{-j2\pi(\mu x + \nu y)} dx dy \tag{4.3}$$

where $\mu = \mathrm{f}\cos\theta_k$ and $\nu = \mathrm{f}\sin\theta_k$, are the frequency variables. The right side of equation (4.3) is a central slice of the 2-D FT of $f(x, y)$, taken at angle θ_k.

4.2.2 Image Reconstruction from Parallel-Beam Projections

The Radon transform might be seen as a projection operator. Its value is given by a line integral through the object (represented by function $f(x, y)$) along the line specified by ρ and θ. A Radon projection is a set of line integrals, i.e., a set of values of the Radon transform, obtained varying ρ, while keeping θ fixed. The set of Radon projections, obtained varying θ, is the sinogram of the original image. The reverse process, i.e., recovering the original image from its sinogram, is called image reconstruction. This section addresses four reconstruction methods largely used in CTI [72]: Filtered Backprojection Reconstruction (FBR), Direct Fourier Reconstruction (DFR), Algebraic Reconstruction Technique (ART) and Simultaneous Iterative Reconstruction Technique (SIRT).

Filtered Backprojection Reconstruction (FBR)

Filtered Backprojection Reconstruction (FBR) is the most widely used technique in CTI [71]. By backprojection, one means that each Radon projection is smeared over the image along the parallel-beam direction, as Fig. 4.2 shows.

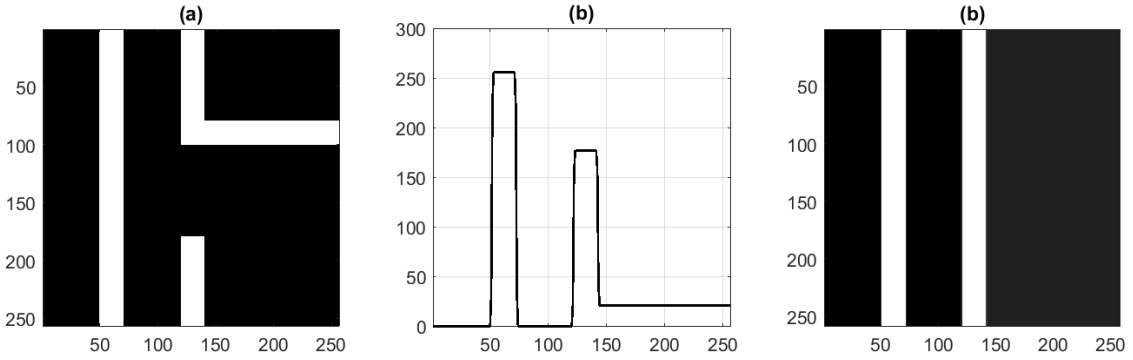

Figure 4.2: (a) Original 256×256-pixel image; (b) Radon projection at angle $\theta = 0$; (c) Backprojection of (b), i.e., laminar image of (a) at $\theta = 0$.

Function $f(x, y)$ expresses the absorption rate of the object cross-section at planar coordinates (x, y). $F(\mu, \nu)$ is the 2-D FT of $f(x, y)$, from which follows that $f(x, y)$ is the inverse 2-D FT of $F(\mu, \nu)$. In polar coordinates, it is given by

$$f(x,y) = \int_0^{2\pi} \int_0^{+\infty} F(\mathrm{f}\cos\theta, \mathrm{f}\sin\theta) e^{j2\pi \mathrm{f}(x\cos\theta + y\sin\theta)}\ \mathrm{f}\ d\mathrm{f}\ d\theta \tag{4.4}$$

From equation (4.3), one gets that $F(\mathrm{f}\cos\theta, \mathrm{f}\sin\theta) = G(\mathrm{f}, \theta)$, where $G(\mathrm{f}, \theta)$ is the FT of the Radon projection $g(\rho, \theta)$. Replacing that value in equation (4.4) and using some trigonometry yields

$$f(x,y) = \int_0^{\pi} \left(\int_{-\infty}^{+\infty} |\mathrm{f}|\ G(\mathrm{f}, \theta) e^{j2\pi \mathrm{f}\rho} d\mathrm{f} \right)\ d\theta \tag{4.5}$$

where the inner integral provides $\mathcal{F}_1^{-1}\{|\mathrm{f}|\, G(\mathrm{f}, \theta)\}$, i.e., the inverse 1-D FT of $G(\mathrm{f}, \theta)$ multiplied by a ramp. Equation (4.5) states that the original image $f(x, y)$ can be reconstructed by backprojecting $\mathcal{F}_1^{-1}\{|\mathrm{f}|\, G(\mathrm{f}, \theta)\}$. In the practical discrete case, equation (4.5) becomes an approximation given by

$$\hat{f}(x,y) = \Delta\theta \sum_{\theta=0}^{n} \mathcal{F}_1^{-1}\{|\mathrm{f}|\, G(\mathrm{f}, \theta)\} \tag{4.6}$$

where $\mathcal{F}_1^{-1}$ indicates the inverse 1-D Discrete FT (DFT) operator. The ramp reinforces the high-frequency components, compensating for the sparser sampling at high frequencies. This reduces blurring in the reconstructed image. To prevent ringing, the ramp filter transfer function is multiplied by a Hamming window [71]. As Fig. 4.3 shows, the Radon projection at angle θ_k is sampled at m points (dark dots in the image). As a result, the value $g(\rho, \theta_k)$ to be backprojected over the pix-

els (of the reconstructed image) along the line defined by (ρ, θ_k) must be obtained by interpolation.

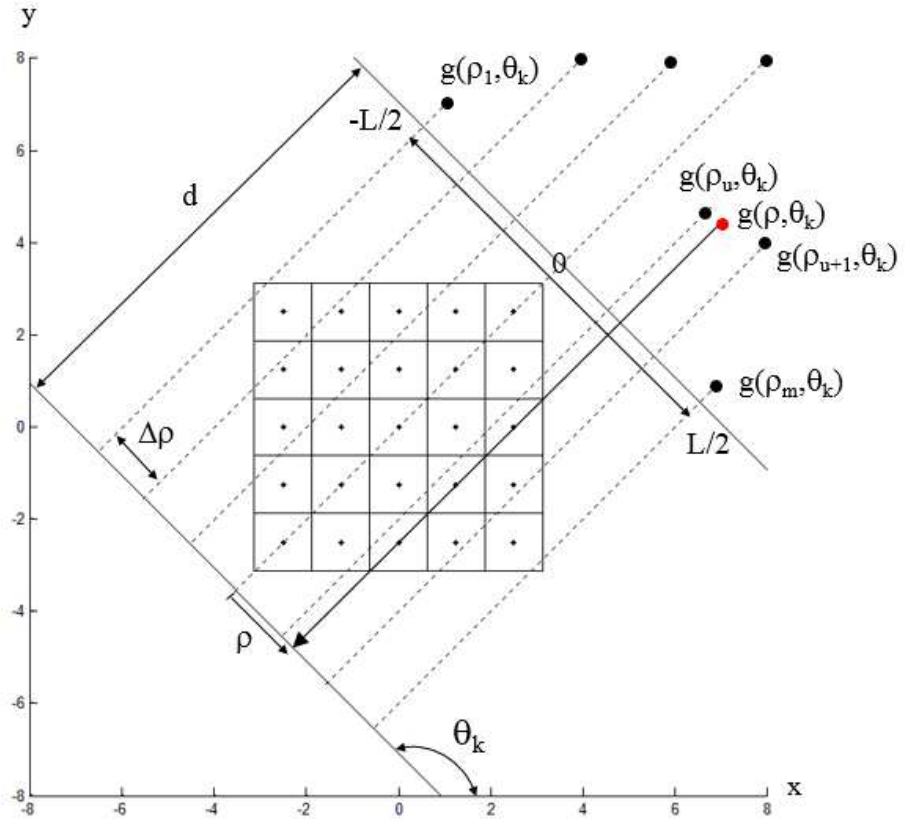

Figure 4.3: Backprojection and one-dimensional interpolation.

Direct Fourier Reconstruction (DFR)

The Fourier Central Slice theorem is the basis for DFR. That theorem states that the 1-D FT of a Radon projection at angle θ_k is equal to a slice of the 2-D FT of the original image (represented by function $f(x, y)$) at that same angle. So, by taking projections for $0 \leq \theta < \pi$, and calculating their FTs, one obtains the 2-D FT of $f(x, y)$. By calculating its inverse, one recovers the original image. The process of DFR can the be summarized by

$$f(x, y) = \mathcal{F}_2^{-1} \cdot \mathcal{F}_1 \cdot \mathbf{G} \tag{4.7}$$

where $\mathcal{F}_n$ and $\mathcal{F}_n^{-1}$ are the n-dimensional DFT and inverse DFT operators, respectively [73]; and

$$\mathbf{G} = [g(\rho_j, \theta_k)]_{j=1,\ldots,m;k=1,\ldots,n} \tag{4.8}$$

is the sinogram matrix, i.e., the set of Radon transforms obtained passing parallel beams through the object.

However, in the practical discrete case, only a finite number of slices are taken, with a limited number of samples along each slice. As Fig. 4.4 indicates, those samples are measured over a polar grid, at coordinates given by (ρ, θ) (blue dots). To calculate the inverse 2-D DFT (Discrete Fourier Transform), those samples must be interpolated to a rectangular grid (black dots). So, the formulation summarized by equation (4.7) becomes an approximation, given by

$$\hat{f}(x, y) = \mathcal{F}_2^{-1} \cdot \mathcal{I}_{\rho\theta}^{xy} \cdot \mathcal{F}_1 \cdot \mathbf{G} \tag{4.9}$$

where $\mathcal{I}_{\rho\theta}^{xy}$ is the interpolation operator, that fills the rectangular grid with the interpolated values of the samples in the polar grid, as shown in Fig. 4.4.

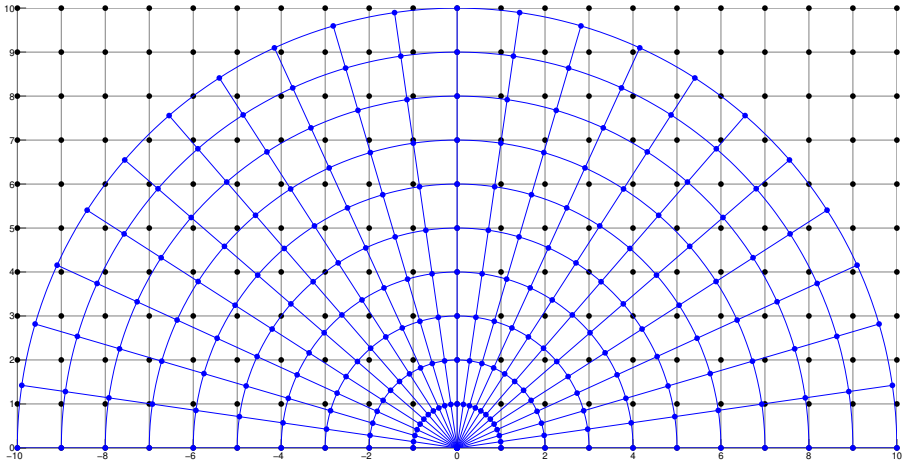

Figure 4.4: 2-D rectangular interpolation grid in the frequency plane.

Iterative Algebraic Reconstruction Methods (ART and SIRT)

In algebraic reconstruction, one treats the floor map $f(x, y)$ as a matrix of $N \times N$ unknowns. This discrete inverse problem is represented by the linear system

$$\mathbf{A}\hat{\mathbf{x}} = \mathbf{b} \tag{4.10}$$

where $\hat{\mathbf{x}} = [\mathrm{x}_i]_{i=1,\ldots,N^2}$ is the column vector with the elements of $\hat{f}(x, y)$, i.e., the reconstructed image; $\mathbf{b} = [\mathrm{b}_i]_{i=1,\ldots,mn}$ is the column vector with the elements of the sinogram $\mathbf{G}$; and $\mathbf{A} = [\mathrm{a}_{i,j}]_{i=1,\ldots,mn;j=1,\ldots,N^2}$ is the coefficient matrix. Each line of matrix $\mathbf{A}$ corresponds to a ray in the parallel-beam acquisition geometry. As Fig. 4.5 shows, element $\mathrm{a}_{i,j}$ informs the length of the path traversed by the ith ray across

the jth pixel. Thereby, one has

$$\mathrm{b}_i = g(\rho_u, \theta_v) = \sum_{j=1}^{N^2} \mathrm{a}_{i,j}\hat{\mathrm{x}}_j \tag{4.11}$$

where $g(\rho_u, \theta_v)$ is the Radon transform along the ray defined by (ρ_u, θ_v), $u = 1, \ldots, m$, $v = 1, \ldots, n$ and $i = 1, \ldots, mn$.

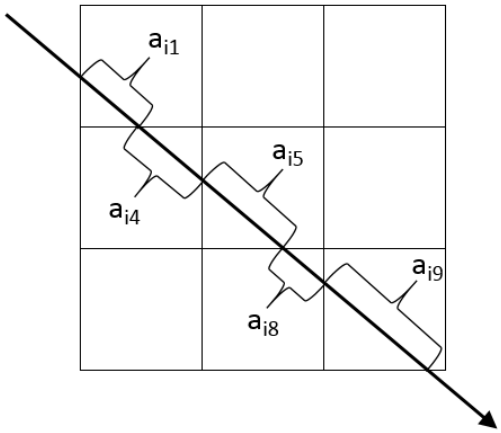

Figure 4.5: Example of a 3×3 coefficient matrix.

In typical TWM reconstruction problems matrix $\mathbf{A}$ is huge. For example, assuming a discretized floor map with 256×256 pixels and a parallel-beam acquisition geometry with 256×80 rays, $\mathbf{A}$ is a 20480×65536 matrix. Furthermore, equation (4.10) represents a discrete ill-posed problem, as matrix $\mathbf{A}$ condition number is very large [68, 74]. In such cases, regularization is needed, to prevent the noise in $\mathbf{b}$ from causing significant fluctuations in the solution.

Just a small fraction of the elements of $\mathbf{A}$ are not zero, as each ray passes through just a small percentage of all pixels composing the floor blueprint. From Fig. 4.5 one sees that any ray crosses at most $2N - 1$ pixels. For $N = 256$, no ray traverses more than 511 pixels. In that case, no more than 0.78% of the elements of any line of $\mathbf{A}$ would be non-null.

Considering $\mathbf{A}$'s sparsity and the need to obtain a solution less affected by the noise in the input data, iterative regularization methods for linear ill-posed problems become a preferable alternative for reconstruction [74]. This section addresses two such methods: Kaczmarz's (ART) and Landweber's (SIRT).

Algebraic Reconstruction Technique (ART): The Kaczmarz's iterative regularization algorithm, also known as ART, has been widely applied in tomographic reconstruction [72]. It is a simple method which usually converges in just a few

iterations [68]. This subsection addresses its fundamentals.

Consider the linear system in equation (4.10). Each line of this system defines a hyperplane in the N^2-dimensional space, i.e.,

$$\mathcal{H}_i = \{\mathbf{x} | \mathbf{a}_i \mathbf{x} = \mathrm{b}_i\} \tag{4.12}$$

where $\mathbf{a}_i$ is the ith line of $\mathbf{A}$. Each solution is projected on the subsequent hyperplane, i.e., $\hat{\mathbf{x}}_K^{(i-1)}$ is projected on $\mathcal{H}_i$ producing $\hat{\mathbf{x}}_K^{(i)}$ for $i = 1, \ldots, mn$. This sweep is repeated at each iteration K of the algorithm. The cycle continues until a stop criterion has been met, which might be a maximum number of iterations or some convergence indicator. This iterative process can be described by

$$\hat{\mathbf{x}}_K^{(i)} = \hat{\mathbf{x}}_K^{(i-1)} + \beta \mathbf{a}_i^{\mathrm{T}} \tag{4.13}$$

where β is a scalar and $\mathbf{a}_i^{\mathrm{T}}$ is orthogonal to the ith hyperplane. Combining equations (4.13) and (4.12) and isolating β, one obtains

$$\beta = \frac{\mathrm{b}_i - \mathbf{a}_i \hat{\mathbf{x}}_K^{(i-1)}}{\|\mathbf{a}_i\|_2^2} \tag{4.14}$$

where the denominator provides the squared l_2 norm of $\mathbf{a}_i$.

At the expense of a slower convergence, the effects of noise in the ART reconstructed image can be further mitigated by using a relaxation parameter $\delta \in (0, 1]$. Replacing the value of β provided by equation (4.14) into equation (4.13) and adding a relaxation parameter, one gets the definition of Kaczmarz's iterative process, given by

$$\hat{\mathbf{x}}_K^{(i)} = \hat{\mathbf{x}}_K^{(i-1)} + \delta \mathbf{a}_i^{\mathrm{T}} \left(\frac{\mathrm{b}_i - \mathbf{a}_i \hat{\mathbf{x}}_K^{(i-1)}}{\|\mathbf{a}_i\|_2^2} \right), \; i = 1, \ldots, mn \tag{4.15}$$

$$\hat{\mathbf{x}}_{K+1}^{(0)} = \hat{\mathbf{x}}_K^{(mn)}, \; K = 1, 2, 3, \ldots \tag{4.16}$$

The relaxation parameter can be static or decreasing, to reduce the oscillations around the optimal solution in the final iterations. The latter is analogous to the use of decreasing learning steps per neuron during the training of a Kohonen layer, as seen in Chapter 3.

Simultaneous Iterative Reconstruction technique (SIRT): Landweber's iterative algorithm, also known as SIRT, carries out successive approximations of $\mathbf{x}$ through

$$\hat{\mathbf{x}}_K = \hat{\mathbf{x}}_{K-1} + \delta \mathbf{A}^{\mathrm{T}} \left(\frac{\mathbf{b} - \mathbf{A} \hat{\mathbf{x}}_{K-1}}{\left\| \mathbf{A} \mathbf{A}^{\mathrm{T}} \right\|_2^2} \right) \tag{4.17}$$

where δ is the relaxation parameter. Note the similarity with equation (4.15). However, while in ART the solution was updated for every line of the linear system defined by equation (4.10), in SIRT the update is not carried out in such line-wise manner. Instead, one uses all lines of $\mathbf{A}$ simultaneously, i.e., at each iteration [75]. This results in SIRT yielding a more stable solution than ART, which leads to better-quality reconstructed images. However, this is achieved at the expense of slower convergence [72, 74]

4.3 Problem Model

In the absence of data from field measurements, one has to resort to computer simulations to evaluate reconstruction algorithms applied to RF TWM. These simulations typically rely on empirical path loss equations (offset-slope models). Calibration campaigns are required to fine tune such models before applying them to a specific environment. These propagation models apply the geometric optics approximation, i.e., they disregard common wave propagation phenomena such as diffraction. Furthermore, they also do not take into account ray bending due to refraction and multipath reception caused by multiple reflections. In other words, these models assume single-path straight-line propagation. In an attempt to take the effect of multipath into consideration, Rician or Rayleigh distributions are commonly used to provide an additional random path loss component [70, 76]. For the simulations, floor blueprints are provided, so that the reconstruction techniques can be evaluated. These maps can be built as "occupancy grids" [77], i.e., as $N \times N$ matrices of 1's and 0's. Each matrix element corresponds to a pixel, and non-null elements indicate the presence of an obstacle (e.g., a wall or a column). Alternatively, each non-null element might inform the attenuation that the obstacle at that location imposes to the RF signal (at a given frequency) passing through it [69].

4.3.1 Propagation Modeling

Referring to the parallel-beam geometry depicted in Fig. 4.1, one has the following equation describing the mean received power P_r (dBm) at d meters from the transmitter along the line defined by (ρ_j, θ_k), $j = 1, \ldots, m$ and $k = 1, \ldots, n$:

$$P_r(\rho_j, \theta_k) = P_t - L_t + G_t - L_d - \sum_i \alpha_i(\rho_j, \theta_k) l_i(\rho_j, \theta_k) + G_r - L_r \tag{4.18}$$

where $l_i(\rho_j, \theta_k)$ and $\alpha_i(\rho_j, \theta_k)$ are the length (meters) and the attenuation factor (dB/m) across the ith obstacle, respectively. P_t (dBm) is the mean transmitted power. L_t and L_r are the losses (dB) due to cables and connections at the trans-

mitter and receiver, correspondingly. G_t and G_r are the transmitter and receiver antennas gains (dBi), in that order. L_d is the propagation loss (dB) as a function of the transmitter-receiver distance (d).

Equation (4.18) represents the path loss assuming single-path straight line propagation. In such a scenario, it is clear that

$$\sum_i \alpha_i(\rho_j, \theta_k) l_i(\rho_j, \theta_k) = g(\rho_j, \theta_k) \tag{4.19}$$

i.e., the summation of the losses across the obstacles along the line defined by (ρ_j, θ_k) is equal to the Radon transform of the floor blueprint $f(x, y)$ along that same line. This comes from the very definition of the Radon transform. Thereby, equation (4.18) can be rewritten as

$$g(\rho_j, \theta_k) = P_t - P_r(\rho_j, \theta_k) - L_t - L_r - L_d + G_t + G_r \tag{4.20}$$

Therefore, by measuring $P_r(\rho_j, \theta_k)$ for $j = 1, \ldots, m$, one obtains the Radon projection $g(\rho, \theta_k)$ of $f(x, y)$ at angle θ_k.

The value of L_d (dB) can be approximated by an empirical model, such as the one defined by

$$L_d = \beta_{\text{offset}} + \beta_{\text{slope}} \log\left(\frac{d}{d_0}\right) \tag{4.21}$$

where β_{offset} is the propagation loss (dB) at a distance d_0 meters from the transmitter, and β_{slope} is the path loss exponent or slope (dB/decade). Calibration campaigns are required to fine tune such models before they can be applied to a specific environment. During these campaigns, at each selected measurement point, the distance d and the mean propagation loss at that location are registered. Then, linear regression can be used to estimate β_{offset} and β_{slope} [78]. From Fig. 4.3, it is clear that along a d-meter path, the ray passes through two environments: outside and inside the floor being mapped. If d is the transmitter-receiver distance, $d_{\text{in}}(\rho_j, \theta_k)$ is the distance traversed inside the floor by the ray defined by (ρ_j, θ_k), and assuming $d_0 = 1$ meter, equation (4.21) becomes

$$L_d\left(\rho_j, \theta_k\right) = \beta_{\text{offset}} + \beta_{\text{slope,out}} \log\left(\frac{d}{d_{\text{in}}(\rho_j, \theta_k)}\right) + \beta_{\text{slope,in}} \log\left(d_{\text{in}}(\rho_j, \theta_k)\right) \tag{4.22}$$

where $\beta_{\text{slope,in}}$ and $\beta_{\text{slope,out}}$ are the slope inside and outside the floor, respectively.

4.3.2 Maximum Supportable Over-the-Air Path Loss

The maximum supportable over-the-air path loss (dB) is given by

$$L_{\max} = \text{EIRP} + G_r - L_r - S_0 \tag{4.23}$$

where S_0 is the receiver sensitivity (dBm); the Effective Isotropic Radiated Power (EIRP) in dBm is defined by

$$\text{EIRP} = P_t - L_t + G_t \tag{4.24}$$

Using equations (4.23) and (4.24) to replace the proper terms in equation (4.20), one gets

$$g(\rho_j, \theta_k) = L_{\max} + S_0 - P_r(\rho_j, \theta_k) - L_d(\rho_j, \theta_k) \tag{4.25}$$

Any received signal below S_0 is reported as equal to S_0, i.e., $P_r(\rho_j, \theta_k) \geq S_0$. As a result, the maximum detectable shadowing loss along the path defined by (ρ_j, θ_k) is

$$g_{\max}(\rho_j, \theta_k) = L_{\max} - L_d(\rho_j, \theta_k) \tag{4.26}$$

Thereby, during the acquisition of the RF samples, the Radon projection is effectively "clipped" at $g_{\max}(\rho_j, \theta_k)$, as shown in Fig. 4.6 [1]. This means that information about the obstacles along the propagation path is lost, which will result in additional reconstruction error. From equation (4.26), it is clear that, the higher the $L_{\max}$, the higher the amount of detail that can be acquired about the obstacles being mapped.

4.3.3 Static Multipath Propagation

The parallel-beam geometry described in Section 4.2.2 assumes single-path straight-line propagation. While for X-Ray tomography this simplification poses no problem, due to the nanometric radiation wavelength, in RF-based TWM it results in reconstruction error [76].

In the acquisition phase, the transmitter-receiver pair is static during the measurements at each position. The intervening obstacles are also not moving in relation to the transmitter-receiver pair. Therefore, multiple reflections at the walls and diffraction result in static multipath fading [2]. Such condition is deterministic, and

[1] For simplicity, $L_{\max}$ is assumed to be equal for all ρ_j, $j = 1 \ldots, m$.

[2] In a mobile link, the received signal amplitude undergoes rapid fluctuations due to dynamic multipath reception. In the absence of a direct LOS path, the received signal envelope in such circumstances is approximately Rayleigh distributed. Besides the reception of multipath components with random amplitude and phases, there might also occur a Doppler shift, due to the relative movement between transmitter and receiver. If both transmitter and receiver are stationary, there is no Doppler effect and the multipath is said to be static.

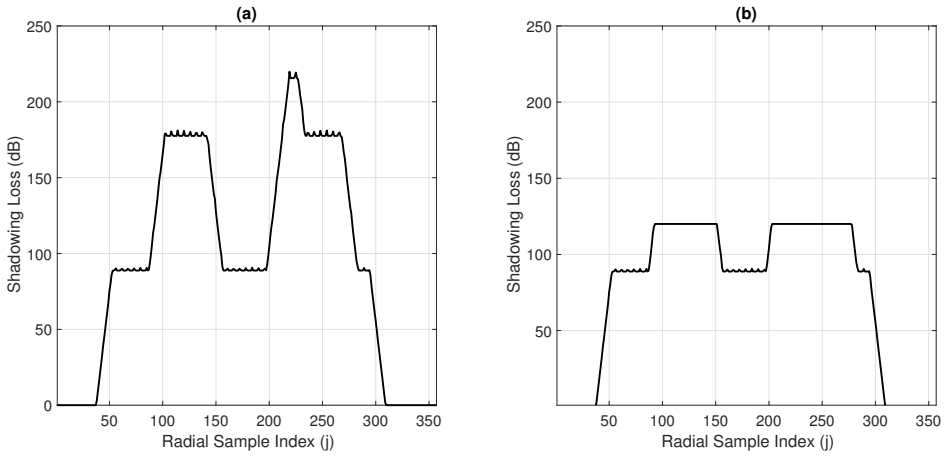

Figure 4.6: (a) Radon projection of Fig. 4.2a for $\theta = 45$ degrees; (b) "Clipping" effect due to $L_{\max}$ limitation ($S_0 = -120$ dBm).

given enough information about the environment – which is not available when one intends to map a floor – it would be possible to estimate the several propagation paths using ray-tracing techniques and the resulting received level [3]. Static multipath reception alters the shadowing loss estimates, which has a direct effect on the reconstruction error. The effect of multipath in stationary links can be modeled by a Rayleigh distribution. The random values selected from this distribution provide the additional propagation loss, to be added to the previously calculated average propagation loss (path loss plus shadowing). As no ray-tracing techniques are used, one might assume that the multipath components (amplitude and phase) are random, but that their average is time-invariant, for any given transmitter-receiver path through the target floor [76]. Equation (4.19) then becomes:

$$g(\rho_j, \theta_k) = \sum_i \alpha_i(\rho_j, \theta_k) l_i(\rho_j, \theta_k) + \Delta_b \tag{4.27}$$

where Δ_b(dB) is the multipath fading relative to the mean received power, given by:

$$\Delta_b = 20 \log_{10} \left(\frac{R_b}{2b} \right) \tag{4.28}$$

[3]Fluctuations in the amplitude of the received multipath components will still occur, due to punctual variations of the air refractive index (due to atmospheric conditions and local temperature) or modifications in the intervening obstacles (such as doors being opened or closed, furniture being moved on the floor, and people walking around). However, the link is more stable (static in time).

R_b is the Rayleigh probability distribution function with parameter b, defined by

$$R_b = \frac{x}{b^2} e^{\left(\frac{-x^2}{2b^2}\right)} \tag{4.29}$$

where x is the received signal amplitude, and b is equal to half the average received signal amplitude, i.e:

$$b = \frac{1}{2}\sqrt{10^{[0.1(P_t - L_t + G_t - L_d + G_r - L_r)]}} \tag{4.30}$$

Equation (4.27) indicates that the Radon projection along the direction defined by ρ_j and θ_k is equal to the shadowing loss through the obstacles along that direction plus the random term accounting for multipath reception (relative to the average received level). However, in the practical case, it is not possible to separate between the path loss and shadowing loss. Therefore, the Radon projection accounts for the total loss along the propagation path. So, the sinogram matrix forwarded to the reconstruction methods is defined by

$$\mathbf{G} = [\text{EIRP} - G_r + L_r - P_r(\rho_j, \theta_k)]_{j=1,\ldots,m;k=1,\ldots,n} \tag{4.31}$$

where m is the number of samples per Radon projection and n is the number of projections.

4.3.4 Floor Maps

Fig. 4.7 shows the two maps used in the RF TWM simulations. These maps represent 9.2×9.2 m^2 areas. At the center of each area there is an 8×8 m^2 room. The first map has a central 1.6×1.6 m^2 concrete column. The second map has inner walls, dividing the main room in two rooms connected by a door. All walls are assumed to be 50-cm thick and made of concrete without steel reinforcement rods. The floor maps are stored as 128×128 matrices, so each pixel corresponds to $9.2/128 \approx 7.2$ cm on the field. Non-zero elements indicate the presence of an obstacle.

4.3.5 Sinogram Acquisition

To acquire the sinogram using a parallel-beam geometry, the transmitter and receiver pair moves along L-meter long lines. The receiver measures the mean received power with a $\Delta\rho$ spacing between subsequent samples. Therefore, the length of each Radon projection [4] is

$$L = (m-1)\Delta\rho \tag{4.32}$$

[4] In a parallel-beam acquisition geometry, all projections have the same length.

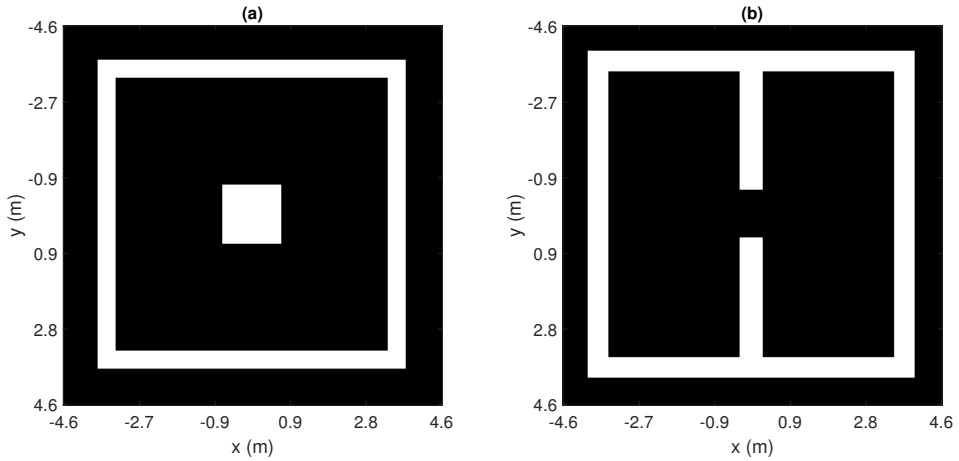

Figure 4.7: Floor maps used in the simulations.

where m is the number of samples per projection. Notably, for any given θ, L must be long enough to cover the whole area being mapped. The transmitter-receiver distance is also equal to L meters.

The samples collected along a line provide a discrete Radon projection [5]. Radon projections were obtained at n angles uniformly spaced in $[0,\pi)$, i.e., $\Delta\theta = \lfloor 180/n \rfloor$ degrees. Consequently, the full sinogram has $m \times n$ samples. To simulate lower sampling rates, proper subsets of the sinogram are selected.

The reconstructed images' sizes are $m \times m$ pixels [6], and they represent areas larger than the original floor maps. For example, to obtain a Radon projection of an 9.2×9.2 m^2 area at $\theta = 45$ degrees, $L \geq 9.2\sqrt{2} \approx 13$ meters. Therefore, the reconstructed images represent a 13×13 m^2 area. To compensate that and remove the excess length, the resulting images are cropped, such that their final size is $2\left(\left\lfloor \frac{m}{2\sqrt{2}} \right\rfloor \times \left\lfloor \frac{m}{2\sqrt{2}} \right\rfloor\right)$ pixels. In all simulations in this chapter, $L = 13$ meters.

4.3.6 Operational Frequency Selection

The main issues concerning the operational frequency selection for RF-based TWM are specific attenuation, diffraction, and interference from external sources. The first two are interchangeable: the higher the frequency, the higher the specific attenuation, but the lower the energy of the diffracted components; in the opposite direction, lower frequencies, though experiencing less through-the-wall attenuation,

[5] For simplicity, in all cases we refer to the set of samples collected along a line for a fixed θ as a Radon projection. However, these samples are treated as such only in the projective methods (FBR and DFR). In algebraic methods (ART and SIRT), each sample is treated independently (each providing an independent term of a line of the sparse matrix A).

[6] This applies only to the projective methods. However, for uniformity and to facilitate posterior image quality comparison, the final size (after cropping) as a function of m is also used in the algebraic methods.

are more prone to diffraction effects. A trade-off between those two issues must be set for a proper operational frequency to be selected. Table 4.1 lists the RF propagation parameters of interest at 500, 1000 and 2000 MHz [7]:

- the offset, i.e., the loss at $d_0 = 1$ meter from the transmitting antenna [79];
- the path loss exponent (attenuation slope) inside a typical office building [79];
- the attenuation factor (specific attenuation) through concrete [80];

Table 4.1: RF parameters (offset, in-building path loss exponent and through-the-wall attenuation factor) at 500, 1000 and 2000 MHz.

Frequency (MHz)	Offset (dB)	$\beta_{\text{slope,in}}$ (dB/decade)	Specific Attenuation through Concrete (dB/m)
500	26	36	36.0
1000	32	33	46.1
2000	38	30	57.5

The path loss exponent outside the building ($\beta_{\text{slope,out}}$) was assumed to be 20 dB/decade [81]. This corresponds to free space propagation, a reasonable approximation if the reflected component on the ground can be disregarded. Table 4.1 indicates that the through-wall attenuation is more than 10 dB lower at 1 GHz than at 2 GHz. Furthermore, frequencies around 2 GHz are to be avoided due to the external interference posed by the WiFi, 3G and 4G cellular networks. At 500 MHz, though the through-the-wall attenuation per meter is 10 dB lower than at 1 GHz, the 60-cm wavelength is too long. This would result in diffracted components with more energy. Pondering these issues, frequencies around 1 GHz were selected for the simulations.

4.3.7 Selecting an Objective Comparison Metric

To evaluate the reconstruction techniques, the original and the reconstructed floor maps are compared for different systemic parameters configuration sets. By systemic parameters, one refers to the operational parameters of the acquisition system, such as antenna gains (both transmitter and receiver antennas), sampling rates and operational frequency.

As a mean opinion score (MOS) campaign could not be carried out (and also considering computer vision applications that might use those reconstructed maps for robot navigation), an objective comparison metric is desirable. Preferably, the

[7] The RF propagation parameters at 500 MHz have been obtained by interpolation of the values at the nearest available frequencies, as there were no results available at this frequency in the selected references.

selected metric should **(i)** not be very sensitive to noise in the reconstructed image; **(ii)** compare the similarity of the objects' shape in the image, and not only pixel misclassification rate [8]; and **(iii)** follow as closely as possible the subjective evaluation of the reconstruction quality.

Metrics that just measure the pixel misclassification rate, such as mean-squared error or sum of absolute distances, would report a high distance between two images if one or more boundaries in one of them are just slightly shifted. This would happen even if such shifting preserved the shape of the objects in the image. To avoid that, Mean Structural Similarity Index (MSSIM) [82] was tentatively selected. The MSSIM is the average of the Structural Similarity Index (SSIM) values, which are calculated within a sliding window that is shifted pixel by pixel throughout the whole image. The SSIM is based on the assumption that human visual perception is specialized for the extraction of structural information from an image. The SSIM is given by

$$\mathrm{SSIM}_i\left(f_i, \hat{f}_i\right) = \left[l\left(f_i, \hat{f}_i\right)\right]^{(1/a_1)} \left[c\left(f_i, \hat{f}_i\right)\right]^{(1/a_2)} \left[s\left(f_i, \hat{f}_i\right)\right]^{(1/a_3)} \tag{4.33}$$

where f_i and $\hat{f}_i$ are the contents of the original and reconstructed image at the ith local window; functions l, c and s are defined in [82] and account for the luminance, contrast and structural similarities, respectively. Their outputs lie within $[0, 1]$. Positive parameters a_1, a_2 and a_3 adjust the relative weights of the three components. The MSSIM index is then provided by

$$\mathrm{MSSIM}\left(f_i, \hat{f}_i\right) = \frac{1}{M}\sum_{i=1}^{\mathrm{M}} \mathrm{SSIM}_i\left(f_i, \hat{f}_i\right) \tag{4.34}$$

where M is the number of local windows in the image. To calculate the SSIM, both $f(x, y)$ (the original image) and $\hat{f}(x, y)$ (the reconstructed image) must have the same dimensions, and their luminance values must be normalized to the same range. The MSSIM was calculated using $\frac{2}{3}\left(\left\lfloor\frac{m}{2\sqrt{2}}\right\rfloor \times \left\lfloor\frac{m}{2\sqrt{2}}\right\rfloor\right)$ local windows [9], with parameters $a_1 = 1$, $a_2 = 2$ and $a_3 = 4$.

[8] Pixel misclassification refers to differences between the original and reconstructed images pixel-by-pixel luminance, which is evaluated using metrics such as normalized mean-squared error.

[9] The size of the sliding window was empirically defined, adjusting it until the MSSIM reflected the subjective perception of image similarity. The key idea was that a window too small might lead to a poor MSSIM due to the Rayleigh noise in the image background. On the other hand, a sliding window which is too large might not allow the MSSIM to accurately evaluate similarities in different regions of the image.

4.4 Simulation Results

For all simulations, $G_t = G_r = 14$ dBi (isotropic gain of transmitter and receiver antennas), $L_t = L_r = 3$ dB (cable and connector losses at the transmitter and at the receiver) and $P_t = 40$ dBm (transmitter output power). In subsection 4.4.3, the receiver sensitivity (S_0) varies to allow evaluation of projection clipping in the reconstruction. In all other subsections, $S_0 = -110$ dBm. Furthermore, $L = 13$ meters and $m = 256$ samples per projection. Rearranging the terms in equation (4.32), one gets an inter-sample distance $\Delta\rho = L/(m-1) = 5$ cm. The histograms of all reconstructed images have been equalized for contrast enhancement and better visualization. FBR and DFR employed linear interpolation. At high sampling rates ($m = 256$ samples/per projection, or $\Delta\rho = 5$ cm), no perceptible improvement on reconstruction quality has been observed when using other interpolation schemes, such as spline interpolation or shape-preserving piecewise cubic interpolation [83].

4.4.1 ART and SIRT Convergence

Fig. 4.8 shows the convergence of algebraic methods ART and SIRT [10] with $n = 80$ projections when applied to the reconstruction of the floor maps depicted in Fig. 4.7. A vector with all elements set to zero has been arbitrarily chosen as the initial solution of both iterative methods. The convergence is expressed as a function of the similarity between the original and reconstructed images, calculated using the MSSIM. The behavior presented by both ART and SIRT is typical of regularization methods which show *semi-convergence* [68]: the initial iterates are progressively more regularized (filtered), and, as the number of iterations increases, it diverges from the optimal solution.

Notably, ART reaches the optimal solution in the very first iteration. This behavior can be promptly explained by the geometric interpretation of Kaczmarz's method, as Fig. 4.9 shows. The greater the angle between the hyperplanes (in this 2-D example, they are represented by lines) defined by adjacent lines of $\mathbf{A}$, the faster the algorithm converges to the optimal solution. In Fig. 4.9a, the angle is 78.6 degrees, and the algorithm converges in just 4 iterations. In Fig. 4.9b, the angle is 26.5 degrees, and the algorithm takes more than 15 iterations to reach the optimal solution. If the hyperplanes defined by adjacent lines of $\mathbf{A}$ are nearly orthogonal, then the algorithm might converge in just one iteration [74]. In the reconstruction problem analyzed in this section, due to $\mathbf{A}$'s sparsity (only 0.49% of non-null elements), this condition is observed: the box plot in Fig. 4.10 indicates that, except for a few outliers (displayed as red crosses), the angles lie in the interval $[84.9, 90]$ degrees.

[10] The ART and SIRT used the AIR Tools MATLAB® package [75].

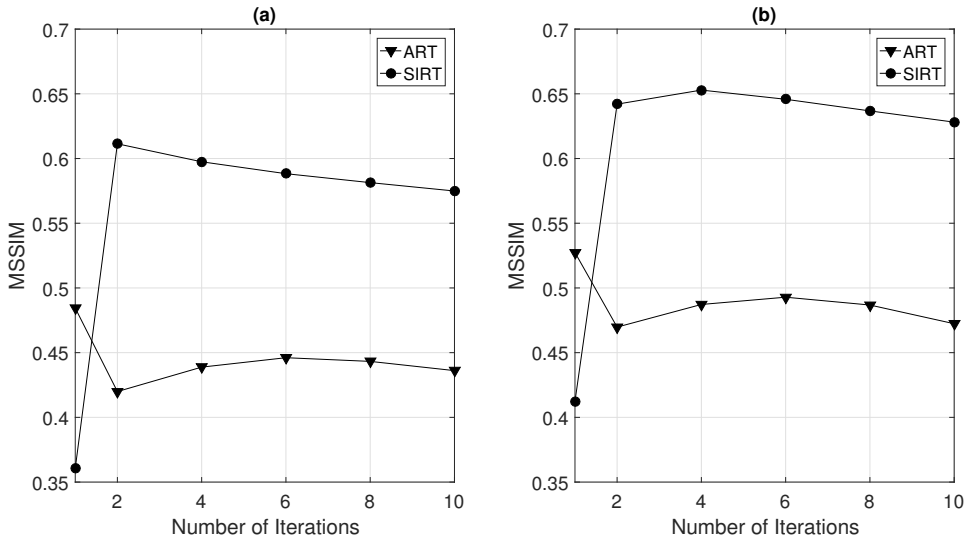

Figure 4.8: ART and SIRT convergence (averaged over 100 runs) in the reconstruction of floor maps (a) 1 and (b) 2.

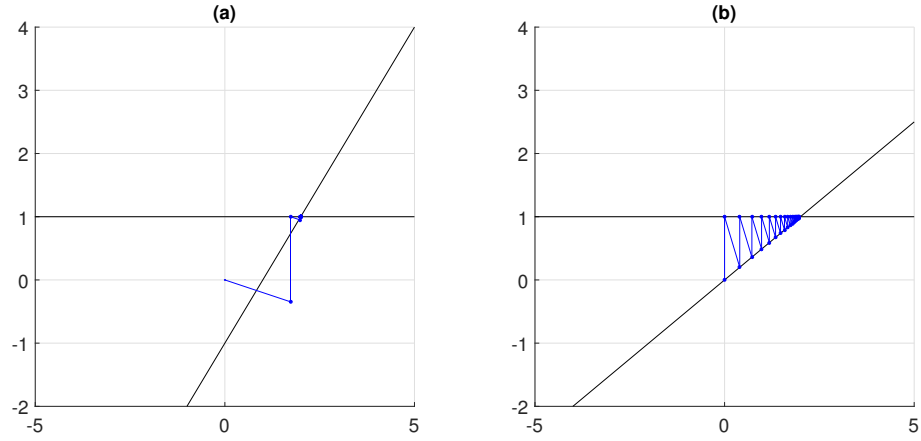

Figure 4.9: Geometric interpretation of Kaczmarz's method.

Figure 4.11 displays the ART and SIRT reconstruction of floor maps 1 and 2. The behavior described by the MSSIM curves in Fig. 4.8 is observed in the ART and SIRT images:

- ART with four iterations is slightly noisier than with one iteration, as Figs. 4.11a,b and Figs. 4.11e,f indicate; this is typical of the semi-convergence [68] inherent to regularization techniques such as ART, where, as the number of iterations increase after a certain point, noise starts to dominate the output;
- SIRT greatly improves when the number of iterations rises from one to four:

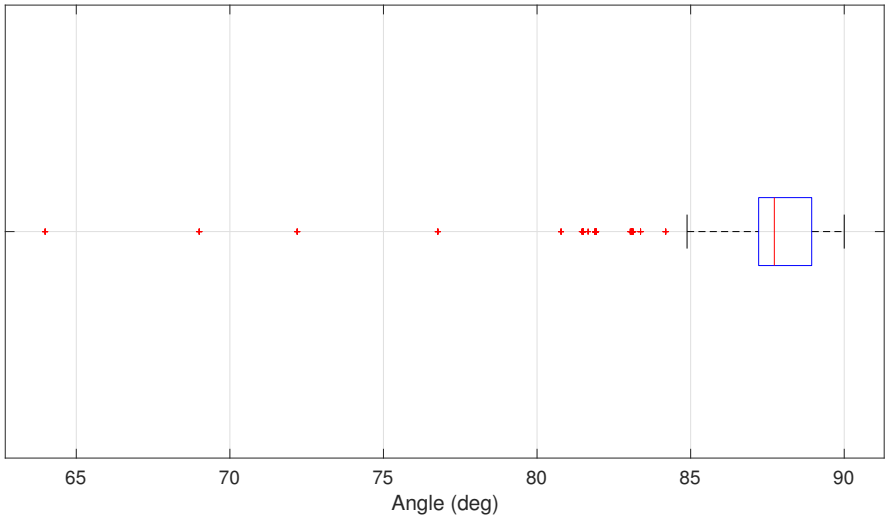

Figure 4.10: Box plot providing descriptive statistics of the angles between the hyperplanes defined by adjacent lines of **A**.

with only one iteration, SIRT reconstructed images are considerably blurred, as Figs. 4.11c,g show; with four iterations that blurring is greatly reduced, as Figs. 4.11d,h indicate;

Furthermore, as already indicated by the MSSIM curves, SIRT yields a much less noisy image than ART. Such a result was somewhat expected, as the propagating electromagnetic energy is being treated as rays in the simulations. This is analogous to the nanometric wavelength of X-ray radiation, and the superior quality of SIRT in X-ray tomography in comparison to ART has already been well documented [72]. This better quality is achieved at the expense of a slower convergence. Nonetheless, for any practical purposes, this increase in convergence time is negligible, if compared to the time required to acquire all samples in a real TWM measurement setup.

In all simulations in the remaining sections, the number of iterations used in ART and SIRT is one and four, respectively.

4.4.2 Reconstruction Quality versus Number of Projections

Fig. 4.12 shows the MSSIM of the reconstructed floor maps for all methods as a function of n [11]. Fig. 4.12a refers to floor map 1 and Fig. 4.12b to floor map 2. In both cases, FBR, DFR [12] and SIRT MSSIM increase with n. However, the MSSIM increment is negligible when n rises from 40 to 80 projections. This can be verified comparing Fig. 4.13d ($n = 40$) and Fig. 4.11d ($n = 80$), which show SIRT reconstructions of floor map 1: they are quite similar. The same applies to

[11] Remember that $\Delta\theta = \lfloor 180/n \rfloor$

[12] The DFR reconstructions used the Central Slice MATLAB® package [84].

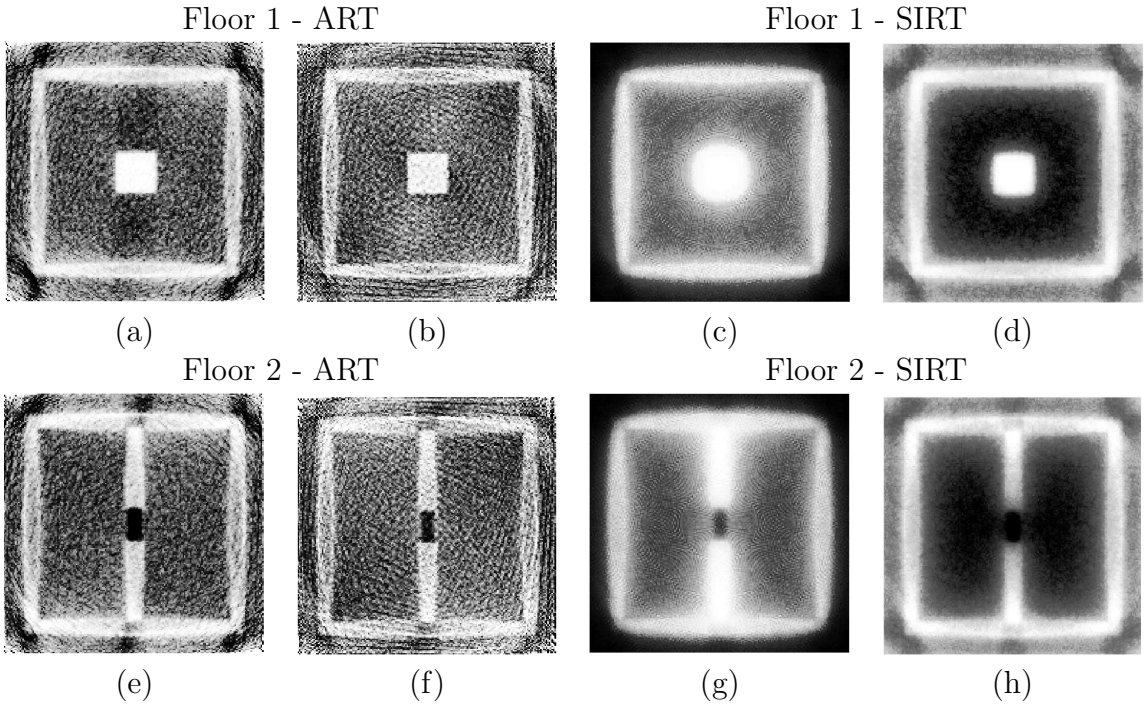

Figure 4.11: Reconstructed floor maps 1 and 2: ART with 1 (a,e) and 4 (b,f) iterations; SIRT with 1 (c,g) and 4 (d,h) iterations.

Fig. 4.13h ($n = 40$) and Fig. 4.11h ($n = 80$), which illustrate SIRT reconstructions of floor map 2.

Some degree of aliasing is inevitable in the reconstructed maps, as the original images are not band-limited. However, for a lower number of projections, the aliasing artifacts become more evident, as Fig. 4.14 shows. Despite that, the reconstructed floor maps are still recognizable with only 10 projections.

The MSSIM curves in Fig. 4.12 indicate that DFR has the worst performance. This can be promptly confirmed observing Fig. 4.13f ($n = 40$) and Fig. 4.14f ($n = 10$), where DFR fails to clearly reproduce a key feature of floor map 2: the door interconnecting the two rooms.

Finally, Fig. 4.12 shows that ART MSSIM has an "anomalous" behavior: it decreases as n augments. This is contrary to what was initially expected, i.e., that a higher n (i.e., a smaller $\Delta\theta$) would produce better quality reconstructed images. Comparing Fig. 4.13c and Fig. 4.14c (floor map 1), one sees that for $n = 40$ there is more "background" noise in the ART reconstructed image. The same applies when comparing Fig. 4.13g and Fig. 4.14g (floor map 2). This effect can be understood through the fact that lowering the number of samples results in low pass filtering. This reduces the high-frequency noise due to multipath. However, details of the floor maps are also lost. In fact, with $n = 10$, the aliasing artifacts corrupt the image significantly. Therefore, in that particular case, it seems that the MSSIM

failed to follow the subjective image quality evaluation.

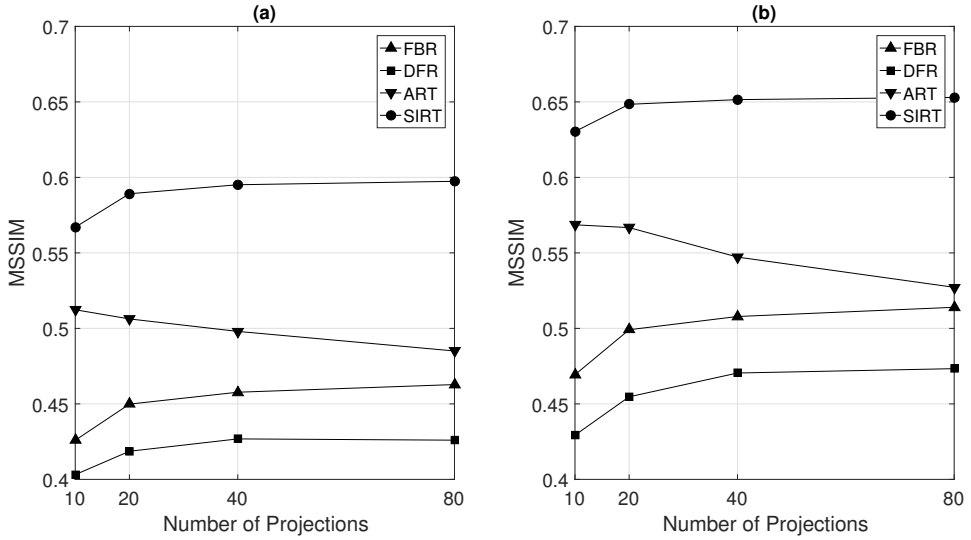

Figure 4.12: MSSIM (averaged over 100 runs) versus number of projections in the reconstruction of floor maps (a) 1 and (b) 2.

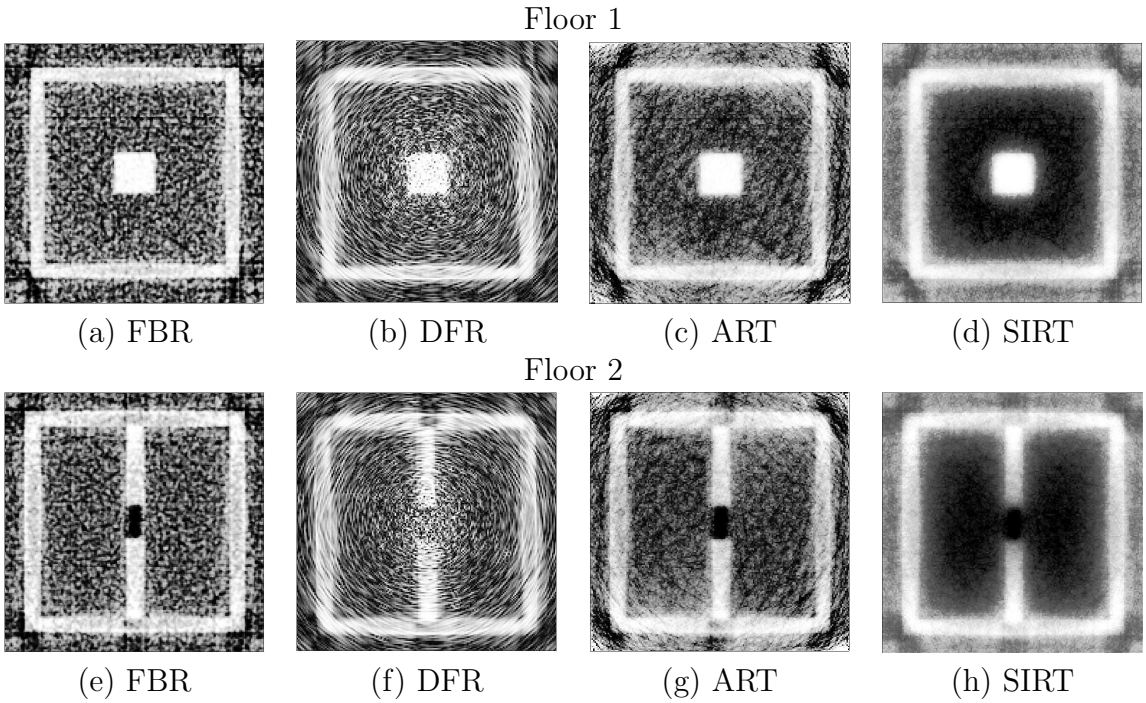

Figure 4.13: FBR, DFR, ART and SIRT reconstruction of floor maps 1 and 2 ($n = 40$).

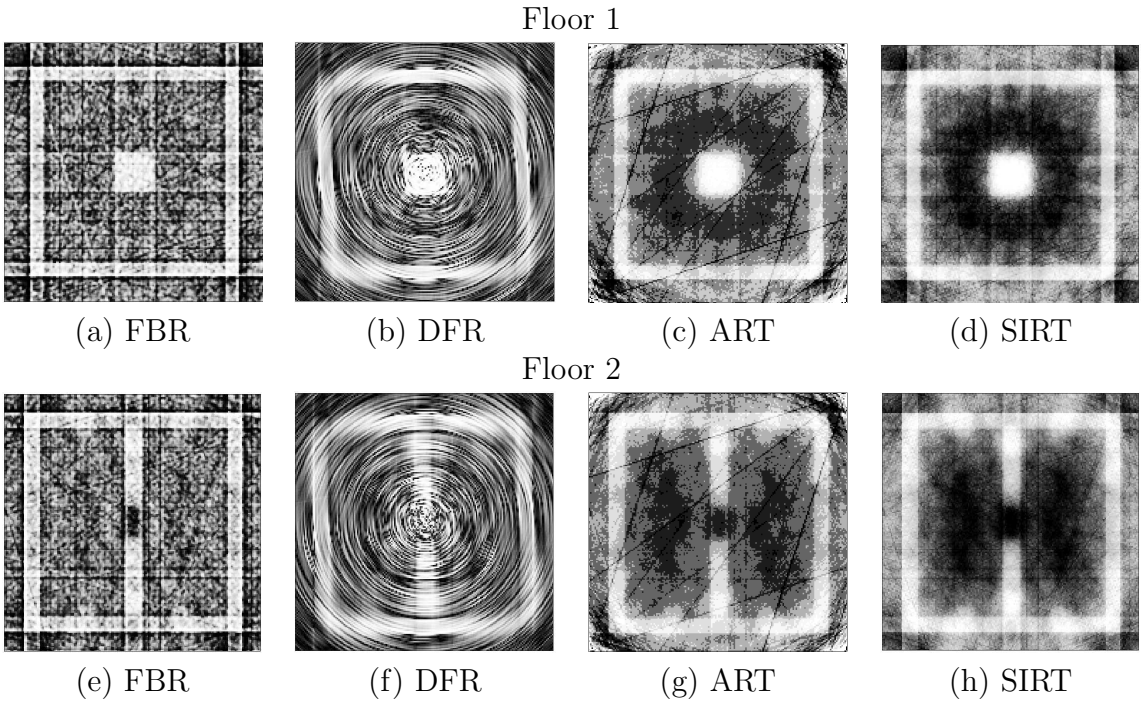

Figure 4.14: FBR, DFR, ART and SIRT reconstruction of floor maps 1 and 2 ($n = 10$).

4.4.3 Effect of Projection Clipping on Reconstruction Quality

All previously reconstructed images in this chapter were obtained for a maximum supportable over-the-air path loss of $L_{\max} = 172$ dB. This resulted in only 1.4% and 3.0% of clipped samples in floor maps 1 and 4, respectively. To better assess the effect of projection clipping on reconstruction quality for all methods, this section evaluates the MSSIM as a function of $L_{\max}$. To increase the value of $L_{\max}$ from 172 dB down to 92 dB, the receiver sensitivity rose from -110 dBm up to 10 dBm. Fig. 4.15 displays the results for both floor maps. SIRT clearly outperforms all other evaluated methods for all values of $L_{\max}$. However, as the receiver is desensitized, SIRT's quality approaches that of FBR.

Table 4.2 informs the percentage of clipped samples at each floor map for each value of $L_{\max}$. For $L_{\max}$ equal to or below 92 dB, the reconstructed images are not usable for any practical purposes, and the floors features cannot be recognized on them . That is why MSSIM for all methods (except ART) falls just slightly when $L_{\max}$ decreases from 92 dB to 52 dB.

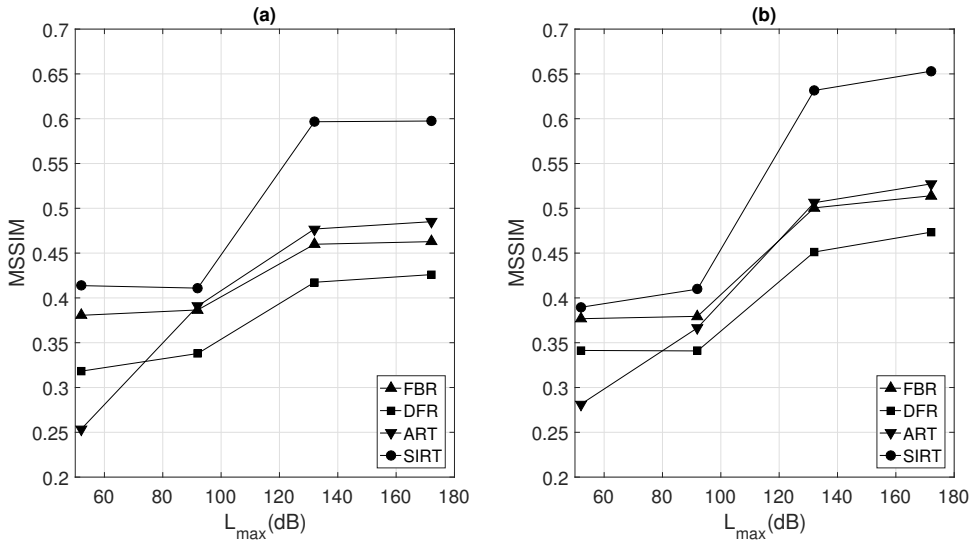

Figure 4.15: MSSIM (averaged over 100 runs) versus $L_{\max}$ in the reconstruction of floor maps (a) 1 and (b) 2.

Table 4.2: Percentage of clipped samples for different values of $L_{\max}$.

$L_{\max}$ (dB)	Percentage of clipped samples	
	Floor 1	Floor 2
172	1.4%	3.0%
132	12%	19%
92	55%	67%
52	80%	83%

4.5 Conclusions

This chapter analyzed the fundamentals of RF-based parallel-beam geometry TWM employing methods originally applied in X-ray CTI: FBR, DFR, ART, and SIRT. For that, a path-loss model was defined to simulate RF propagation. The offset and slope coefficients were empirically defined, using values published in the literature for typical office buildings. The equations were corrupted by Rayleigh noise, to emulate the effect of multi-path reception. Besides that, projection clipping due to receiver's limited sensitivity was also considered.

The simulations showed the superiority of SIRT quality. The Landweber's regularization mitigates noise more efficiently than ART, at the expense of a slightly longer convergence. In fact, ART, due to the quasi-orthogonality of the hyperplanes defined by the lines of $\mathbf{A}$, converges in only one iteration. DFR reconstruction had the worst performance for any number of projections, failing to clearly identify a key feature in floor map 2: the door interconnecting two rooms. MSSIM provided an objective quality metric for the reconstructed images comparison, and, for the

most part, followed the subjective evaluation closely.

Regardless of those conclusions, one issue remains open at this point: the channel model does not take into account the wave nature of the propagating RF energy. As a result, diffracted components are not considered in the simulation. However, at 1 GHz, the 30-cm wavelength is comparable to the obstacles width (50-cm walls), which means that diffraction effects will not be negligible. So, a more sophisticated model, capable of better representing the complexity of the RF propagation environment, is required to yield more realistic results. This is attempted in Chapter 5.

Chapter 5

Finite Element Method Framework for RF Through-The-Wall Mapping

This chapter defines a Finite Element Method (FEM) based framework to allow accurate simulations of the reconstruction of floor blueprints, using Ultra-High Frequency (UHF) narrowband continuous-wave (CW) signals. This framework makes it possible to quickly and accurately evaluate different algorithms – already in use or yet to be proposed – without the need to assemble a full test setup, which might not be available due to budgetary and time constraints. This chapter applies the collection of reconstruction methods studied in the previous chapter under a parallel-beam acquisition geometry. Considering all the drawbacks associated with such a complex problem, a robust and reliable computational setup based on a flexible method such as FEM can be very useful. To the best of our knowledge, this is the first attempt to use FEM in an RF-based TWM problem [85].

5.1 Introduction

5.1.1 RF Electromagnetic Wave Propagation Issues

The simulation model built in Chapter 4 uses path-loss equations corrupted by Rayleigh noise. It employs the geometric optics approximation to the RF propagation (but not considering ray deviation due to refraction). Therefore, it assumes straight single path propagation, i.e., disregards multipath arising from reflections at interfaces and diffraction around corners. While these assumptions hold true for X-Ray tomography, due to the very small wavelength, the same does not apply to UHF signals. In that case, the wave properties of the RF energy must be taken into account to more accurately simulate the RF-based TWM problem. For that, a

model more sophisticated than the one used in Chapter 4 is required. To build such model, a FEM framework will be used. Compared to the path-loss method used in the previous chapter, a FEM RF propagation simulation is capable of providing much more realistic results, as it models the electromagnetic wave interaction with different physical media with much higher detail and fidelity [86, 87]. It is probably the closest one can get to describing the real propagation phenomena, without having to deploy a measurement setup, which sometimes is not possible due to time and budgetary constraints.

5.1.2 Finite Element Method

The Finite Element Method (FEM) is a numerical tool suitable for the solution of general *field problems*, like elasticity, fluid flow, heat transfer and electromagnetic wave propagation. These problems have *field variables* that are subjected to specific *boundary conditions*. Differential equations govern the field variables. The boundary conditions are the specified values of the field variables on the boundaries of the field [88].

A key concept in FEM is the discretization or *meshing*, which is the process of dividing the model geometry into smaller units called *finite elements*. Those units are interconnected at points (1-D geometry), boundary lines (2-D geometry) or boundary surfaces (3-D geometry), common to two or more elements. The *nodal points* are the vertexes of the finite elements. The field variables must be explicitly calculated at the nodal points, using the problem's governing differential equations. The values of the field variables are estimated at non-nodal points using interpolation functions, also referred to as *shape functions*. The number of *degrees of freedom* is equal to the number of finite elements, multiplied by the number of nodal points per element and by the number of values of the field variables that must be calculated at each node [89].

To simulate UHF RF propagation in a parallel-beam acquisition geometry using the proposed FEM model requires solving up to 33440 linear systems (one for each position of the transmitter-receiver pair when using 80 projections with 418 samples per projection) with as much as 652 thousand degrees of freedom per system (when using the standard mesh). Those linear systems are obtained after linearization of the partial differential equations (PDEs) governing the RF propagation problem. To solve such huge linearized stationary models, one might choose between iterative or direct solvers. Due to the complexity of setting up iterative solvers – which involves adequately setting up initial estimates and convergence criteria that might vary depending on the physical interface being simulated – we have opted for using the parallel sparse direct linear solver (PARDISO) [90]. Though it requires more

memory space, it is typically more robust than iterative methods [91].

5.2 RF-Based TWM FEM Model

This section describes the FEM simulation of the parallel-beam geometry TWM setup. The simulation was carried out in COMSOL Multiphysics®, a commercial package which can be applied to electromagnetic wave propagation problems.

5.2.1 Governing Equations and Boundary Conditions

In the RF TWM FEM simulation, the Helmholtz vector equation for harmonic electric fields

$$\vec{\nabla} \times \vec{\nabla} \times \vec{\mathbf{E}}\left(\vec{\mathbf{r}}, t\right) - \gamma \vec{\mathbf{E}}\left(\vec{\mathbf{r}}, t\right) = 0 \tag{5.1}$$

is solved at each nodal point, where $\vec{\nabla} = \frac{\partial}{\partial x}\vec{\mathbf{a}}_x + \frac{\partial}{\partial y}\vec{\mathbf{a}}_y + \frac{\partial}{\partial z}\vec{\mathbf{a}}_z$ is the $\vec{\nabla}$ vector operator in rectangular coordinates and $\vec{\mathbf{E}}\left(\vec{\mathbf{r}}, t\right)$ is the electric field vector in Volts per meter (V/m) at instant t and location $\vec{\mathbf{r}} = x\vec{\mathbf{a}}_x + y\vec{\mathbf{a}}_y + z\vec{\mathbf{a}}_z$. For simplicity, we will thereafter drop the full notation, using simply $\vec{\mathbf{E}}$. The same applies to all other fields. Vectors $\vec{\mathbf{a}}_x$, $\vec{\mathbf{a}}_y$ and $\vec{\mathbf{a}}_z$ are the unit vectors in the direction of the rectangular coordinate axes. Parameter γ is the complex propagation constant, given by

$$\gamma = \sqrt{j\omega\mu_r\mu_0\left(\sigma + j\omega\epsilon_r\epsilon_0\right)} \tag{5.2}$$

where ω is the harmonic field angular frequency (rad/s); σ is the material electrical conductivity (S/m); $\epsilon_0 = 8.85 \times 10^{-12}$ F/m and $\mu_0 = 4\pi \times 10^{-7}$ H/m are the electric permittivity and magnetic permeability of vacuum, respectively; ϵ_r is the relative permittivity and μ_r is the relative permeability of the material medium.

Section 5.2.2 defines the surface current density exciting the model, producing harmonic electric and magnetic fields. Assuming a harmonic magnetic field, Faraday's law can be expressed in phasorial form by

$$\vec{\nabla} \times \vec{\mathbf{E}} = -j\omega\mu_r\mu_0\vec{\mathbf{H}} \tag{5.3}$$

Thereby, the magnetic field at each nodal point can be obtained by calculating the curl of the solution of equation (5.1), i.e.,

$$\vec{\mathbf{H}} = \frac{j}{\omega\mu_r\mu_0}\left(\vec{\nabla} \times \vec{\mathbf{E}}\right) \tag{5.4}$$

The field variables solutions are subjected to the boundary conditions for the

electric and magnetic fields [92]:

$$\left(\vec{\mathbf{E}}_1 - \vec{\mathbf{E}}_2\right) \times \vec{\mathbf{n}} = 0 \tag{5.5}$$

$$\left(\vec{\mathbf{D}}_1 - \vec{\mathbf{D}}_2\right) \cdot \vec{\mathbf{n}} = \rho_s \tag{5.6}$$

$$\left(\vec{\mathbf{H}}_1 - \vec{\mathbf{H}}_2\right) \times \vec{\mathbf{n}} = \vec{\mathbf{K}} \tag{5.7}$$

$$\left(\vec{\mathbf{B}}_1 - \vec{\mathbf{B}}_2\right) \cdot \vec{\mathbf{n}} = 0 \tag{5.8}$$

where $\vec{\mathbf{n}}$ is a unitary vector normal to the boundary between media 1 and 2, $\vec{\mathbf{K}}$ is the surface current density in amperes per meter (A/m), ρ_s is the surface charge density in Coulombs per square meter (C/m^2), $\vec{\mathbf{D}} = \epsilon_r \epsilon_0 \vec{\mathbf{E}}$ and $\vec{\mathbf{B}} = \mu_r \mu_0 \vec{\mathbf{H}}$ are the electric flux density vector (C) and the magnetic flux density vector (Wb), respectively. There are only dielectric materials in the model geometry, so $\rho_s = 0$ at all boundaries and $\vec{\mathbf{K}}$ is different from zero only at the transmitter monopole. This is the field source, described in Section 5.2.2.

5.2.2 Field Source

A time-harmonic surface current density is set over the transmitter monopole surface to excite the RF model. Its complex phasor representation is expressed by

$$\vec{\mathbf{K}} = \mathrm{Re}\left\{\mathrm{K}_0 e^{j\omega t}\right\} \mathbf{a}_z \tag{5.9}$$

with $f = 1$ GHz and $\mathrm{K}_0 = 1.6$ A/m, which corresponds to a current

$$\mathrm{I}_0 = (2\pi r)\,\mathrm{K}_0 = 100mA \tag{5.10}$$

where $r = 1$ cm is the monopole radius. This current generates a vertically polarized electromagnetic wave (with the electrical vector perpendicular to the model plane) with an output power of approximately 10 W [1].

A boundary probe is defined on the receiver monopole, integrating the received electric field over the monopole's surface. Identical antennas are used for both transmission and reception.

[1] This was empirically verified using a FEM model in COMSOL. First, the antenna was placed at the center of a circular PML. Then a probe surface was defined around it, and the electromagnetic wave propagation simulation was carried out. Finally, the outward power flux (W/m^2) through the probe surface was integrated, yielding the transmitter output power.

5.2.3 Model Geometry and Material Properties

The main obstacles present in a floor – walls and doors – have a fixed horizontal cross-section. Considering this symmetry, a 2-D model can be used in the FEM simulation. Employing a 2-D model instead of a 3-D one results in a FEM model with fewer degrees of freedom, which reduces the computational complexity of the simulation. As Figure 5.1 shows, the 2-D models in COMSOL replicate the floor maps depicted in Fig. 4.7. The walls and pillar are assumed to be made of dry concrete, without any steel reinforcement rods. The floors are immersed in a dry atmosphere and surrounded by a circular perfect matching layer (PML), a boundary placed around the model's geometry to prevent reflections at the external interface [93].

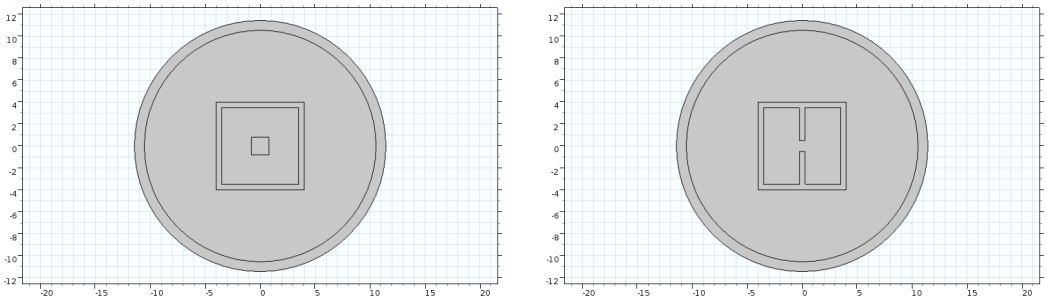

(a) (b)

Figure 5.1: Floor maps (a) 1 and (b) 2 surrounded by a PML in COMSOL.

All media are assumed to be isotropic, homogenous and linear. The electromagnetic properties (at three different frequencies) of dry concrete used in the FEM model are summarized in Table 5.1 [2]. For dry air, $\epsilon_r = \mu_r = 1$ and $\sigma = 0$.

Table 5.1: Electromagnetic properties of dry concrete used in the FEM model.

Freq. (MHz)	μ_r	ϵ_r	σ (S/m)	Ref.
500	1	7.75	0.0200	[94]
1000	1	7.00	0.0473	[79]
2000	1	5.87	0.0830	[80]

5.2.4 Meshing

A key concept in FEM is the discretization or *meshing*, which is the process of dividing the space into *finite elements*. The solution accuracy is directly related to the size of elements in the mesh. Smaller elements lead to a finer mesh, which results in a more accurate solution. However, smaller elements equal more degrees

[2]The RF propagation parameters at 500 MHz have been obtained by interpolation of the values at the nearest available frequencies, as there were no results at 500 MHz in the selected references.

of freedom, which increases the computational cost of the solution. Besides, it also augments the required memory space.

A few alternatives can be exploited to decrease the number of elements, without perceivably affecting the solution accuracy, as follows:

- employ smaller elements where the field gradient is highest, i.e., at media interfaces, and let them be much larger farther away from those boundaries;
- let the elements grow accordingly as one moves away from media interfaces; thereby, the mesh would be finer nearby the media boundaries, and would increasingly, though slowly, become coarser farther away from these areas;
- refine the mesh around corners, to more accurately model the electrical field diffracted components;
- refine the mesh inside obstacles, such as walls and pillars, to better represent fine details of the structures, such as doors and reinforcement steel rods inside the concrete;

Table 5.2 summarizes the main features of the two types of meshes used to build the FEM 2-D models in COMSOL. The *maximum element size* is defined as a function of the carrier wavelength λ. In the standard mesh, the maximum element size is just one-fifth of the wavelength. In the optimized mesh, it is three times larger. The *maximum element growth rate* defines the rate at which the element size grows from one element to another, as one moves from a region with smaller elements to a region with larger elements. In the standard mesh, the growth rate is 30%. In the optimized mesh, it is half this value. The *resolution of narrow regions* parameter defines the number of layers of elements inside narrow regions (such as doors). In the optimized mesh, this number is three times the value used in the standard mesh. The *element size scaling factor* is a refinement factor applied to finite elements in sharp corners. The lower this value, the finer the mesh at those regions. Note that in the optimized mesh this parameter is one-fourth of the value used in the standard mesh.

Table 5.2: Meshing parameters.

Mesh	Standard	Optimized
Max. Element Size	$\lambda/5$	$3\lambda/5$
Max. Element Growth Rate	1.3	1.15
Resolution of Narrow Regions	1	3
Element Size Scaling Factor	1	0.25

Fig. 5.2 illustrates triangular meshes in three selected regions of 2-D models built in COMSOL. The first line (a,b,c) shows standard meshes, and the second line (d,e,f)

depicts optimized meshes in those same regions. One sees that in the standard mesh the number of elements is much higher. However, in the optimized mesh, the mesh is finer at critical areas, such as around corners and at media boundaries in general. Fig. 5.2(c,f) show a section with two perpendicular concrete walls and a door. Note the much finer mesh at the door, as a result of the higher *resolution of narrow regions* parameter.

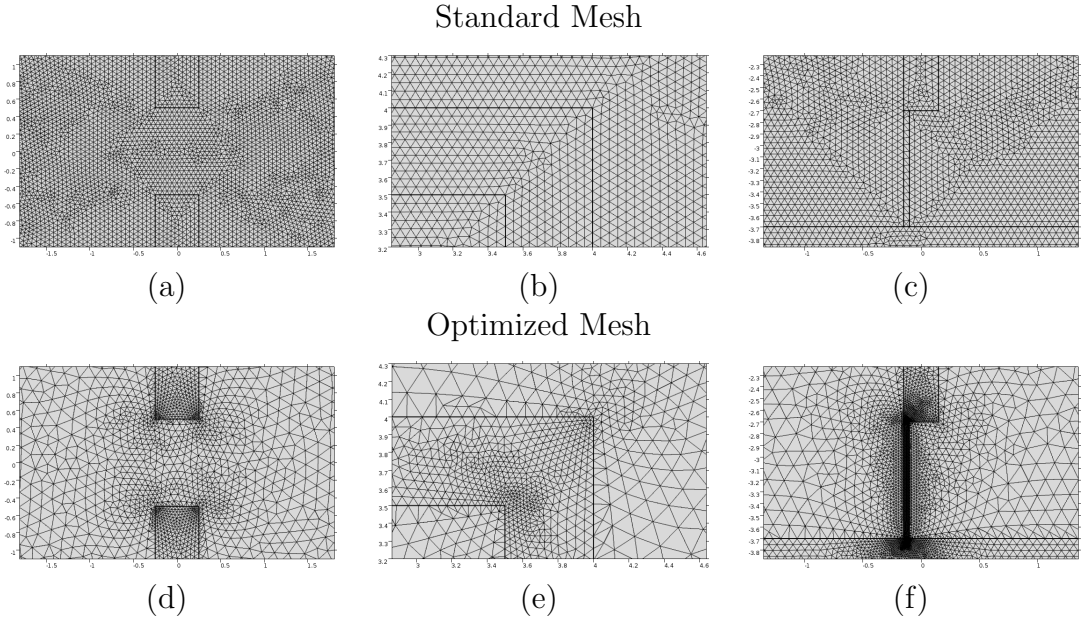

Figure 5.2: Triangular meshes in selected sections of 2-D FEM models.

Table 5.3 lists the number of elements and degrees of freedom, as a result of meshing floor maps 1 and 2 (see Fig. 5.1) using the standard and optimized configurations. Note that, as triangular elements are being used, the number of degrees of freedom is approximately twice the number of elements. In both floor maps, the use of the optimized mesh reduces the number of elements (and the number of degrees of freedom) roughly six times.

Table 5.3: Standard and optimized meshes (at 1 GHz) of floor maps 1 and 2.

Parameter	Floor map			
	1		2	
	Standard	Optimized	Standard	Optimized
Triangular Elements	324574	53836	324268	56016
Boundary Elements	3540	1858	3632	1996
Degrees of Freedom	651989	106873	651209	112153

Using the standard mesh in all simulations would exact a prohibitive computational cost [3]. Therefore, Section 5.3 employs only optimized mesh, with the excep-

[3]Running a simulation in COMSOL (floor map 2 at 1 GHz, $\Delta\rho = 9$ cm and $n = 40$) with

tion of Section 5.3.6, which evaluates the effect on reconstruction quality of using the optimized mesh instead of the standard one.

5.2.5 Sinogram Acquisition

To acquire the sinogram using a parallel-beam geometry in the FEM model, the transmitter and receiver pair moves along $L = 12.51$-meter long lines, as Fig. 5.3 illustrates [4]. Samples are collected every $\Delta\rho = \lambda/10 = 3$ cm. To obtain each sample, the electric field must be calculated over the entire test area. From equation (4.32), $m = \left\lfloor \frac{L}{\Delta\rho} + 1 \right\rfloor = 418$ samples per angle. The samples collected along a line provide a discrete Radon projection. Radon projections were obtained at $n = 80$ angles uniformly spaced in $[0,\pi)$, i.e., $\Delta\theta = 2.25$ degrees. Consequently, the sinogram has 33440 samples. To simulate lower sampling rates appropriate subsets of the sinogram are selected.

Unlike the simulations carried out in Chapter 4, the transmitter-receiver distance now must be larger than L. The extra distance at each end (transmitter and receiver end) was set to $W = 1.2$ meters, which is the reflector largest dimension. As a result, the transmitter-receiver distance becomes 14.91 meters.

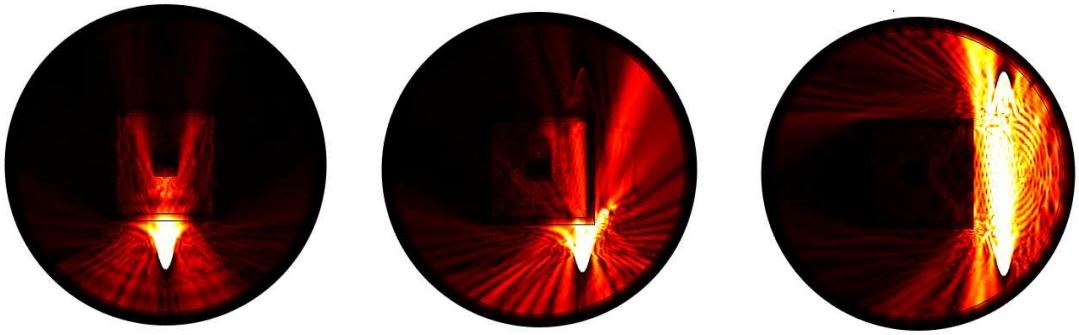

(a) (b) (c)

Figure 5.3: Electric field 2-D maps generated in COMSOL using the FEM model. The sequence of images from (a) to (b) illustrates the movement of the transmitter-receiver pair along parallel lines during the acquisition phase.

From Fig. 5.3 the superiority of the RF-based TWM simulation using a FEM model in relation to the path-loss formulation applied in Chapter 4 becomes evident.

the standard mesh took 104.5 hours (i.e., 4 days and 7 hours). With the optimized mesh, the same simulation lasted only 11 hours. Both simulations were run on the same machine, with the following specifications: operational system Microsoft Windows 7 Ultimate, processor Intel Core i7-4770 CPU @ 3.4 GHz (4 cores, 8 processors), 16 GB RAM and 31.8 GB virtual memory. Note that, even though the number of degrees of freedom in the optimized mesh is roughly 6 times smaller than in the standard mesh, the mesh optimization reduced the processing time 9.5 times. This non-linear relationship resulted from the swap operations to the hard disk (which has a much slower access time than the RAM) which had to be performed when running the simulation with the standard mesh, due to the much higher number of degrees of freedom.

[4]For a more detailed visual representation of the parallel-beam acquisition geometry, please refer to Fig. 4.3.

The electric field 2-D maps show interference patterns due to the superposition of the direct and reflected waves. They also depict the diffracted components around and behind obstacles along the propagation path. The planar distribution of the electromagnetic energy radiated from the transmitter is also noticeable, as a result of the transmitting antenna horizontal radiation pattern. The simplified geometric optics approximation adopted in Chapter 4 disregarded reflections, diffraction, and antenna horizontal beamwidth. Besides that, the antenna gain there was simply a value added to the transmitter output power to obtain the effective isotropic radiated power (EIRP).

5.2.6 First Fresnel Zone and Inter-Sample Distance

The Huygens' principle states that each point on a wavefront acts as an isotropic elementary radiator [95]. Based on that fundamental, the Fresnel zones are defined. The Fresnel zones are volumes of constructive and destructive interference. The boundaries of those zones are ellipsoidal surfaces, whose foci are placed at the transmitter and the receiver. These boundaries are the geometric place of the points on the wavefront with

$$(d_{\mathrm{TX}} + d_{\mathrm{RX}}) - d = n\lambda/2 \tag{5.11}$$

where d is the direct distance between the transmitter and the receiver, d_{TX} and d_{RX} are the distances between the wavefront point and the transmitter and the receiver, respectively. Parameter n indicates the order of the Fresnel zone.

If $(d_{\mathrm{TX}} + d_{\mathrm{RX}}) - d < \lambda/2$, then point B is within the first Fresnel zone. Therefore, the first Fresnel ellipsoid defines a volume of constructive interference. As most of the energy of the propagating electromagnetic wave is contained in the first Fresnel zone, its clearance (absence of obstacles within it) is meticulously analyzed during the design of point-to-point microwave links [96]. In the specific case of RF-based TWM, for any given location of the transmitter-receiver pair, the obstacles contained within the first Fresnel zone are the ones effectively mapped, i.e., they are the obstacles which alter characteristics of the propagating wave and imprint modifications on the collected sample.

As Fig. 5.4 indicates, in a parallel-beam acquisition geometry, if two samples along a line defined by a given θ were too close (i.e., if $\Delta\rho$ is too small), the first Fresnel ellipsoids of the two links would have a high superposition. This would result in the two samples being approximately equal. So, after a certain point, arbitrarily increasing the linear sampling rate (by diminishing $\Delta\rho$) in RF TWM does not improve reconstruction quality. This relationship will be explored in Section 5.3.

In planar models, the Fresnel ellipsoids become ellipses. Equations (5.12)

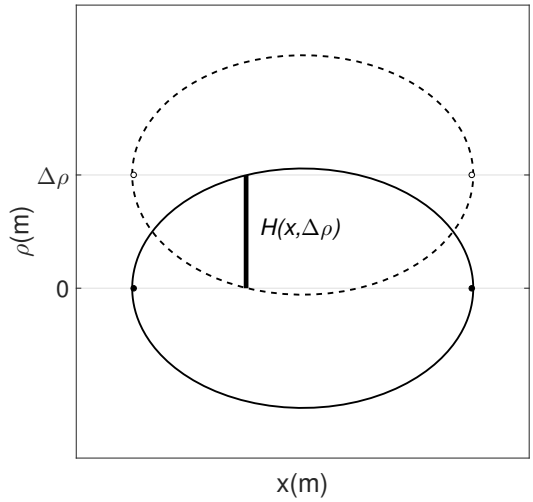

Figure 5.4: Superposition of the first Fresnel zones of adjacent links. The black and white dots pinpoint the locations of the transmitter-receiver pair.

and (5.13) define the ellipses shown in Fig. 5.4.

$$\frac{x^2}{a^2} + \frac{\rho^2}{b^2} = 1 \tag{5.12}$$

$$\frac{x^2}{a^2} + \frac{(\rho - \Delta\rho)^2}{b^2} = 1 \tag{5.13}$$

Parameter b is the ellipse's minor semi-axis length. So, it is equal to the radius of the first Fresnel zone when $d_{\mathrm{TX}} = d_{\mathrm{RX}} = d/2$. The radius of the first Fresnel zone is given by $R = \sqrt{\frac{\lambda d_{\mathrm{TX}} d_{\mathrm{RX}}}{d}}$ [96]. So,

$$b = \frac{\sqrt{\lambda d}}{2} \tag{5.14}$$

Parameter a is the ellipse's major semi-axis length. From basic geometry and the very definition of an ellipse, one obtains the well-known relation

$$a = \sqrt{b^2 + c^2} \tag{5.15}$$

where c is the distance between each focus and the ellipse center. As the transmitter and receiver are located at the foci, one has that $d = 2c$, so

$$c = d/2 \tag{5.16}$$

Replacing b and c in equation (5.15) by equations (5.14) and (5.16), respectively, one gets

$$a = \frac{d}{4}\left(d + \frac{\lambda}{4}\right) \tag{5.17}$$

In Fig. 5.4, H expresses the height of the intersection of the two ellipses as a function of x and $\Delta\rho$. It is defined by

$$H(x, \Delta\rho) = \frac{2b}{a}\sqrt{a^2 - x^2} - \Delta\rho \tag{5.18}$$

To obtain the percentage of superposition of the two adjacent ellipses, one must integrate H along the x-axis between $x = -a$ and $x = +a$ (yielding the intersection area), and divide the result by the area of the ellipse, i.e.,

$$s(\Delta\rho) = \frac{100}{\pi ab}\int_{-a}^{+a} H(x, \Delta\rho)dx \tag{5.19}$$

Fig. 5.5a plots the percentage of superposition as a function of $\Delta\rho/\lambda$. For example, with $\Delta\rho = 3\lambda/10 = 9$ cm, this percentage is approximately 95%. From Fig. 5.5b, the high level of superposition for this value of $\Delta\rho$ becomes evident. Section 5.3 evaluates this issue in deeper detail through FEM simulations in COMSOL.

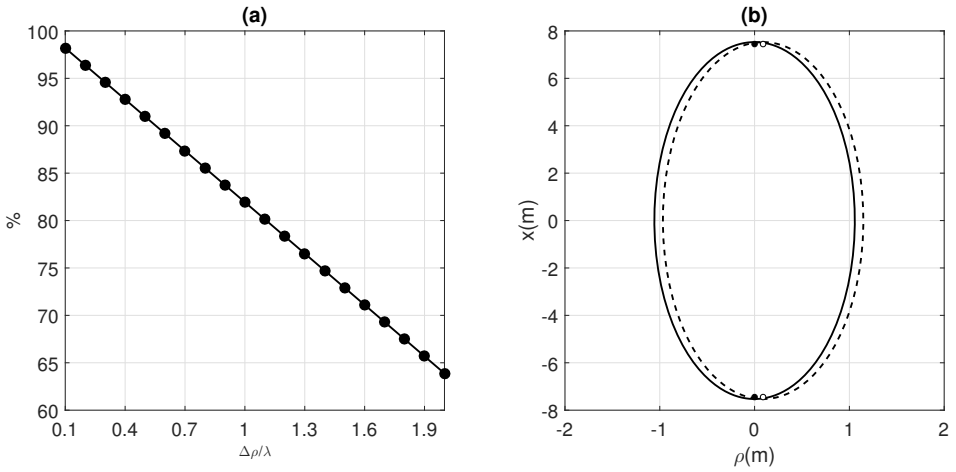

Figure 5.5: Superposition of the first Fresnel zones of adjacent links: (a) as a function of $\Delta\rho/\lambda$; (b) for $\Delta\rho = 9$ cm. The black and white dots in (b) pinpoint the locations of the transmitter-receiver pair.

5.2.7 Antenna Design

As a 2-D model is being used, it is necessary to select an antenna with a constant horizontal cross section, such as a monopole with a cylindrical parabolic reflector [97]. Due to the tiny skin depth at 1 GHz in metals, the reflector was configured as a perfect electrical conductor surface (no width, zero skin depth). The monopole center was placed at the focal line of the reflector. Fig. 5.6a shows the antenna horizontal cross section. The selected antenna geometric parameters were:

- Monopole radius: $r = 1$ cm;
- Focal distance: $p = \lambda/4 = 7.5$ cm;
- Reflector aperture: $D = 1.2$ m;
- Reflector length: $W = \frac{(0.5D)^2}{4p} = 1.2$ m.

The horizontal radiation pattern of the antenna at 1 GHz shown in Fig. 5.6b was obtained through FEM simulations, placing the receiver probe in the far field region, i.e., farther than the Fraunhofer distance [98]. At the selected central frequency, the designed antenna has a maximum gain of 14 dBi, 20 degrees half-power beamwidth, and a 30 dB front-to-back ratio.

A high antenna gain is required to minimize the effects of multipath reception. However, for a fixed operational frequency, there is a trade-off between the antenna gain and antenna dimensions: as the sinogram acquisition process requires moving the transmitter-receiver pair through several locations, the antenna cannot be too large. The dimensions of the designed antenna allow it to be placed on the roof of a car, or on-board a mobile robot. In a real setup to collect field measurements, a parabolic antenna would be used instead. At 1 GHz, the parabolic reflector would have a 75-cm diameter to provide a 14 dBi gain [5].

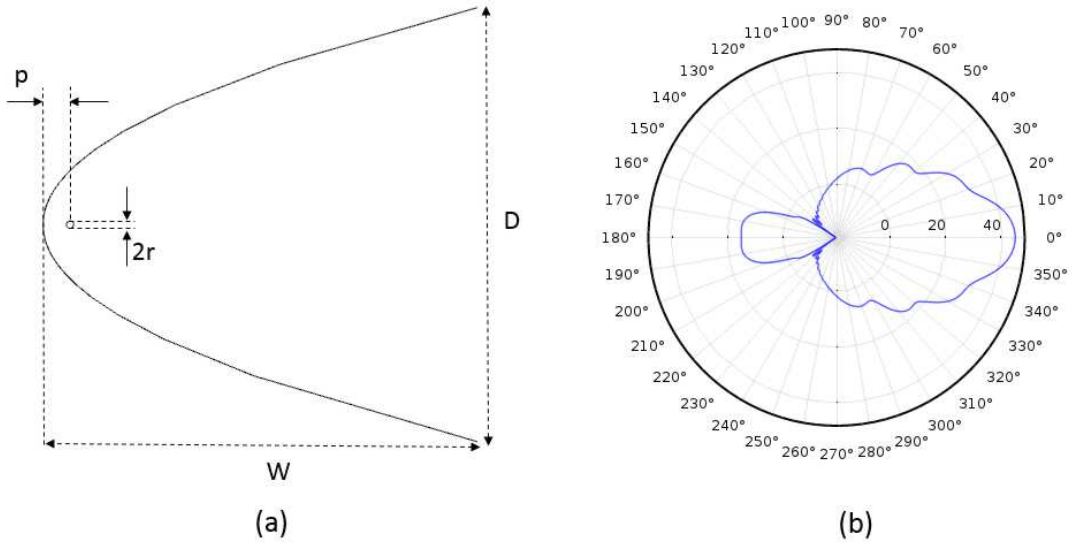

Figure 5.6: (a) Cross-section of the monopole and the cylindrical parabolic reflector; (b) Horizontal radiation pattern of the antenna.

[5]Using antenna model KP10F-820 as reference [99]. It has a 3-meter parabolic dish which provides a 26 dBi gain at 960 MHz. Halving the diameter of the reflector results in a 6 dB reduction in gain. So, with a 75-cm dish (one-quarter of the original diameter), the gain would be approximately $(26 - 2 \times 6)$ dBi = 14 dBi.

5.3 Simulation Results

This section presents the results of the RF-based TWM simulations applying the proposed FEM model. With the exception of Sections 5.3.5, 5.3.6 and 5.3.7, the simulations employ the optimized mesh at $f = 1$ GHz using the antenna specified in Section 5.2.7. MSSIM provides an objective metric for quality assessment of the FBR, DFR, ART and SIRT, using the same configuration as defined in Section 4.3.7. The number of iterations of the algebraic methods is the same as defined in Section 4.4.1. Projection clipping due to limited receiver sensitivity is not considered at this point, unless explicitly indicated. The luminance of all reconstructed images has been equalized for contrast enhancement and better visualization. This section is organized as follows:

- Subsection 5.3.1 compares FBR, DFR, ART and SIRT with and without projection clipping; SIRT outperforms the other techniques in both cases, so the remainder subsections focus only on that method;
- Subsection 5.3.2 empirically evaluates the reconstruction quality as a function of the number of projections;
- Subsection 5.3.3 assesses the improvement on reconstruction quality achieved by applying a non-linear low-pass filter to the sinogram, in order to mitigate high-frequency components related to multi-path reception; such evaluation assumes that there is information loss due to projection clipping;
- Subsection 5.3.4 empirically evaluates the reconstruction quality as a function of the number of samples along a projection, and relates it to the formulation introduced in Section 5.2.6; in lower sampling rates, up-sampling is used to improve the reconstructed images resolution;
- Subsection 5.3.5 verifies the reconstruction image degradation due to decreasing antenna directivity;
- Subsection 5.3.6 compares the reconstruction using the standard and optimized meshes;
- Subsection 5.3.7 correlates reconstruction quality and operational frequency;
- Subsection 5.3.8 proposes the use of a simple method, which combines segmentation and morphological processing, to convert the gray-scale reconstructed images to binary occupancy grids, in preparation for its use in automated applications [77];

The reconstructed images quality is much lower than the ones achieved by the same methods in Chapter 4. It was expected, as the path-loss model used in the previous chapter was too simplistic, disregarding relevant wave propagation phenomena in the UHF band, such as diffraction. The RF-based TWM FEM model proposed in this chapter represents this physical reality with much higher accuracy, reducing the gap between the simulation results and the ones that would be expected in the real world. This can be promptly verified by comparing the reconstructed images listed in this section with the ones obtained from field measurements and presented in [5, 6, 8, 70].

5.3.1 Overall Comparison of Reconstruction Methods Quality

From the fundamentals of the reconstruction algorithms studied in Chapter 4 and from the RF-based TWM FEM model proposed in this chapter, the reconstruction errors can be roughly grouped into four classes:

i) errors due to the particularities of the interaction of the RF energy with the intervening absorbing obstacles, being caused by multi-path propagation (reflections and diffraction), by the RF energy spreading into many directions as it is radiated (which is governed by the antenna radiation pattern), ray deviation (refraction), and by inhomogeneities and anisotropies of the materials [6]; this type of errors cannot be suppressed nor mitigated by increasing the number of samples per projection (m) nor the number of projections (n).

ii) intrinsic errors of each reconstruction method, such as interpolation errors in FBR and DFR, or convergence issues in ART and SIRT;

iii) errors due to limited receiver sensitivity (projection clipping);

iv) aliasing artifacts due to undersampling.

This section considers all these issues as a whole, comparing the reconstruction quality (both visually and using the MSSIM) of FBR, DFR, ART and SIRT.

Fig. 5.7 shows, from left to right, the reconstruction of floor maps 1 and 2 using FBR, DFR, ART and SIRT, with uniform sampling and without any post-processing, other than histogram equalization for contrast enhancement. Subjectively, it is evident that SIRT outperforms all other reconstruction methods, which is confirmed by the MSSIM values. As Fig. 5.8 indicates, the same conclusion is

[6] However, this specific problem will not be present in the reconstructed maps obtained from the FEM model built in COMSOL, as we assumed all materials to be homogenous, isotropic and linear.

reached when samples are randomly "clipped" (i.e., cutting any signals below the receiver sensitivity). In that scenario, SIRT reconstructed floor maps (Fig 5.8d,h), though heavily corrupted, still discernibly portray both floors main features.

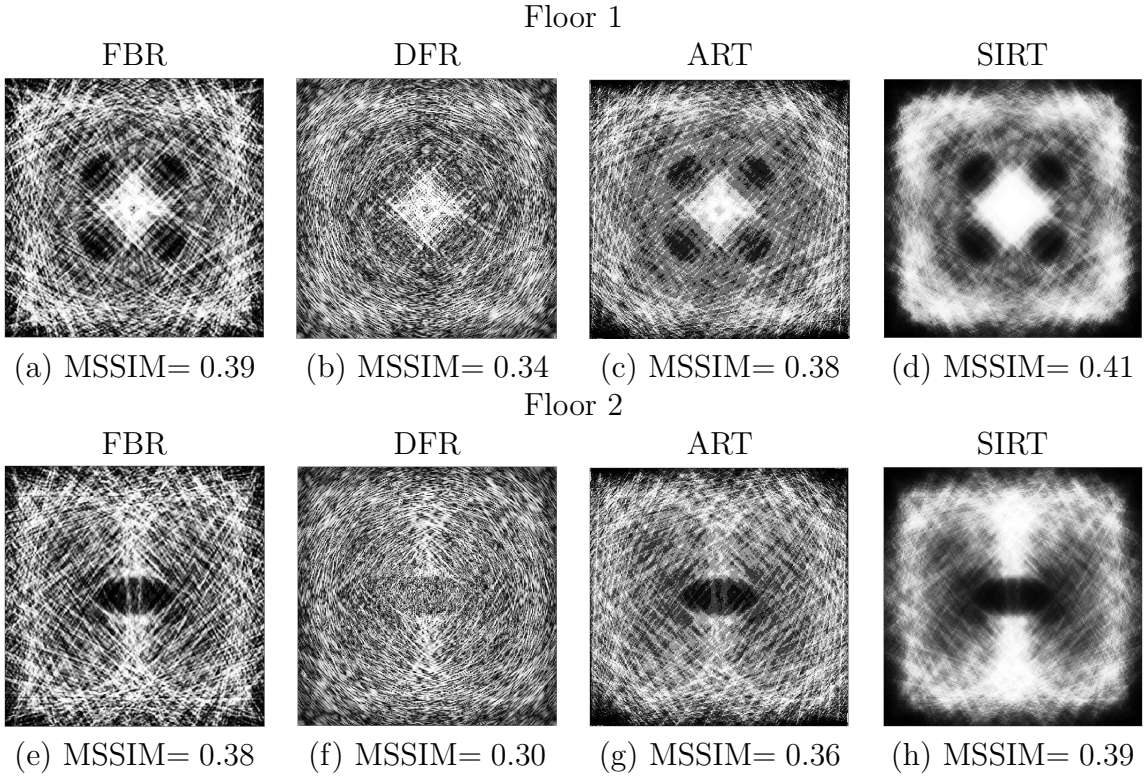

Figure 5.7: Reconstruction with uniform sampling ($\Delta\rho = 3$ cm and $n = 80$).

The superiority of SIRT had already been established in Chapter 4, being now reinforced under more sophisticated (and realistic) simulation scenarios. Another result from the previous chapter that was also confirmed here is the poor performance of DFR. As in Chapter 4, DFR had the worst reconstruction quality. Though well suited to X-ray CTI reconstruction [100], DFR seems not to perform adequately in RF-based TWM. The subsequent sections further explore SIRT related issues.

5.3.2 SIRT Quality versus Number of Projections

Fig. 5.9 depicts the SIRT reconstructed floor maps using 10, 20, 40 and 80 projections. As in Chapter 4, it is perceivable that with as few as 10 projections, the floor features are still recognizable in the reconstructed images. However, with $n = 10$ the reconstructed floor maps are heavily corrupted by undersampling artifacts, particularly floor 1. The results suggest that between 20 and 40 projections should be collected for proper reconstruction.

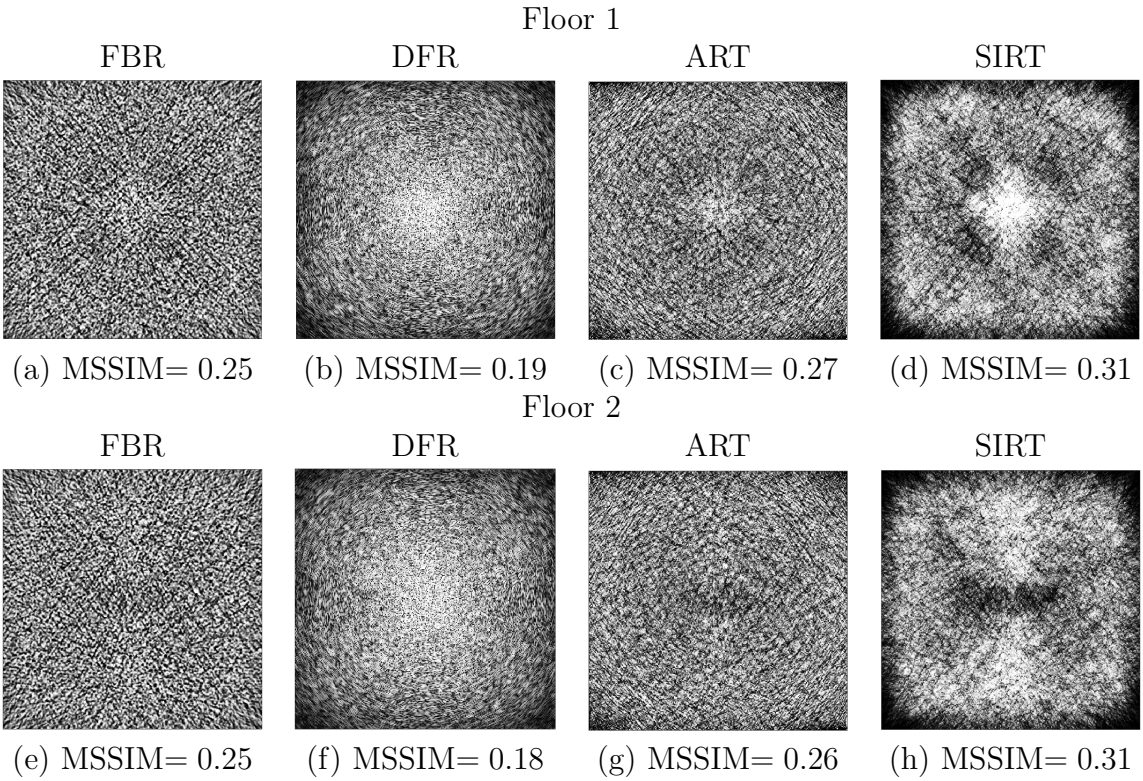

Figure 5.8: Reconstruction with random clipping of 20% of the samples ($\Delta\rho = 3$ cm and $n = 80$).

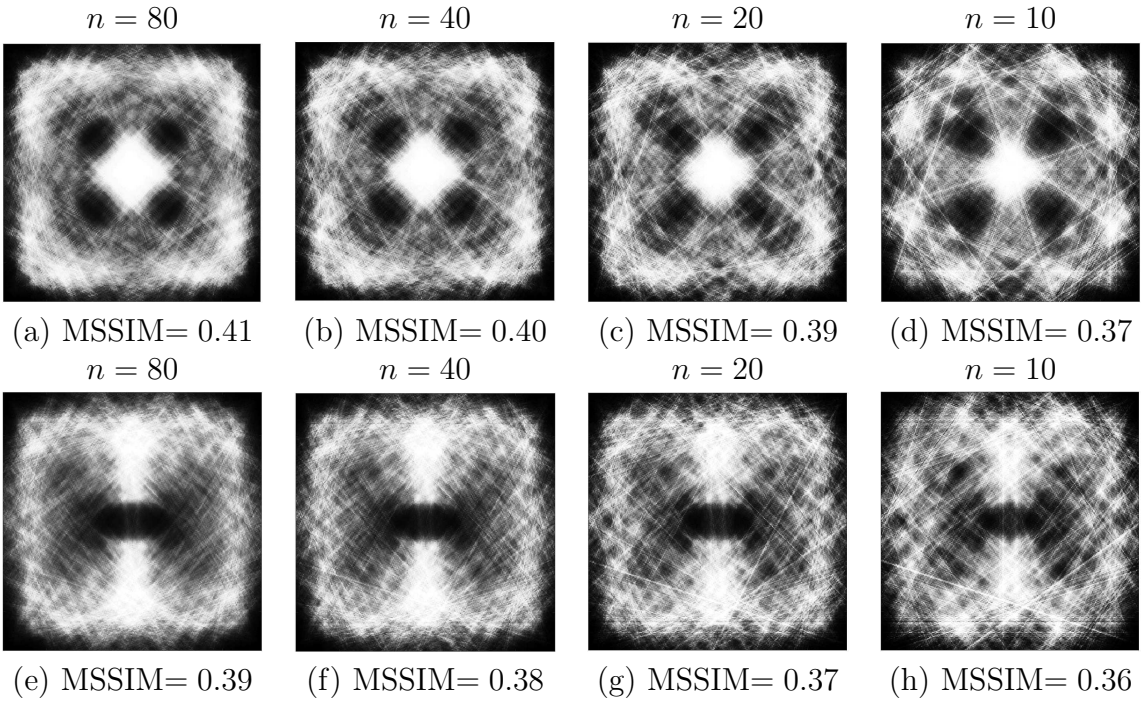

Figure 5.9: SIRT reconstructed floor maps 1 and 2 ($\Delta\rho = 3$ cm and $n = 80, 40, 20, 10$).

5.3.3 Improving SIRT Quality with Sinogram Low-Pass Filtering

We propose low-pass filtering the sinogram to smooth fluctuations in the received signal due to multipath propagation. For that, a median filter has been selected, a first order-statistics non-linear filter which causes significantly less blurring than a linear mean filter [71]. The filtering effects can be better understood in Fig. 5.10, which shows the Radon projections obtained in floor 1 at $\theta = 0$ degrees before (a) and after (b) applying the median filter. The attenuation spikes at $\rho = \pm 2$ m are almost completely filtered out. All sinograms and individual Radon projections are expressed in the logarithmic scale (dB). The dashed lines in Fig 5.10a,b represent the Radon projections that would be obtained without ray bending (no refraction) and with single path (no reflection nor diffraction) propagation. The median filter mask is a 10×3 rectangle. Therefore, at 1 GHz, for $\Delta\rho = 3$ cm and $\Delta\theta = 4.5$ degrees, the mask encompasses samples within one wavelength (for a fixed θ) and three adjacent angles (projections).

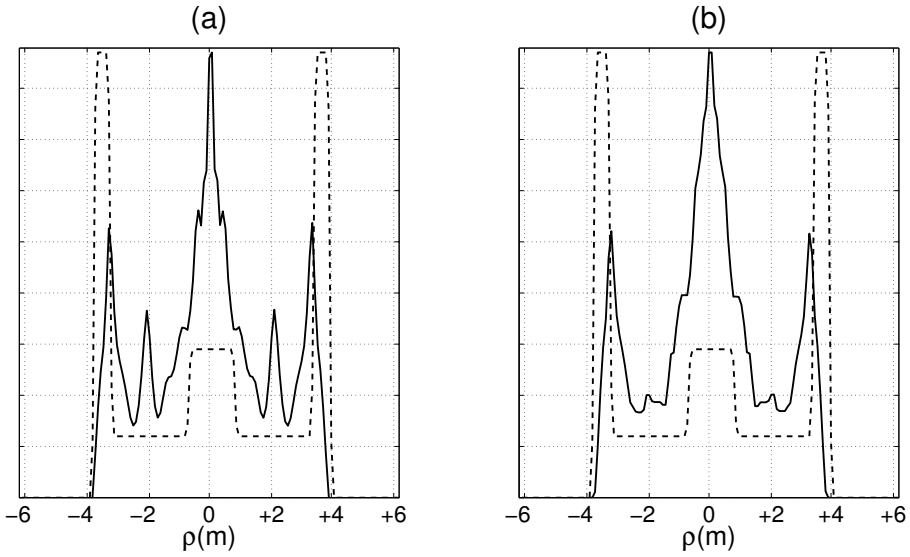

Figure 5.10: Radon projections from floor map 1 taken at $\theta = 0$ degrees before (a) and after (b) applying the median filter. The dashed line indicates the Radon projection that would be obtained in the ideal case, i.e., straight line propagation without multi-path reception and without projection clipping.

Fig. 5.11 shows the sinograms of floor maps 1 (first line) and 2 (second line). The first sinogram of each floor (a,e) is the one which would be achieved if the RF energy propagated along straight lines, i.e., without refraction and diffraction (see dashed lines in Fig 5.10). The second sinogram of each floor (b,f) is the one obtained from the RF-based TWM simulation. The third (c,g) represents the effect of randomly clipping 20% of the samples. The fourth sinogram of each floor (d,h) shows the result of the low-pass filtering.

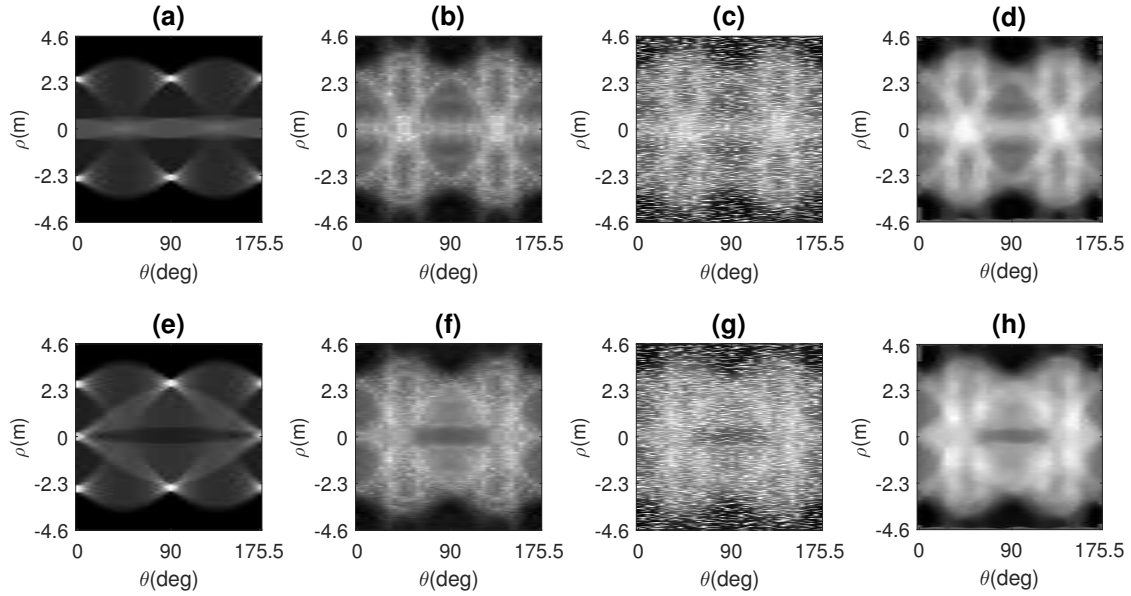

Figure 5.11: Sinograms of floor maps 1 and 2 ($\Delta\rho = 3$ cm, $n = 40$).

Fig. 5.12 illustrates the enhancement of the reconstructed image quality when sinogram low-pass filtering is applied. The improvement is clearly perceptible. The MSSIM values follow the subjective evaluation.

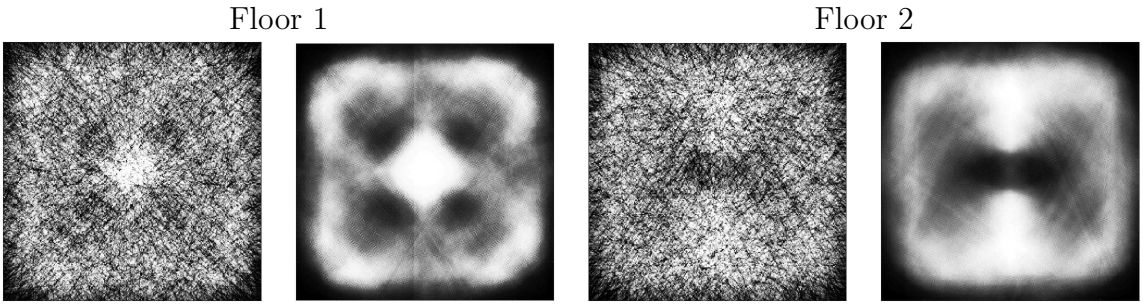

(a) MSSIM= 0.31 (b) MSSIM= 0.36 (c) MSSIM= 0.27 (d) MSSIM= 0.32

Figure 5.12: SIRT reconstruction of floor maps 1 and 2 ($\Delta\rho = 3$ cm and $n = 40$) with random clipping of 20% of samples, before (a,c) and after (b,d) applying the median filter.

5.3.4 Increasing $\Delta\rho$ while Preserving Acceptable SIRT Quality

The spectral contents of the floor maps used defined in Fig 4.7 are not band-limited. However, the UHF electromagnetic wave wavelength and the aperture of the antennas radiation pattern smooth the projections, resulting in information loss at the highest frequencies [72]. Based on these considerations, and on the formulation presented in Section 5.2.6, it can be expected that increasing $\Delta\rho$, up to a certain point,

will not perceptually degenerate the reconstructed image quality. This expectation is experimentally confirmed. Fig. 5.13 shows the SIRT reconstructed floor maps with $\Delta\rho = 2\lambda$. From the graphic on Fig. 5.4a, one sees that for that $\Delta\rho$ there is still a 64% superposition of the first Fresnel zones of adjacent links. Fig. 5.13a,c show the reconstructed floor maps. Due to the smaller number of samples along each projection [7], the resulting images have low resolution [8]. This can be mitigated if, before the reconstruction, the sinogram is up-sampled. In up-sampling, a new sequence is obtained inserting $K-1$ zeros between the original samples. Then, a low-pass filter (referred to as an interpolation filter in this context[9]) is applied. Up-sampling produces an approximation of the results that would be obtained if a higher sampling rate had been used.

The results of applying an up-sampling factor of $K = 20$ are portrayed in Fig. 5.13b,d. The results are quite similar to those obtained applying the median filter in Section 5.3.3, but with the advantage of having being achieved at a much lower sampling rate.

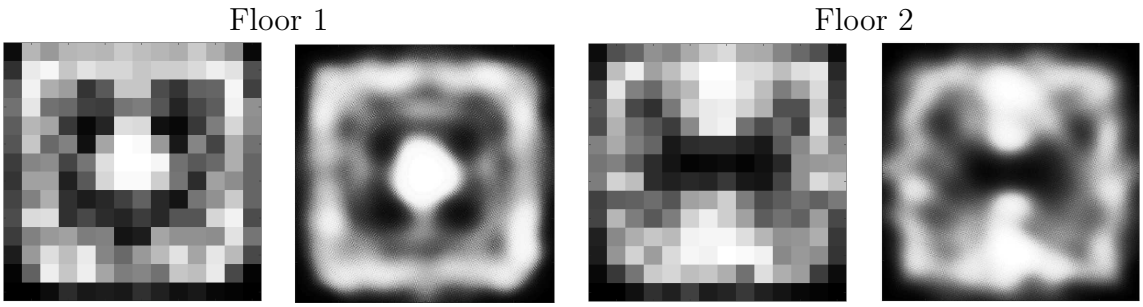

(a) MSSIM= 0.48 (b) MSSIM= 0.41 (c) MSSIM= 0.32 (d) MSSIM= 0.36

Figure 5.13: SIRT reconstruction of floor maps 1 and 2 ($\Delta\rho = 2\lambda$ and $n = 40$) without (a,c) and with (b,d) sinogram up-sampling.

Regarding the MSSIM values in the reconstructed floor 1, Fig. 5.13a had a MSSIM greater than that of Fig. 5.13b (0.48 against 0.41). This obviously does not correspond to the human subjective perception of image quality, as Fig. 5.13b is clearly better. This anomaly can be explained by the fact the Fig. 5.13a resolution is too poor (14×14 pixels), and the moving window used to calculate the MSSIM becomes so small that the results revert to those of pixel-by-pixel comparison metrics.

[7] From equation (4.32), $m = \left\lfloor \frac{L}{\Delta\rho} + 1 \right\rfloor = 21$, for $L = 12.51$ meters and $\Delta\rho = 60$ cm.

[8] From Section 4.3.5, the reconstructed image resolution is $2\left(\left\lfloor \frac{m}{2\sqrt{2}} \right\rfloor \times \left\lfloor \frac{m}{2\sqrt{2}} \right\rfloor\right)$ pixels. For $m = 21$, the resolution is 14×14 pixels.

[9] The details of the finite impulse response (FIR) filter used in this implementation can be found in [101].

5.3.5 SIRT Quality versus Antenna Directivity

This section assesses the effect of a decreasing antenna gain on the quality of SIRT reconstructed images. Table 5.4 summarizes the characteristics of the antennas defined in the FEM model. They are all monopoles with cylindrical parabolic reflectors. They are grouped in three classes, based on their reflector aperture (60, 30 or 15 cm). Within each class, their parameters at each frequency (500 MHz, 1 GHz and 2 GHz) are listed: focal distance, reflector length, isotropic gain, half-power beamwidth (HPBW), front-to-back ratio and the Fraunhofer distance. The Fraunhofer distance provides an approximation for the far-field distance from the transmitting antenna [102]. In the far-field region, an electromagnetic field behaves like a plane wave. The Fraunhofer distance is given by $2L^2/\lambda$, where L is the maximum linear dimension of the antenna [10]

Table 5.4: Antennas parameters.

Ant. Type	D (m)	f (GHz)	p (m)	W (m)	Gain (dBi)	HPBW (degrees)	Front-to-back ratio (dB)	Fraunhofer distance (m)
I	0.6	0.5	0.15	0.60	11.3	36	29.4	3.3
		1	0.08	1.20	14.2	20	30.0	9.6
		2	0.04	2.40	17.2	12	32.1	76.8
II	0.3	0.5	0.15	0.15	8.5	68	22.8	3.3
		1	0.08	0.30	11.3	36	29.1	6.7
		2	0.04	0.60	14.2	20	28.4	13.3
III	0.15	0.5	0.15	0.04	5.8	114	20.9	3.3
		1	0.08	0.08	8.5	68	22.9	6.7
		2	0.04	0.15	11.2	36	29.5	13.3

Fig. 5.14 portrays the quality degradation of the reconstructed images of both floor maps as the antenna gain diminishes from 14.2 dBi (a,d) down to $8,5$ dBi (c,f). The operational frequency was 1 GHz. The deterioration of the reconstructed images is evident. This result was expected, as a lower directivity means that the radiated energy will spread out more, leading to more intense multi-path reception. The trade-off here is between image quality and practicality of antenna deployment on the field: higher gain equals better quality but implies in larger reflectors, which might hinder moving the antennas around the target in certain cases.

Note that such analysis could not be carried out using the path-loss model of Chapter 4, as there the antenna gain was simply a number to be added to the output and received powers and did not model the energy distribution on the plane.

[10] In a 2-D COMSOL model, all surfaces are vertically extruded 1 meter for the calculation of power flows through boundaries [93]. Therefore, L will never be smaller than one meter.

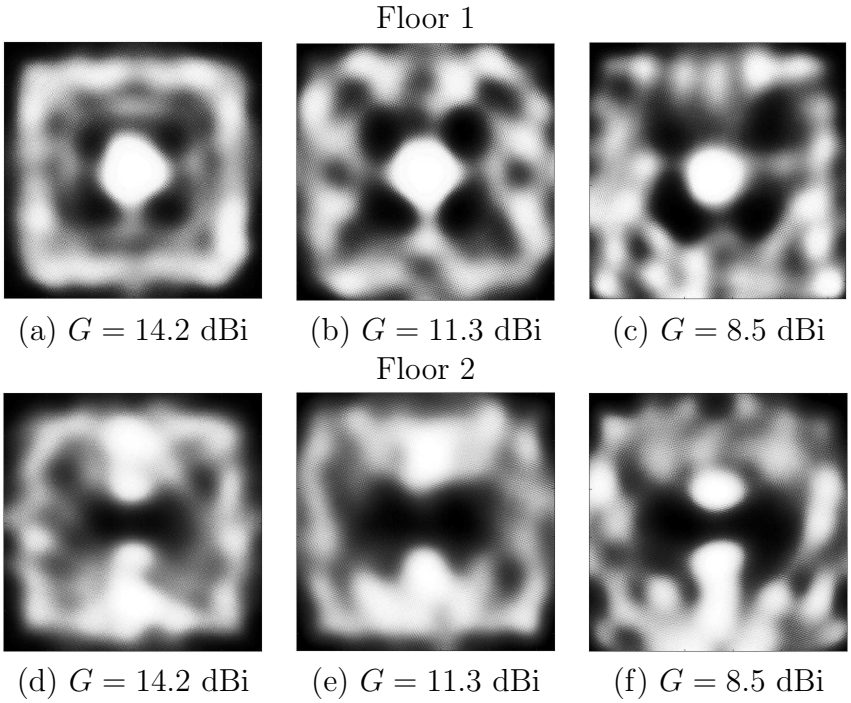

(a) $G = 14.2$ dBi (b) $G = 11.3$ dBi (c) $G = 8.5$ dBi

(d) $G = 14.2$ dBi (e) $G = 11.3$ dBi (f) $G = 8.5$ dBi

Figure 5.14: Degradation of SIRT quality with decreasing antenna directivity ($\Delta\rho = 2\lambda$ with up-sampling, and $n = 40$).

5.3.6 Standard versus Optimized Meshes

Fig. 5.15 compares SIRT using the standard and optimized meshes. It indicates that there is no degradation of the reconstructed images with the use of the optimized mesh. In fact, due to the much higher finite element density at interfaces, narrow regions and corners, the details of the inner obstacles of both floor maps – the column in floor 1 and the inner walls in floor 2 – are reproduced better. These results confirm the advantage of using the optimized mesh, which on average reduces the computational cost by a factor of six (see Section 5.2.4).

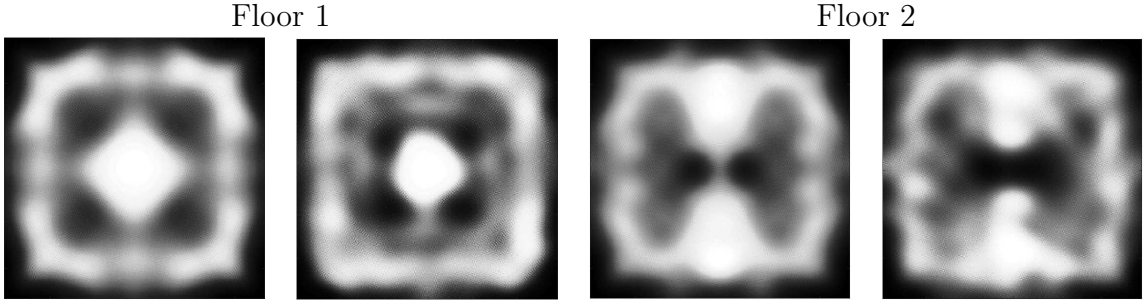

(a) MSSIM= 0.37 (b) MSSIM= 0.41 (c) MSSIM= 0.31 (d) MSSIM= 0.36

Figure 5.15: Comparing SIRT quality using the standard (a,c) and optimized (b,d) meshes ($\Delta\rho = 2\lambda$ with up-sampling, and $n = 40$).

5.3.7 SIRT Quality versus Operational Frequency

At higher frequencies, the lower wavelength is expected to result in higher quality reconstructed images, as the propagating energy will approach more the ray-like properties on which all the reconstruction methods are based upon (as they were all originally designed for X-ray CTI reconstruction). Besides that, for the same antenna aperture D, the antenna gain will be higher at higher frequencies. Fig. 5.16 shows the far-field radiation patterns of antenna type I ($D = 60$ cm) at three different frequencies (500 MHz, 1 GHz and 2 GHz). Table 5.4 informs that the isotropic gains are 11.3, 14.2 and 17.2 dBi, respectively (i.e., the gain approximately doubles with frequency).

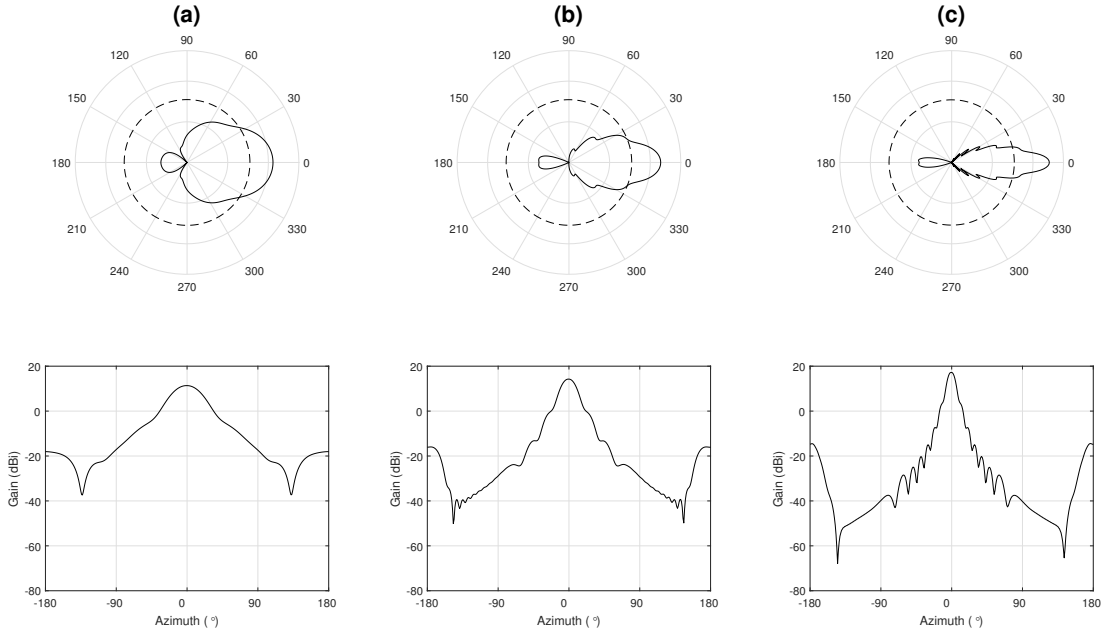

Figure 5.16: Antenna type I - radiation patterns at (a) 500 MHz, (b) 1 GHz and (c) 2 GHz.

Fig. 5.17 brings the SIRT reconstruction of floor map 1 at the selected frequencies. Though at 1 GHz there is a clear improvement in the recovered details of the central obstacle (which practically occupies the whole floor at the 500 MHz reconstructed image), SIRT quality decreased at 2 GHz in respect to 1 GHz. This result goes against the reasoning laid out in the previous paragraph.

Upon closer inspection of Table 5.4, a possible explanation to such anomaly arises. At 2 GHz, the Fraunhofer distance for antenna I is 76.8 meters, which is way larger then the 14.91-m transmitter-receiver distance. Therefore, the measurements are being made in the near field region, where the radiation pattern shown in Fig. 5.16c does not apply. To verify that, we carried out the reconstruction using the lower gain antenna type III ($D = 15$ cm). In such case, the far-field distance

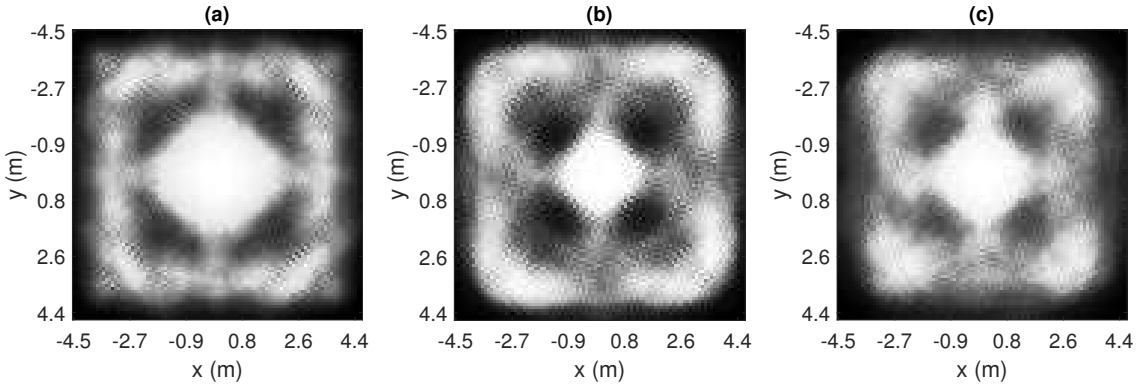

Figure 5.17: SIRT reconstructed floor map 1 using antenna type I at (a) 500 MHz (a), (b) 1 GHz and (c) 2 GHz, with $\Delta\rho = 9$ cm and $n = 40$. A 2-D median filter is applied to the sinogram, as described in Section 5.3.3.

at 2 GHz will be 13.3 m, which is shorter than the transmitter-receiver distance. Fig. 5.18 depicts the far-field radiation patterns of antenna type III at the three selected frequencies.

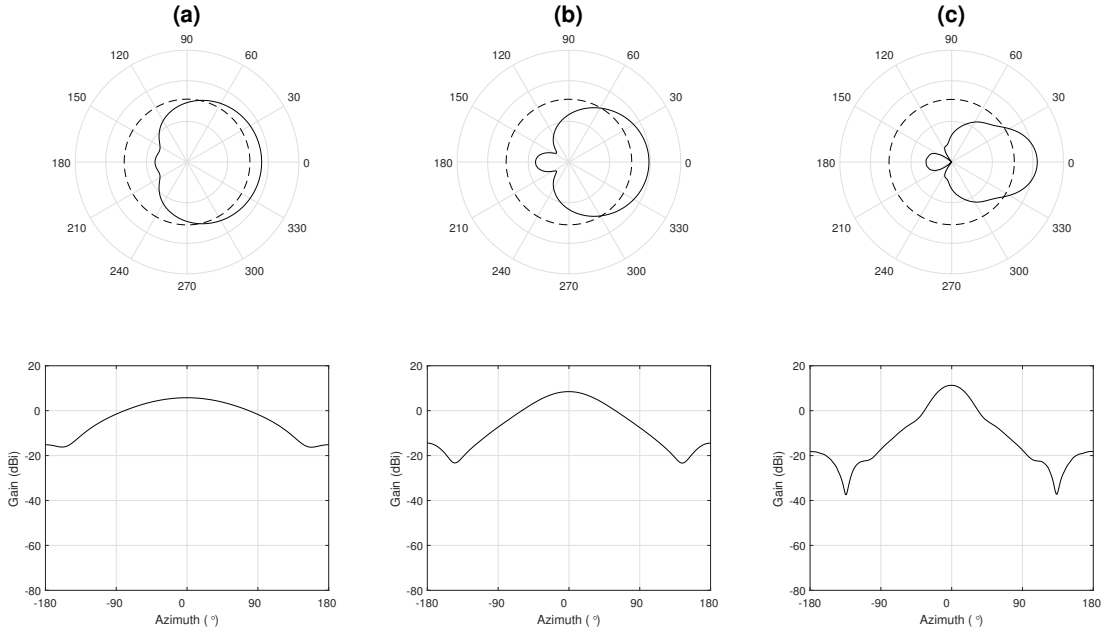

Figure 5.18: Antenna type III - radiation patterns at (a) 500 MHz, (b) 1 GHz and (c) 2 GHz.

Fig. 5.19 shows the SIRT reconstructed images of floor maps 1 and 2 at the three selected frequencies using antenna type III. Now the quality enhancement at 2 GHz becomes evident. The outer walls are recovered with much finer detail. Note

that the inner walls in floor map 2 are also reconstructed with higher quality. This confirms the initial expectations.

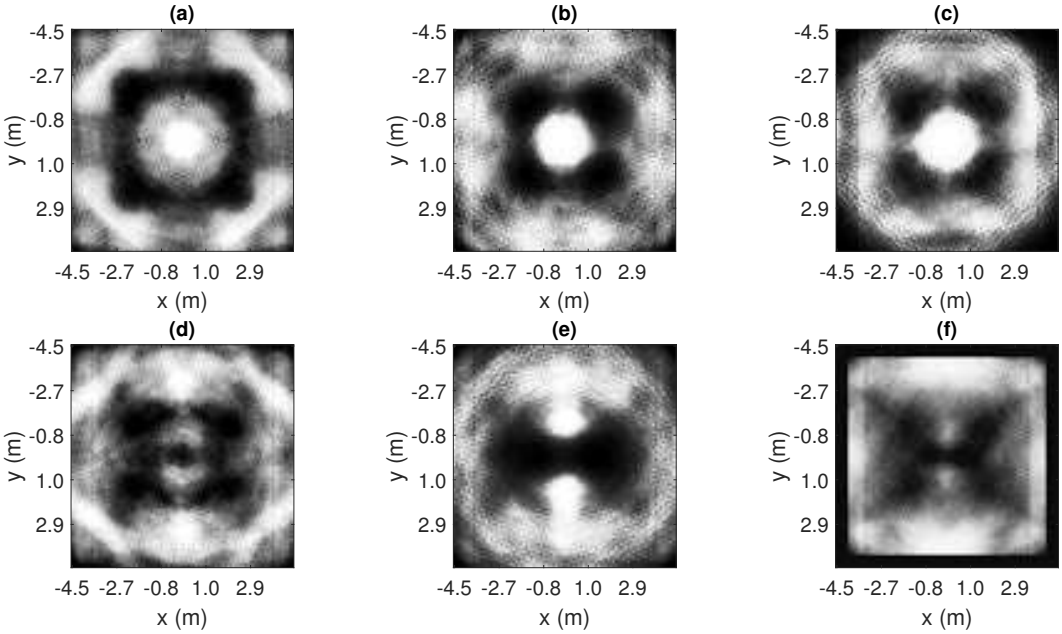

Figure 5.19: SIRT reconstructed floor maps 1 (a,b,c) and 2 (d,e,f) using antenna type III at 500 MHz (a,d), 1 GHz (b,e) and 2 GHz (c,f), with $\Delta\rho = 9$ cm and $n = 40$. A 2-D median filter is applied to the sinogram, as described in Section 5.3.3.

However, there is a trade-off between reconstruction quality and practicality of the deployment of the experimental set-up. At higher frequencies, receivers with higher sensitivity, transmitters with more output power and higher gain antennas are required, as the propagation losses – particularly the through-the-wall attenuation – will be much more intense, as Table 5.1 indicates and Fig. 5.20 shows. Depending on the set-up configuration and on the floor being mapped (on its size, walls width and materials), reconstruction might be possible only at lower frequencies. In such case, the choice might be between obtaining a lower quality image or obtaining no image at all.

5.3.8 Post-Processing of Reconstructed Images

Post-processing techniques can be applied to the reconstructed floor maps to enhance image quality before forwarding them to an application or an human observer. This section shows the results of employing segmentation (thresholding) followed by a morphological operation (erosion).

Thresholding is an easy procedure when the image luminance histogram is clearly bimodal. Within the scope of post-processing of the reconstructed TWM images, thresholding will be difficult, because the reconstructed images histograms

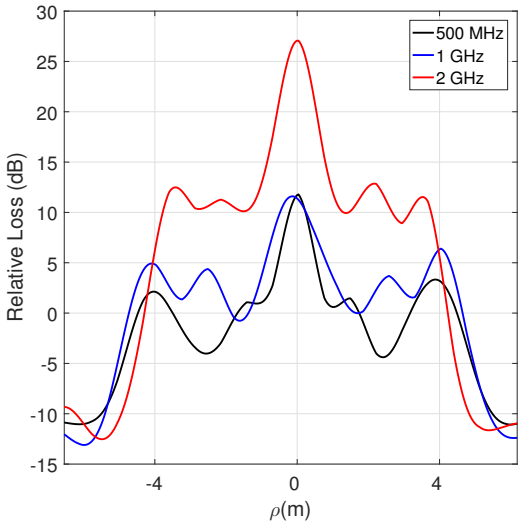

Figure 5.20: Radon projections from floor map 1 taken at $\theta = 0$ degrees with $\Delta\rho = 60$ cm. Though the relative losses at 500 MHz and 1 GHz are similar, at 2 GHz it increases significantly.

are multi-modal, as Fig. 5.21 illustrates. Ideally, the image segmentation should be autonomous and non-parametric, aiming at future TWM applications where the recovered image shall be processed and interpreted by an automaton. The automaton could then use the post-processed recovered floor map to define an optimum route before entering the floor. In such scenario, the reconstructed floor map, after post-processing, would be simply an occupancy grid, an array of zeros and ones, with non-null pixels indicating the presence of an obstacle [77].

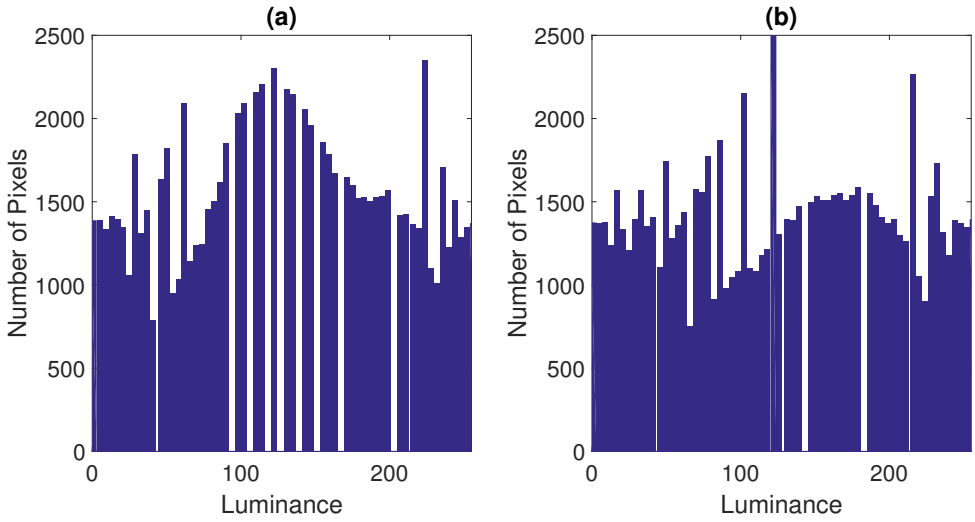

Figure 5.21: Luminance histograms of SIRT reconstructed floor maps (a) 1 and (b) 2.

Among the multitude of available techniques [103], Otsu's thresholding has been

selected. It meets the requirements previously set: being autonomous and non-parametric. It is a point-dependent global thresholding technique that defines a threshold level minimizing the intra-class variance while maximizing the inter-class variance [104]. Though it is not possible to provide a theoretical guarantee that Otsu's method will be the best in any situation, it yielded reasonable results for both floor maps. Entropic thresholding has also been evaluated [105], but with poorer results. More advanced techniques, such as the region-dependent local thresholding applied to automatic boundary detection in radiographic images presented in [106], or the segmentation and edge enhancement with stabilized inverse diffusion equations proposed in [107], could be used to further improve the recovered images. This, however, lies beyond the scope of this work.

Fig. 5.22a,d show the result of applying Otsu's thresholding to the original SIRT reconstructed images, illustrated in Fig. 5.14a,d, respectively. Fig. 5.22b,e depict the segmented images after erosion by a 12-pixel long square structuring element. Fig. 5.22c,f bring the original floor maps for comparison. Though somewhat distorted, the layouts of the floors are still recognizable in the post-processed images.

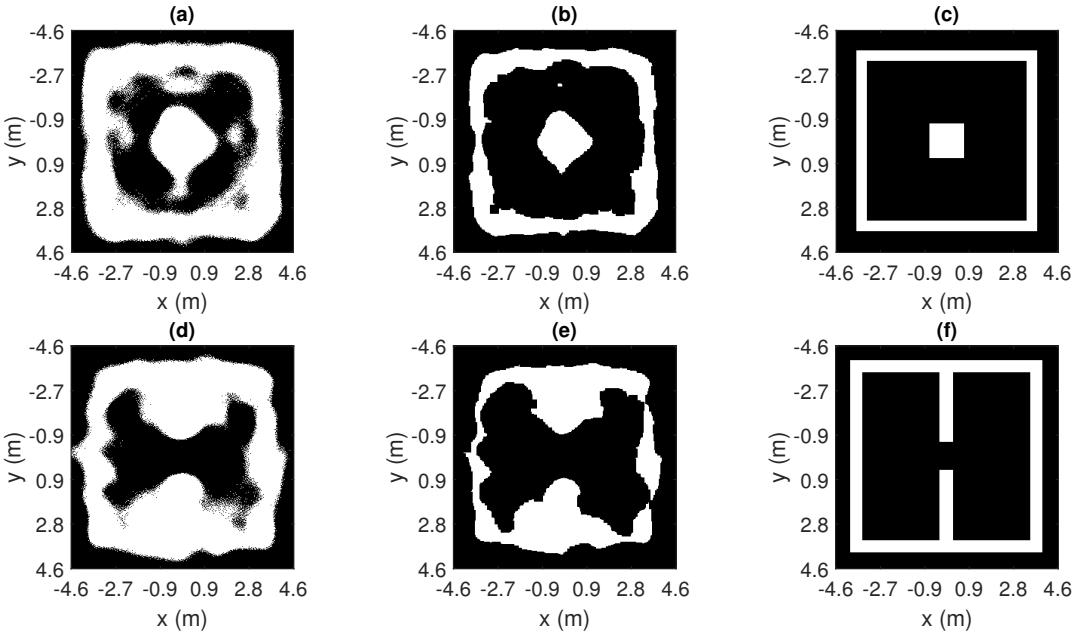

Figure 5.22: Post-processing of SIRT reconstructed maps (a,d): Otsu's thresholding followed by erosion (b,e). The ground-truth signals are shown (c,f) for better comparison ($\Delta\rho = 2\lambda$ with up-sampling, and $n = 40$).

5.4 Conclusions

This chapter defined a FEM-based framework to allow accurate simulations of RF-based TWM using CW signals at selected frequencies in the UHF band. This framework is expected to better represent the RF propagation through materials such as concrete, considering phenomena not accounted for in the simpler path-loss models used in Chapter 4. In fact, as those path-loss models do not account for diffraction nor refraction, there is a large gap between the obtained results and the real world scenario. The FEM framework proposed in this chapter aims at reducing this gap between simulations and measurements.

To fully validate the effectiveness of such framework, field measurements must be carried out under controlled conditions. As we have not been able to proceed to this stage at the present point, we have included measurement results published in [70]. The simple geometry used there is shown in Fig 5.23(a,b). Fig. 5.23d portrays the FBR reconstructed image obtained with the proposed FEM model [11]. Finally, Fig. 5.23e brings the FBR reconstructed image using the model defined in Chapter 4. Clearly, the FEM model yields a reconstructed image closer to the one achieved using field measurements (Fig. 5.23c).

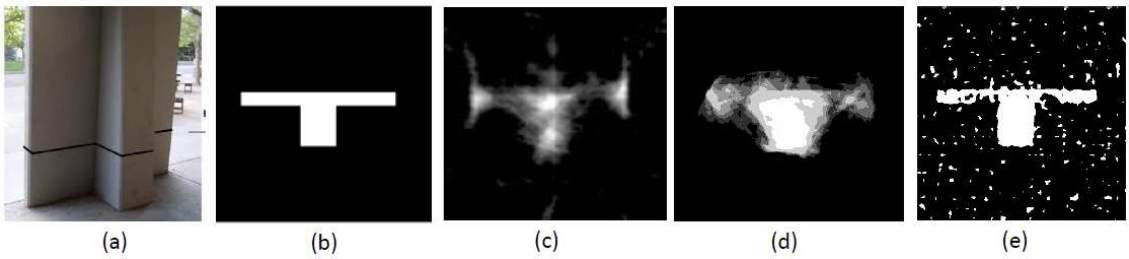

Figure 5.23: (a) T-section concrete column; (b) Column cross-section; (c) FBR reconstructed image from field measurements; (d) FBR reconstructed image using the proposed FEM framework; (d) FBR reconstructed image using the Rayleigh channel path-loss model defined in Chapter 4.

As in Chapter 4, SIRT outperformed all other methods in all evaluated conditions. Then, several experiments were conducted, to better assess the behavior of SIRT under different set of systemic parameters: sampling rates, antenna directivity, and operational frequency (500 MHz, 1 GHz, and 2 GHz). Sinogram low-pass filtering was employed to improve SIRT quality. A simple post-processing procedure, comprising Otsu's thresholding and a morphological operation was used to convert the reconstructed floor map into an occupancy grid to be forward to automatic applications, such as indoor robot navigation.

[11] Using similar configurations as those employed in the actual measurement campaign: antenna gain, sampling rate and operational frequency.

Chapter 6

Multi-Sensor Circular Acquisition Geometry for RF Through-The-Wall Mapping

The reconstruction quality of projective and algebraic methods under different sets of systemic parameters has been evaluated in Chapters 4 and 5. In the former, such evaluation has been carried out using path-loss models corrupted by Rayleigh noise. In the latter, it was accomplished employing the finite-element method (FEM) framework with optimized meshing proposed in this work. Another aspect of paramount importance which must be dealt with is the need to obtain the reconstructed floor maps quickly. Its relevance stands out if one considers the intended applications of RF-based TWM (already discussed in Chapter 4), such as rescuing efforts in collapsed buildings and hostage situations. A first approach to this problem would consider reducing processing time. However, this is negligible if compared to the time required to obtain the RF samples in a parallel-beam geometry. This chapter addresses this issue by proposing a multi-sensor circular acquisition geometry (MCG), which is expected to reduce acquisition time and enable the detection of floor layout changes (e.g., the opening and closing of a door).

6.1 Introduction

In a parallel-beam geometry, two mobile sensors (one transmitter and one receiver) move around the area being mapped to collect the RF samples. In such a geometry with $L = 12.5$ meters (as in Chapter 5) and $\Delta\theta = \pi/10$ radians, both the transmitter and the receiver would have to traverse more than 125 meters to reconstruct the floor map. As a result, any dynamic layout changes occurred in the meantime (e.g., opening and closing a door) will pass unnoticed. On the other hand, in MCG, a

multiple-sensor chain is set up around the area to be mapped. Once deployed, these sensors will remain static for the duration of the mapping process. Such a scheme would allow a much faster reconstruction, as well as the detection of floor layout modifications. However, the use of multiple sensors rises some specific operational issues, such as

- **radio channel multiple access coordination**: some form of multiple access scheme must be adopted, such as frequency division multiple access (FDMA) or time division multiple access (TDMA); in the former, each sensor is allocated a narrow band channel; in the latter, a time slot is assigned to each sensor in a round-robin fashion; code division multiple access (CDMA) is an alternative more suitable for a wideband scenario, which is not considered at this point; in any case, a central node with coordination functions must be set up;
- **sensors positioning and antenna orientation**: with multiple sensors, the effect of positioning errors might compound and degrade reconstruction quality; therefore, high accuracy localization techniques must be employed;

Nonetheless, such practical issues are not addressed at this point. The remainder of the chapter is organized as follows: Section 6.2 specifies the MCG geometric parameters and compares the number of valid rays per pixel it achieves to a parallel-beam geometry and to another published multi-sensor acquisition scheme [7]; Section 6.3 brings the SIRT simulation results using both the path-loss model defined in Chapter 4 and the FEM framework presented in Chapter 5. Finally, Section 6.4 brings a brief conclusion.

6.2 MCG Definition

6.2.1 Geometric Parameters

In MCG, N equally spaced sensors are placed in an outdoor circle around the area to be mapped, which is represented in Fig. 6.1 by a $D \times D$ m^2 square. This square and the sensor chain are concentric. All sensors' directive antennas are pointed towards the common center, located at coordinates (x_0, y_o). The angular separation between adjacent sensors in the sensor chain is defined by $\Delta\xi = \frac{2\pi}{N}$. The ith sensor position vector $\vec{\mathbf{s}}_i = (x_i, y_i)$ components are given by

$$x_i = x_0 + \mathrm{R}\sin\xi_i \tag{6.1}$$

$$y_i = y_0 - \mathrm{R}\cos\xi_i \tag{6.2}$$

where ξ_i is the angle between the negative y-axis and the line connecting the ith sensor to the origin, $i = 1, \ldots, N$, and R is the MCG radius. This parameter is defined as a function of the size of the square-shaped area to be mapped (D), plus an additional distance (δ) to account for the antenna reflector size, thereby preventing it from being too close to the floor outer walls (which would result in deformities in the horizontal radiation patterns). So, the radius can be defined as

$$\mathrm{R} = \frac{\mathrm{D}\sqrt{2}}{2} + \delta \tag{6.3}$$

Parameter δ must be defined as a function of the antenna reflector size and radiation wavelength. As a rule of thumb, higher gains (i.e., larger reflectors) and larger wavelengths demand a bigger δ. This relationship, however, is not explored at this point. So, a reasonable value for δ will be assumed and used in all simulations.

The trajectory of the ray $r_{i,j}$ transmitted by sensor i and received at sensor j is defined by a linear equation with coefficients $[a_{i,j}\ b_{i,j}]^{\mathrm{T}}$. The angular and linear coefficients of $r_{i,j}$ ($i = 1, \ldots, (N-1)$; $j = i+1, \ldots, N$) are given by, respectively,

$$a_{i,j} = \frac{(\cos x_i - \cos x_j)}{(\sin x_j - \sin x_i)} \tag{6.4}$$

$$b_{i,j} = \frac{(y_0 - \mathrm{R}\cos x_j)(\sin x_j - \sin x_i) - (y_0 + \mathrm{R}\sin x_j)(\cos x_i - \cos x_j)}{(\sin x_j - \sin x_i)} \tag{6.5}$$

Only the rays traversing the area to me mapped are of interest in RF-based TWM. In Fig. 6.1, the region to be mapped is delimited by vertexes P_1, P_2, P_3 and P_4. Therefore, only the rays intercepting the boundaries of this square are selected, i.e., just the rays $r_{i,j}$ belonging to set $\mathcal{A}$ defined by

$$\mathcal{A} = \left\{ i, j \mid \exists k \in \{1,2,3,4\},\ r_{i,j} \cap \overline{P_{v(k)}P_{v(k+1)}} \neq \oslash,\ v = [1\ 2\ 3\ 4\ 1] \right\} \tag{6.6}$$

Fig. 6.2 shows the valid rays in a MCG sensor chain with $N = 18$ and $R = 6.8$ m. The boundaries of the area to be mapped are defined by a square of size $D = 9.2$ m, so $\delta = \lambda = 30$ cm.

Unlike the parallel-beam acquisition geometry, where the sensors directive antennas are always aligned, the antennas in MCG are all pointed to (x_0, y_0). Therefore, one must apply the antenna horizontal mask to obtain the effective isotropic radiated power in the direction of interest, i.e., towards the receiving sensor. To do that, the angle between any given ray and the direction of maximum gain of the transmitting sensor must be calculated. From Fig. 6.1, such angle, for ray $r_{i,j}$, is

defined by

$$\theta_{i,j} = \arccos\left[\frac{-\vec{\mathbf{s}}_i \cdot (\vec{\mathbf{s}}_j - \vec{\mathbf{s}}_i)}{\|\vec{\mathbf{s}}_i\| \, \|\vec{\mathbf{s}}_j - \vec{\mathbf{s}}_i\|}\right] \tag{6.7}$$

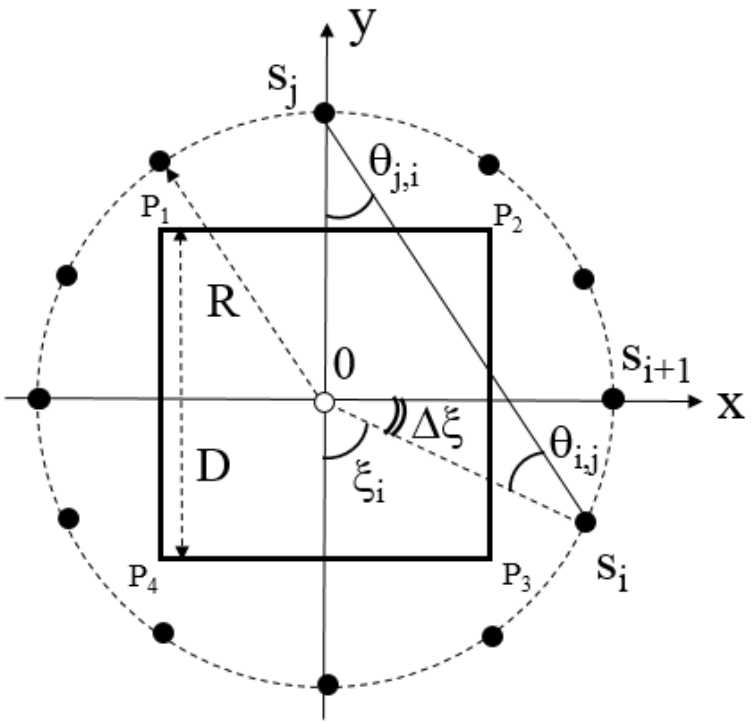

Figure 6.1: MCG parameters definition.

6.2.2 Number of Rays per Pixel

As a rule of thumb, for any given reconstruction method, keeping all other systemic parameters unchanged, increasing the number of rays per pixel improves the reconstructed image quality. Fig. 6.3 indicates that in a setup with approximately 2000 valid rays, the average number of rays per pixel is roughly 3.4 times higher in the parallel-beam geometry (44 rays/pixel) in comparison to MCG (13 rays/pixel). However, MCG is not expected to yield reconstructed images with better quality than in a parallel-beam geometry. Instead, it is intended to drastically reduce the acquisition time and enable dynamic detection of floor layout changes. So, as long as acceptable reconstruction quality is achieved, MCG usefulness will be established. This will be verified in Section 6.3.

Nonetheless, compared to the multi-sensor acquisition scheme proposed in [7], MCG achieves an average number of rays per pixel approximately 20% higher (13 against 11). As the cumulative distribution function (CDF) in Fig. 6.4b indicates, 50% of the pixels in MCG are crossed by at least 13 rays. In the acquisition geometry

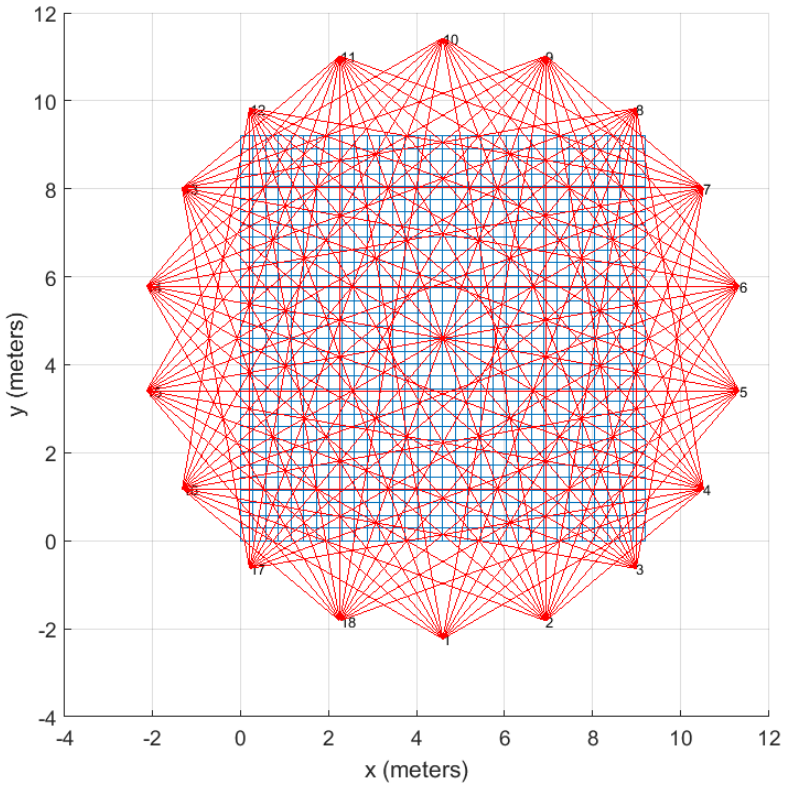

Figure 6.2: Valid rays in a MCG with 18 sensors.

formulated in [7], practically 100% of the pixels are crossed by less than 13 rays [1].

6.3 MCG SIRT

In this section, SIRT is applied using samples obtained from a MCG sensor chain placed around floor map 2 (see Fig. 4.7b), using the Rayleigh channel path-loss model defined in Chapter 4 and the FEM framework specified in Chapter 5. The changes required to accommodate MCG characteristics, as well as the achieved results, are presented hereafter. In all following simulations, the MCG radius is assumed to be R = 6.8 meters. The operational frequency is 1 GHz.

6.3.1 Rayleigh Channel Path-loss Model

Adapting the Channel Model Equations to MCG

Equation (4.18) defines the path-loss equation used in Chapter 4, still without the random term to account for static multipath fading. This equation must be modified to fit into the MCG model. Referring to the MCG depicted in Fig. 6.1, one has the

[1]For the comparison, it was assumed that $N = 78$ sensors and that the length of the square sensor chain in [7] is $2R/\sqrt{2}$, where R is the radius of the MCG circle.

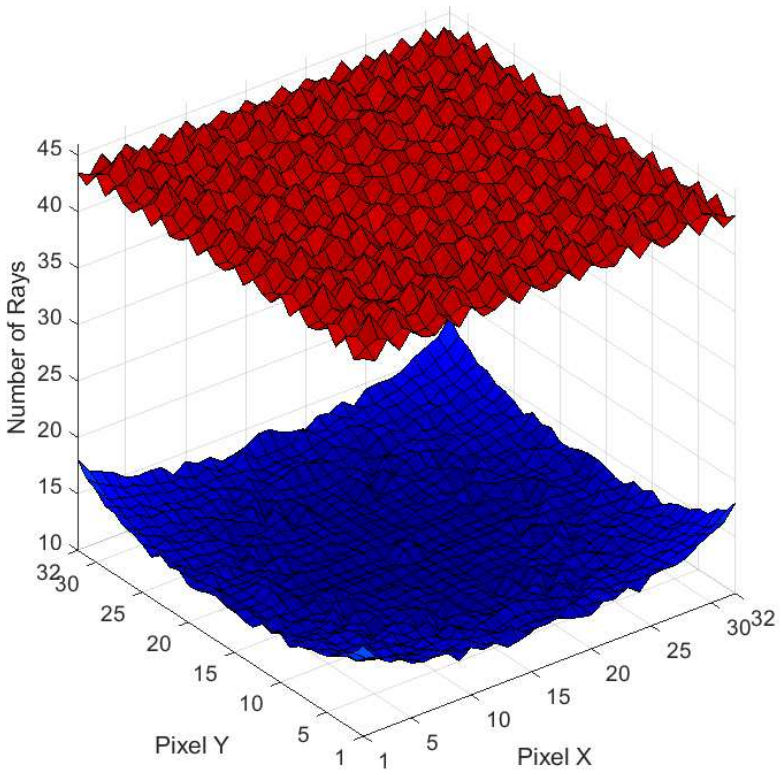

Figure 6.3: Number of rays crossing each pixel in a parallel-beam acquisition geometry ($L = 12.51$ meters, $\Delta\rho = 6$ cm, $\Delta\theta = \pi/10$ radians) (red) and in MCG ($N = 78$ sensors) (blue). In both cases there are approximately 2000 rays and the reconstructed image resolution is 32×32 pixels.

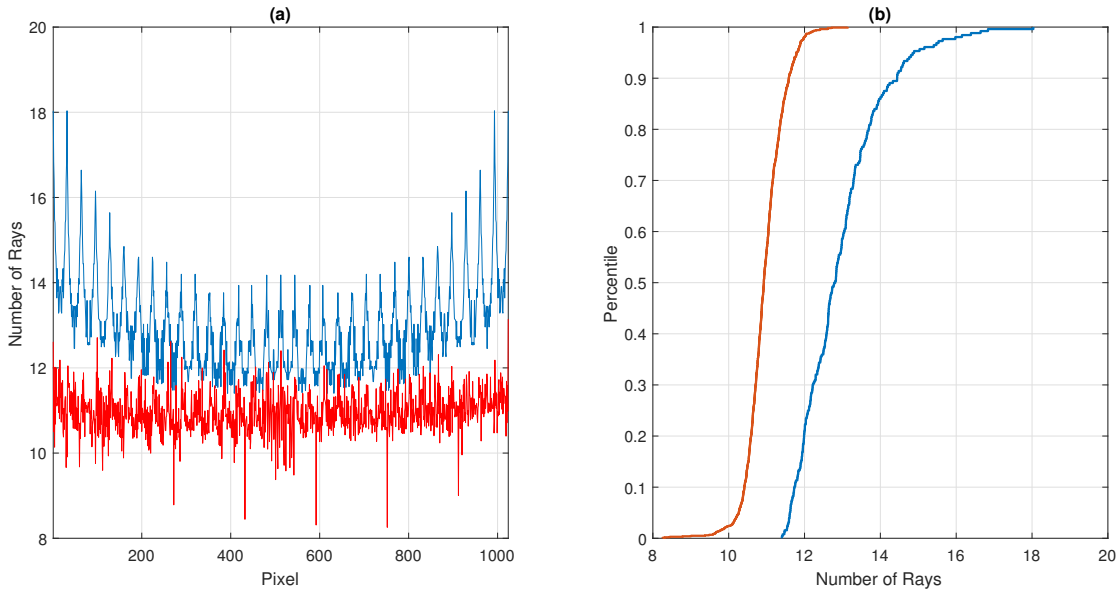

Figure 6.4: (a) Number of rays per pixel and (b) CDF of the number of rays per pixel for MCG (blue) and square [7] (red) geometries with 78 sensors.

following equation describing the mean received power P_r (dBm) at $d_{i,j}$ meters from the transmitter along the ray defined by $r_{i,j}$, $i = 1, \ldots, N-1$ and $j = i+1, \ldots, N$:

$$P_r(i,j) = P_t - L_t + G_t - H_t(\theta_{i,j}) - L_{d_{i,j}} - \sum_k \alpha_k(i,j) l_k(i,j) + G_r - H_r(\theta_{j,i}) - L_r \quad (6.8)$$

where $l_k(i,j)$ and $\alpha_k(i,j)$ are the length (meters) and the attenuation factor (dB/m) across the kth obstacle (along the line connecting the ith and jth sensors), respectively. P_t (dBm) is the mean transmitted power. L_t and L_r are the losses (dB) due to cables and connections at the transmitter and receiver, correspondingly. G_t and G_r are the transmitter and receiver antennas gains (dBi), in that order, in the direction of maximum irradiation ($\theta = 0$ degrees in the antenna radiation pattern). $L_{d_{i,j}}$ is the propagation loss (dB) as a function of the transmitter-receiver distance $d_{i,j}$, i.e., the separation between the ith and the jth sensors. Note that, as in MCG the sensors antennas are not aligned, the antenna mask losses (due to the horizontal radiation patterns) must be taken into account. This is done by adding the mask losses $H_t(\theta_{i,j})$ and $H_r(\theta_{j,i})$ at the transmitter and receiver sensors, respectively. However, if only one type of antenna is used, one has that $H_t(\theta_{i,j}) = H_r(\theta_{j,i})$, as, from Fig. 6.1, it is clear that $\theta_{i,j} = \theta_{j,i}$. Equation (6.8) then becomes:

$$P_r(i,j) = P_t - L_t + G_t - L_{d_{i,j}} - \sum_k \alpha_k(i,j) l_k(i,j) + G_r - L_r - 2H_t(\theta_{i,j}) \quad (6.9)$$

The last term in equation (6.9) must also be added to equation (4.30), which defines the Rayleigh distribution parameter b, and to equation (4.31), which specifies the sinogram matrix forwarded to the reconstruction method. These equations then become, respectively:

$$b = \frac{1}{2}\sqrt{10^{\left[0.1\left(P_t - L_t + G_t - L_{d_{i,j}} + G_r - L_r - 2H_t(\theta_{i,j})\right)\right]}} \quad (6.10)$$

and

$$\mathbf{G} = \left[\text{EIRP} - G_r + L_r - P_r(i,j) - 2H_t(\theta_{i,j})\right]_{i=1,\ldots,N-1; j=i+1,\ldots,N} \quad (6.11)$$

where N is the the number of sensors in the MCG chain and EIRP is the effective isotropic radiated power (dBm), defined by equation (4.24).

Simulation Results

Fig. 6.5 brings the MCG SIRT reconstructed maps with 18, 39 and 78 sensors in the MCG chain, which correspond to angular separations $\Delta\xi = 10, 4.6$ and 2.3 degrees, respectively. The antenna gains, transmitter and receiver losses and receiver

sensitivity use the same values defined in Section 4.4.

The first reconstructed map (Fig. 6.5a) is significantly corrupted by undersampling artifacts, though the outer walls are still clearly distinguishable. The inner walls are harder to interpret, but the central door is perceivable. However, Fig. 6.5b indicates that with 39 sensors the reconstructed map reproduces quite well the main features of the original floor map. As Fig. 6.5c shows, doubling the number of sensors from 39 to 78 produces just a small improvement in the reconstructed image quality.

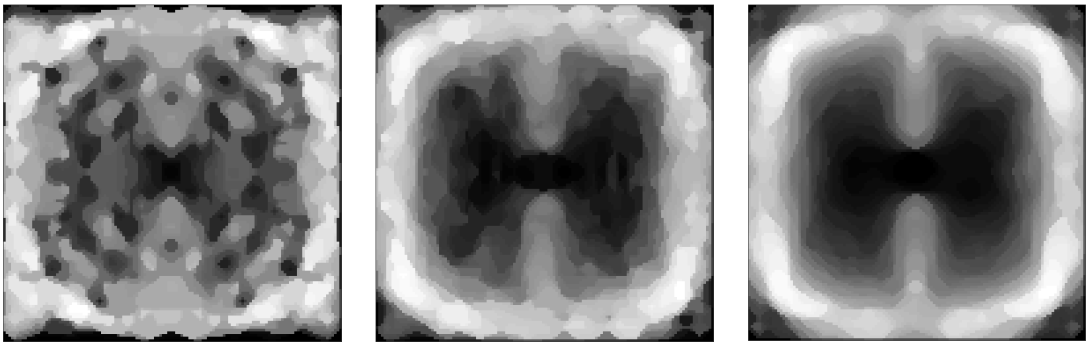

(a) 18 sensors (b) 39 sensors (c) 78 sensors

Figure 6.5: MCG SIRT reconstruction simulation with the Rayleigh channel pathloss model. The reconstructed maps resolution is 32×32 pixels.

As expected, the SIRT reconstructed floor maps using a parallel-beam acquisition geometry (see Figs. 4.13h and 4.14h) have a better quality. Nevertheless, the MCG SIRT images clearly reproduce the floor main features. This results must be further validated using the more sophisticated FEM model.

6.3.2 FEM Model

Adapting the Model to MCG

The MCG FEM model uses the same configuration parameters defined in Sections 5.2.1 to 5.2.4. However, instead of employing just two sensors whose movements would be simulated during the parametric sweep, up to 78 concentric fixed sensors are placed around the area to be mapped. Each sensor acts as both a transmitter and a receiver, though not simultaneously. Due to limitations in the simulation of simultaneous transmission by multiple sensors, the field source is activated upon each monopole by setting up a surface current density with angular frequency $2\pi \times 10^9$ rad/sec, as specified in Section 5.2.2 in a round-robin fashion.

In the geometry representing the floor map in the FEM model, a bulkhead is added to simulate barricading of the central door. Fig. 6.6 shows it in blue. The

bulkhead is assumed to be made of stainless steel, with $\sigma = 4.032 \times 10^6$ S/m, $\mu_r = 1$ and $\epsilon_r = 1$ [108] at 1 GHz. All sensors employ antenna type III (see Tab. 5.4).

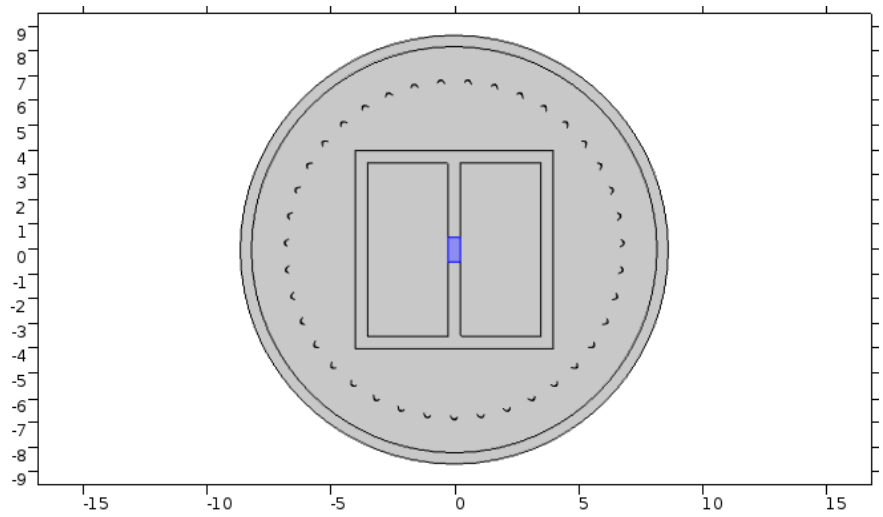

Figure 6.6: MCG geometry in COMSOL with 78 sensors with directive antennas. All distances are expressed in meters.

Simulation Results

Fig. 6.7 brings the MCG SIRT reconstructed floor maps with 39 and 78 sensors. The ground-truth signal (the original floor map) is superimposed over the MCG SIRT image for better comparison in Figs. 6.7b,d. Though heavily corrupted by undersampling, MCG SIRT reconstruction with 39 sensors yields a floor map where both the outer walls and the central door are discernible. Unlike the simulation using the Rayleigh channel path-loss model, here the reconstruction quality significantly improves when doubling the number of sensors in the MCG chain from 39 to 78. The reconstruction quality is worse than the one achieved with the parallel-beam geometry, but the reconstructed maps still clearly reproduce the main features of the original floor map.

Once deployed, the MCG sensor chain can map the area of interest without further displacements of the sensors and therefore is capable of detecting changes in the floor layout, e.g., the opening and closing of a door. To illustrate that, the previously defined steel bulkhead is inserted in the 2-D FEM model. Fig. 6.8a and Fig. 6.8b show the MCG SIRT reconstruction without and with the bulkhead. Fig. 6.8c displays the absolute difference of these two previous images. Due to the high intensity of reflected components at the barricade highly conductive surface, the differential map shows high intensity levels not only at the bulkhead location, but also at walls directly opposed to both sides of the bulkhead. Fig. 6.8d brings the binary image obtained applying a threshold filter to Fig. 6.8c. Any luminance level

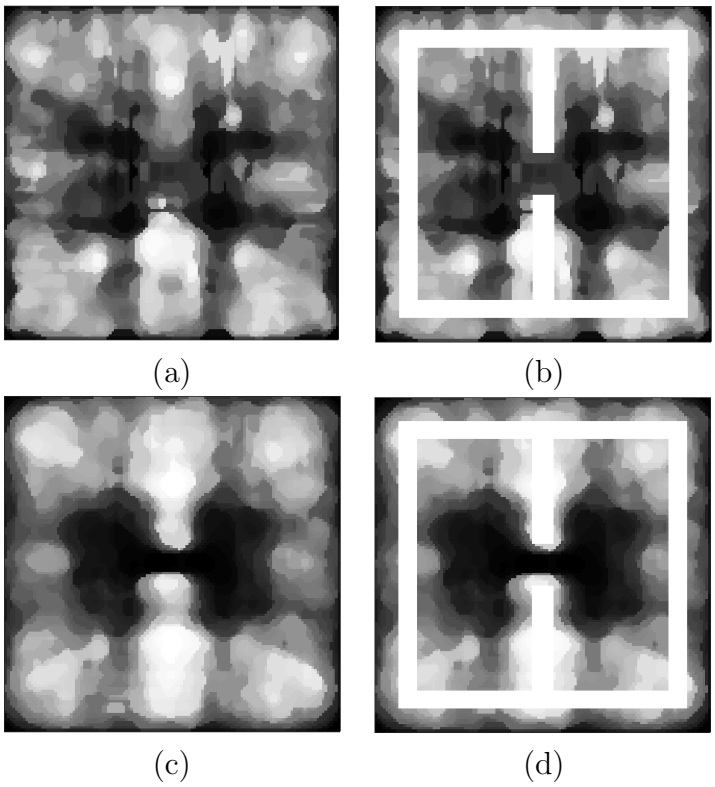

Figure 6.7: MCG SIRT reconstruction simulation using the FEM model with 39 (a,b) and 78 (c,d) sensors. The reconstructed maps resolution is 32×32 pixels. Histogram equalization and median filtering have been applied to the reconstructed images.

below 3 dB of the peak was set to zero. After thresholding, the output image was eroded using a disk structuring element with radius 2. The door barricading is easily detected, mostly due to the high conductivity of the bulkhead material (stainless steel).

6.4 Conclusions

This chapter defined a multi-sensor circular acquisition geometry (MCG) intended to speed-up the sample collection phase in comparison to the standard parallel-beam geometry. MCG deploys a chain of concentric sensors, that, once in place, remains static. A medium access control must be enforced and a highly precise location of the sensors is demanded for proper operation. The proposal was evaluated using both the Rayleigh channel path-loss model and the FEM-based framework. The MCG SIRT recovered images quality was worse than the ones achieved using SIRT within a parallel-beam geometry, due to the lower number of rays per pixel in MCG. Nonetheless, the reconstructed quality was still acceptable, allowing identification of the main features of the original floor map. This, coupled with the faster sample acquisition provided by MCG and its ability to dynamically detect floor layout

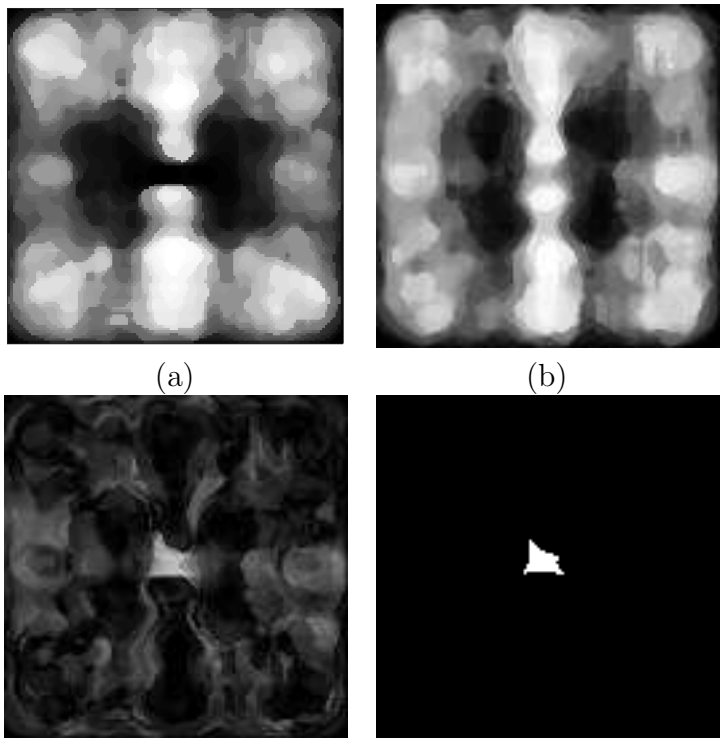

Figure 6.8: Door barricading detection in MCG SIRT reconstruction simulation using the FEM model with 78 sensors. The reconstructed maps resolution is 32×32 pixels. Histogram equalization and median filtering have been applied to the reconstructed images: (a) SIRT reconstructed image of floor map 1; (b) SIRT reconstructed image of floor map 1 with the stainless steel bulkhead; (c) differential image of (b) and (a); (d) result of applying a threshold filter to (c).

changes, suggests the usefulness of the proposed acquisition scheme.

Chapter 7

Conclusions and Future Directions

7.1 Conclusions

This work investigates two main problems: RF-based multi-floor indoor positioning and RF-based non-invasive static obstacles mapping. The first is typically related to non-critical location-based commercial applications, while the second is intrinsically connected to critical scenarios, such as rescue operations in collapsed buildings, hostage situations or urban military operations. Nonetheless, both problems are interrelated, in the sense that both can augment situational awareness in indoor environments.

From an extensive literature review, it became evident that multi-floor positioning papers were much less abundant than the ones addressing solely positioning on a single floor, justifying exploring and trying to propose improvements to multi-floor positioning. The first part of the thesis, comprising Chapter 2 and 3 focuses on the positioning of mobile WiFi nodes in multi-floor indoor environments. A target radio frequency (RF) fingerprint – measured by the MS to be localized – is compared with georeferenced RF fingerprints, previously stored in a correlation database (CDB). Therefore, this strategy lies within the so-called Database Correlation Methods (DCM) used to locate mobile stations (MS) in wireless networks. To obtain best matches in terms of architectural structures such as floors, doors, aisles, among others, we applied two combined techniques that improve localization accuracy: unsupervised clustering (K-medians and Kohonen layer) and majority voting committees of backpropagation artificial neural networks (ANNs). The unsupervised clustering is employed to allow collected data (the fingerprints) to group freely in their natural space, without precluding – through the imposition of architectural constraints – any natural arrangement of the collected fingerprints. The proposed combined strategy improves floor identification accuracy, which in indoor multi-floor positioning must be high. The effects of the proposed solution on the DCM posi-

tioning accuracy are experimentally evaluated using actual measured data. In the trial the floor identification accuracy ranged from 91% to 97%, and the average 2-D positioning error ranged from 3.5 to 1.1 m, depending on the size of the measurement window (from 1 to 25 samples).

The second part of the thesis, comprising Chapters 4, 5 and 6, explored radio-tomographic imaging, also referred to as RF-based through-the-wall mapping (TWM). RF-based TWM is a viable alternative for non-invasive (i.e., without direct sensing) mapping of static obstacles. The thesis first evaluated four different reconstruction algorithms under a parallel-beam acquisition geometry, originally applied in first-generation computerized tomographic imaging: two projective methods (Filtered Backprojection Reconstruction and Direct Fourier Reconstruction), both of them based on the Fourier Slice Theorem; and two algebraic methods (Algebraic Reconstruction Technique and Simultaneous Iterative Reconstruction Technique), both with regularization properties expected to improve reconstruction quality. Initially, evaluation was carried out using a path-loss model with a Rayleigh random component to account for multi-path reception. Recognizing the need for a more accurate model, particularly one that adequately takes into account the wave nature of the propagating energy, we proposed using a finite element method (FEM) in the TWM simulations. To improve accuracy and reduce processing time, the meshing options of the FEM model were optimized, based on some physical constraints. Finally, the multi-sensor circular acquisition geometry (MCG) was defined, which is expected to reduce sample collection time (in comparison to the parallel-beam geometry) and enable the dynamic detection of floor layout changes, e.g., the opening and closing of a door. The proposal was validated using the FEM framework.

7.2 Future Directions

Future developments for the first part could address some substantial issues for the practical implementation of an RF-based multi-floor positioning system, such as:

- **techniques to mitigate cross-device effect**: i.e., increase positioning accuracy when locating mobile devices with different hardware (WiFi adapters) than the ones used in the off-line (training) phase; cross-device effect degrades positioning accuracy of any DCM method, and therefore mitigating this impairment is quite useful [109];

- **alternatives for cooperative CDB filling and updating**: one of the critical issues in any DCM system is the maintenance of the CDB; this is performed in the off-line or training phase, but ideally the very system users could

cooperatively help to furnish the CDB with up-to-date RF fingerprints [64];

Regarding the second part, future directions might comprise:

- **building a 3-D FEM model in COMSOL**: running the RF-based TWM FEM simulations employing a 3-D model shall demand a much higher computational capacity than the one needed to run the 2-D simulations used in this thesis; nonetheless, 3-D models will produce more realistic results;
- **use of ultra-wide band (UWB) signals to improve reconstruction quality**: the high temporal resolution of UWB signals might enable suppressing multi-path components, thereby achieving better reconstruction quality [8]; a FEM model could be set up, and both time and frequency domain analysis could be carried out using it to evaluate how the use of UWB signals would improve the quality of different reconstruction algorithms under different scenarios (floor maps, sampling rates, antenna models, acquisition geometries, etc.).
- **multi-frequency reconstruction**: combining samples of different frequencies to improve reconstruction quality when projection clipping (e.g., due to receiver sensitivity limitations) occurs – higher frequencies shall be preferable (due to the lower intensity of diffracted components) whenever available; if not, increasingly higher wavelengths are selected (due to the lower through-the-wall loss);
- **evaluation of reconstruction quality degradation due to sensors positioning errors in MCG TWM**: the effect of positioning errors in the reconstruction quality of TWM using a parallel-beam geometry and a projective reconstruction algorithm (Filtered Backprojection Reconstruction) has been evaluated in [110]; a similar analysis could be conducted in MCG when using algebraic reconstruction methods;
- **exploring alternatives to enhance sensors positioning accuracy in MCG**: the sensors in the MCG chain must be GPS-enabled, but probably even GPS positioning accuracy in an urban environment will not be enough for proper system operation; alternatives such as creating an *ad hoc* differential GPS (D-GPS) cell must be investigated (within the context of Mobile ad hoc networking (MANETs) [111]);
- **further validation of the RF-based TWM FEM framework through field measurements**: extensive measurements have been collected to validate the proposal of the first part of the thesis; doing the same for the second part would be desirable;

Bibliography

[1] BILL, R., CAP, C., KOFAHL, M., et al. "Indoor and outdoor positioning in mobile environments - a review and some investigations on WLAN-positioning", *Geographic Information Sciences*, v. 10, n. 2, 2004.

[2] LIU, H., DARABI, H., BANERJEE, P., et al. "Survey of Wireless Indoor Positioning Techniques and Systems", *IEEE Transactions on Systems, Man, and Cybernetics, Part C: Applications and Reviews*, v. 37, n. 6, pp. 1067–1080, 2007.

[3] LAOUDIAS, C., CONSTANTINOU, G., CONSTANTINIDES, M., et al. "The Airplace indoor positioning platform for Android smartphones". In: *Mobile Data Management (MDM), 2012 IEEE 13th International Conference on*, pp. 312–315. IEEE, 2012.

[4] BJORKBOM, M., TIMONEN, J., YIGITLER, H., et al. "Localization Services for Online Common Operational Picture and Situation Awareness", *IEEE Access*, v. 1, pp. 742–757, 2013.

[5] GONZALEZ-RUIZ, A., MOSTOFI, Y. "Cooperative Robotic Structure Mapping Using Wireless Measurements: A Comparison of Random and Coordinated Sampling Patterns", *IEEE Sensors Journal*, v. 13, n. 7, pp. 2571–2580, July 2013.

[6] HAMILTON, B. R., MA, X., BAXLEY, R. J., et al. "Propagation Modeling for Radio Frequency Tomography in Wireless Networks", *IEEE Journal of Selected Topics in Signal Processing*, v. 8, n. 1, pp. 55–65, Feb 2014.

[7] MOSHTAGHPOUR, A., AKHAEE, M. A., ATTARIFAR, M. "Obstacle mapping in wireless sensor networks via minimum number of measurements", *IET Signal Processing*, v. 10, n. 3, pp. 237–246, Sep 2016.

[8] BECK, B., MA, X., BAXLEY, R. "Ultrawideband Tomographic Imaging in Uncalibrated Networks", *IEEE Transactions on Wireless Communications*, v. 15, n. 9, pp. 6474–6486, Sep 2016.

[9] CAMPOS, R. S., LOVISOLO, L. *RF Positioning: Fundamentals, Applications and Tools*. 1st ed. Boston, USA, Artech House, 2015.

[10] BAHILLO, A., FERNANDEZ, P., PRIETO, J., et al. "Distance Estimation based on 802.11 RTS/CTS Mechanism for Indoor Localization". In: Miguel Almeida (Ed.), *Advances in Vehicular Networking Technologies*, InTech, cap. 12, Rijeka, Croatia, 2011.

[11] BELL, S., JUNG, W. R., KRISHNAKUMAR, V. "WiFi-based Enhanced Positioning Systems: Accuracy Through Mapping, Calibration, and Classification". In: *Proceedings of the 2nd ACM SIGSPATIAL International Workshop on Indoor Spatial Awareness*, pp. 3–9, San Jose, California, 2010.

[12] CAMPOS, R. S. "Evolution of Positioning Techniques in Cellular Networks, from 2G to 4G", *Wireless Communications and Mobile Computing*, v. 2017, pp. 1–17, January 2017.

[13] CAMPOS, R. S., LOVISOLO, L. "RF Fingerprinting Location Techniques". In: John Wiley and Sons (Ed.), *Handbook of Position Location: Theory, Practice, and Advances*, 1 ed., S. A. Zekavat and R. M. Buehrer, cap. 15, pp. 487–520, Hoboken, NJ, USA, 2011.

[14] GEZICI, S. "A Survey on Wireless Position Estimation", *Wireless Personal Communications: An International Journal*, v. 44, n. 3, pp. 263–282, February 2008.

[15] ZHU, J., DURGIN, G. D. "Indoor/Outdoor Location of Cellular Handsets Based on Received Signal Strength", *Eletronic Letters*, v. 41, n. 1, pp. 24–26, January 2005.

[16] AL KHANBASHI, N., AL SINDI, N., AL-ARAJI, S., et al. "Real time evaluation of RF fingerprints in wireless LAN localization systems". In: *Positioning Navigation and Communication (WPNC), 2013 10th Workshop on*, pp. 1–6, Dresden, Germany, March 2013.

[17] SEIDL, T., KRIEGEL, H.-P. "Optimal Multi-Step K-Nearest Neighbor Search". In: *Proceedings of the 1998 ACM SIGMOD International Conference on Management of Data*, pp. 154–165, Seattle, USA, June 1998.

[18] CAMPOS, R. S., LOVISOLO, L. "A Fast Database Correlation Algorithm for Localization of Wireless Network Mobile Nodes using Coverage Prediction and Round Trip Delay". In: *Proceedings of IEEE 69th Vehicular Technology Conference*, Barcelona, Spain, April 2009.

[19] MAGRO, M. J., DEBONO, C. J. "A Genetic Algorithm Approach to User Location Estimation in UMTS Networks". In: *EUROCON - The International Conference on Computer as a Tool*, pp. 1136–1139, Warsaw, Poland, September 2007.

[20] HATA, M. "Empirical formula for propagation loss in land mobile radio services", *Vehicular Technology, IEEE Transactions on*, v. 29, n. 3, pp. 317–325, 1980.

[21] YOUSSEF, M. A., AGRAWALA, A., UDAYA SHANKAR, A. "WLAN location determination via clustering and probability distributions". In: *Pervasive Computing and Communications, 2003.(PerCom 2003). Proceedings of the First IEEE International Conference on*, pp. 143–150. IEEE, 2003.

[22] BAHL, P., PADMANABHAN, V. N. "RADAR: An in-building RF-based user location and tracking system". In: *INFOCOM 2000. Nineteenth Annual Joint Conference of the IEEE Computer and Communications Societies. Proceedings. IEEE*, v. 2, pp. 775–784, 2000.

[23] B. LI , A. DEMPSTER , C. RIZOS AND J. BARNES. "Hybrid method for localization using WLAN". In: *Proc. Spatial Sci. Conf.*, pp. 341–350, 2005.

[24] CHEN, Y.-C., CHIANG, J.-R., CHU, H.-H., et al. "Sensor-assisted Wi-fi Indoor Location System for Adapting to Environmental Dynamics". In: *Proceedings of the 8th ACM International Symposium on Modeling, Analysis and Simulation of Wireless and Mobile Systems(MSWiM'05)*, pp. 118–125, Montreal, Canada, October 2005.

[25] KING, T., HAENSELMANN, T., EFFELSBERG, W. "On-demand fingerprint selection for 802.11-based positioning systems". In: *International Symposium on a World of Wireless, Mobile and Multimedia Networks (WoWMoM 2008)*, pp. 1–8, Newport Beach, USA, June 2008.

[26] A.M. LADD, K.E. BEKRIS, A. RUDYS, G. MARCEAU, L.E. KAVRAKI AND D.S. WALLACH. "Robotics-based location sensing using wireless Ethernet", *Wireless Networks*, v. 11, n. 1, pp. 189–204, Sep 2005.

[27] STELLA, M., RUSSO, M., BEGUSIC, D. "Location Determination in Indoor Environment based on RSS Fingerprinting and Artificial Neural Network". In: *9th International Conference on Telecommunications (ConTel 2007)*, pp. 301–306, June 2007.

[28] SPIRITO, M. A., CACERES, M., SOTTILE, F. "WLAN-Based Real Time Vehicle Locating System". In: *Proceedings of IEEE 69th Vehicular Technology Conference*, Barcelona, Spain, April 2009.

[29] IEEE COMPUTER SOCIETY. "IEEE Standard for Information Technology - Telecommunications and information exchange between systems - Local and metropolitan area networks - Specific requirements; Part 11: Wireless LAN Medium Access Control (MAC) and Physical Layer (PHY) Specifications". 2007.

[30] KRISHNAKUMAR, A., KRISHNAN, P. "The Theory and Practice of Signal Strength-Based Location Estimation". In: *2005 International Conference on Collaborative Computing: Networking, Applications and Worksharing*, 2005.

[31] CAMPOS, R. S., LOVISOLO, L., DE CAMPOS, M. L. R. "Wi-Fi Multi-floor Indoor Positioning considering Architectural Aspects and Controlled Computational Complexity", *Expert Systems with Applications*, v. 41, n. 14, pp. 6211–6223, 2014.

[32] MENGUAL, L., MARBÁN, O., EIBE, S. "Clustering-based location in wireless networks", *Expert Systems with Applications*, v. 37, n. 9, pp. 6165–6175, 2010.

[33] MENGUAL, L., MARBÁN, O., EIBE, S., et al. "Multi-agent location system in wireless networks", *Expert Systems with Applications*, v. 40, n. 6, pp. 2244–2262, May 2013.

[34] ZHOU, M., TIAN, Z., XU, K., et al. "SCaNME: Location tracking system in large-scale campus Wi-Fi environment using unlabeled mobility map", *Expert Systems with Applications*, v. 41, n. 7, pp. 3429–3443, 2014.

[35] VARSHAVSKY, A., LAMARCA, A., HIGHTOWER, J., et al. "The SkyLoc Floor Localization System". In: *Fifth Annual IEEE International Conference on Pervasive Computing and Communications (PerCom '07)*, pp. 125–134, March 2007.

[36] MOAYERI, N., MAPAR, J., TOMPKINS, S., et al. "Emerging opportunities for localization and tracking", *IEEE Wireless Communications*, v. 18, n. 2, pp. 8–9, 2011.

[37] BAI, Y., JIA, W., ZHANG, H., et al. "Helping the blind to find the floor of destination in multistory buildings using a barometer". In: *Engineering in*

Medicine and Biology Society (EMBC), 2013 35th Annual International Conference of the IEEE, pp. 4738–4741, July 2013.

[38] LEISCH, F., HORNIK, K. "ARC-LH: A new adaptive resampling algorithm for improving ANN classifiers", *Advances in neural information processing systems*, pp. 522–528, 1997.

[39] AL-AHMADI, A. S. M., OMER, A. I., KAMARUDIN, M. R., et al. "Multi-floor indoor positioning system using Bayesian graphical models", *Progress In Electromagnetics Research B*, v. 25, pp. 241–259, 2010.

[40] AL-AHMADI, A., RAHMAN, T., KAMARUDIN, M. R., et al. "Single-phase Wireless LAN Based Multi-floor Indoor Location Determination System". In: *Parallel and Distributed Systems (ICPADS), 2011 IEEE 17th International Conference on*, pp. 1057–1062. IEEE, 2011.

[41] LIU, H.-H., YANG, Y.-N. "WiFi-based indoor positioning for multi-floor environment". In: *TENCON 2011-2011 IEEE Region 10 Conference*, pp. 597–601. IEEE, 2011.

[42] ALSEHLY, F., ARSLAN, T., SEVAK, Z. "Indoor positioning with floor determination in multi story buildings". In: *2011 International Conference on Indoor Positioning and Indoor Navigation (IPIN)*, pp. 1–7, Sept 2011.

[43] MARQUES, N., MENESES, F., MOREIRA, A. "Combining similarity functions and majority rules for multi-building, multi-floor, WiFi positioning". In: *2012 International Conference on Indoor Positioning and Indoor Navigation (IPIN)*, pp. 1–9, Nov 2012.

[44] SUN, L., ZHENG, Z., HE, T., et al. "Multi-Floor Wi-Fi Localization System with Floor Identification", *International Journal of Distributed Sensor Networks*, v. 2015, pp. 1–8, 2015.

[45] THEODORIDIS, S., KOUTROUMBAS, K. *Pattern Recognition*. 4th ed. , Academic Press, 2009.

[46] LIPKUS, A. H. "A proof of the triangle inequality for the Tanimoto distance", *Journal of Mathematical Chemistry*, v. 26, n. 1-3, pp. 263–265, 1999.

[47] DESIENO, D. "Adding a conscience to competitive learning". In: *IEEE International Conference on Neural Networks*, pp. 117–124. IEEE, 1988.

[48] MARSLAND, S. *Machine Learning - An Algorithmic Perspective*. Boca Raton, FL, USA, CRC Press, 2009. pp. 12, 14, 49–50, 207-210, 277–278, 293–314.

[49] HAYKIN, S. *Neural Networks: A Comprehensive Foundation*. 2nd ed. Upper Saddle River, NJ, USA, Prentice Hall PTR, 1998.

[50] SILVA, R. "Improved Self-Organizing Map Performance Applied To Process Monitoring". In: *Proceedings of the Sexto Congreso Interamericano de Computacion Aplicada a La Industria de Procesos*, v. 20, San Andrés Cholula, Puebla, México, 2003.

[51] TWOMEY, J. M., SMITH, A. E., OTHERS. "Committee networks by resampling", *Intelligent Engineering Systems Through Artificial Neural Networks*, v. 5, pp. 153–158, 1995.

[52] RUTA, D., GABRYS, B. "Classifier selection for majority voting", *Information fusion*, v. 6, n. 1, pp. 63–81, 2005.

[53] AL-DAOUD, M. B. "A new algorithm for cluster initialization". In: *WEC'05: The Second World Enformatika Conference*, 2005.

[54] MORÉ, J. J. "The Levenberg-Marquardt algorithm: implementation and theory", *Numerical analysis*, v. 630, pp. 105–116, 1978.

[55] CAMPOS, R. S., LOVISOLO, L., DE CAMPOS, M. L. R. "Search space reduction in DCM positioning using unsupervised clustering". In: *2013 10th Workshop on Positioning Navigation and Communication (WPNC)*, pp. 1–6, Dresden, Germany, March 2013.

[56] KAEMARUNGSI, K., KRISHNAMURTHY, P. "Properties of indoor received signal strength for WLAN location fingerprinting". In: *The First Annual International Conference on Mobile and Ubiquitous Systems: Networking and Services, 2004. MOBIQUITOUS 2004.*, pp. 14–23. IEEE, 2004.

[57] GOLDSMITH, S. F., AIKEN, A. S., WILKERSON, D. S. "Measuring Empirical Computational Complexity". In: *Proceedings of the 6th Joint Meeting of the European Software Engineering Conference and the ACM SIGSOFT Symposium on the Foundations of Software Engineering*, pp. 1–10, Dubrovnik, Croatia, Sep 2007.

[58] CHENG, Y.-C., CHAWATHE, Y., KRUMM, J. "Accuracy Characterization for Metropolitan-Scale Wi-Fi Localization". In: *Proceedings of the 3rd International Conference on Mobile Systems, Applications, and Services*, pp. 233 – 245, Seattle, USA, June 2005.

[59] SUBRAMANIAN, A., DESHPANDE, P., GAOJGAO, J., et al. "Drive-By Localization of Roadside WiFi Networks". In: *The 27th IEEE Conference on Computer Communications (INFOCOM 2008)*, April 2008.

[60] MIKA, S., RATSCH, G., WESTON, J., et al. "Fisher discriminant analysis with kernels". In: *Neural Networks for Signal Processing IX, 1999. Proceedings of the 1999 IEEE Signal Processing Society Workshop*, pp. 41–48, Aug 1999.

[61] ENDSLEY, M. R. "Towards a Theory of Situation Awareness in Dynamic Systems", *Human Factors: The Journal of the Human Factors and Ergonomics Society*, v. 1, n. 37, pp. 32–64, 1995.

[62] MOURIKIS, A. I., ROUMELIOTIS, S. I. "Predicting the Performance of Cooperative Simultaneous Localization and Mapping (C-SLAM)", *Int. J. Rob. Res.*, v. 25, n. 12, pp. 1273–1286, December 2006.

[63] DURRANT-WHYTE, H., BAILEY, T. "Simultaneous localization and mapping: part I", *IEEE Robotics Automation Magazine*, v. 13, n. 2, pp. 99–110, June 2006.

[64] BISSIG, P., WATTENHOFER, R., WELTEN, S. "A pocket guide to indoor mapping". In: *2013 10th Workshop on Positioning Navigation and Communication (WPNC)*, pp. 1–6, Dresden, Germany, March 2013.

[65] RALSTON, T., CHARVAT, G., PEABODY, J. "Real-time through-wall imaging using an ultrawideband multiple-input multiple-output (MIMO) phased array radar system". In: *2010 IEEE International Symposium on Phased Array Systems and Technology (ARRAY)*, pp. 551–558, Oct 2010.

[66] BOREK, S. E. "An Overview of Through the Wall Surveillance for Homeland Security". In: *Proceedings of the 34th Applied Imagery and Pattern Recognition Workshop (AIPR05)*, pp. 1–6, Washington, DC, USA, Dec 2005.

[67] PEABODY, J. E., CHARVAT, G. L., GOODWIN, J., et al. "Through-Wall Imaging Radar", *Lincoln Laboratory Journal*, v. 19, n. 1, pp. 62–72, 2012.

[68] HANSEN, P. C. *Discrete Inverse Problems: Insight and Algorithms*. 1st ed. Philadelphia, USA, Society for Industrial and Applied Mathematics, 2010.

[69] MOSTOFI, Y., GONZALEZ-RUIZ, A. "Compressive cooperative obstacle mapping in mobile networks". In: *MILITARY COMMUNICATIONS CONFERENCE, 2010 - MILCOM 2010*, pp. 524–530, Oct 2010.

[70] MOSTOFI, Y. "Compressive Cooperative Sensing and Mapping in Mobile Networks", *IEEE Transactions on Mobile Computing*, v. 10, n. 12, pp. 1769–1784, Dec 2011.

[71] GONZALEZ, R. C., WOODS, R. E. *Digital Image Processing*. 3rd ed. Upper Saddle River, NJ, Pearson Prentice Hall, 2008. pp. 362–387.

[72] KAK, A. C., SLANEY, M. *Principles of Computerized Tomographic Imaging*. 1st ed. , IEEE Press, 1988.

[73] BRIGGS, W. L., HENSON, V. E. *The DFT: An Owner's Manual for the Discrete Fourier Transform*. 1st ed. Philadelphia, PA, USA, Society for Industrial and Applied Mathematics, 1995. pp. 286–299.

[74] ASTER, R. C., BORCHERS, B., THURBER, C. H. *Parameter Estimation and Inverse Problems*. 1st ed. San Diego, USA, Elsevier Academic Press, 2005.

[75] HANSEN, P. C., SAXILD-HANSEN, M. "AIR Tools - A MATLAB package of algebraic iterative reconstruction methods", *Journal of Computational and Applied Mathematics*, v. 236, n. 8, pp. 2167 – 2178, 2012.

[76] PUCCINELLI, D., HAENGGI, M. "Multipath Fading in Wireless Sensor Networks: Measurements and Interpretation". In: *Proceedings of the 2006 International Conference on Wireless Communications and Mobile Computing*, IWCMC '06, pp. 1039–1044, 2006.

[77] CORKE, P. *Robotics, Vision and Control: Fundamental Algorithms in MATLAB*. 1st ed. , Springer, 2011. Chapter 5.

[78] TURKKA, J., RENFORS, M. "Path loss measurements for a non-line-of-sight mobile-to-mobile environment". In: *8th International Conference on ITS Telecommunications (ITST 2008)*, pp. 274–278, Oct 2008.

[79] INTERNATIONAL TELECOMMUNICATIONS UNION. "Propagation Data and Prediction Models for the Planning of Indoor Radiocommunication Systems and Radio Local Area Networks in the Frequency Range 900 MHz to 100 GHz", *Recommendation ITU-R P.1058-1*, 1997.

[80] TAYLOR, C. D., GUTIERREZ, S. J., LANGDON, S., et al. "Measurement of RF Propagation into Concrete Structures over the Frequency Range 100 MHZ to 3 GHz". In: Reed, J., Rappaport, T., Woerner, B. (Eds.), *Wireless Personal Communications*, v. 377, *The Springer International*

Series in Engineering and Computer Science, Springer US, pp. 131–144, USA, 1997.

[81] PEREZ-VEGA, C., GARCIA, J. L., HIGUERAZ, J. M. L. "A simple and efficient model for indoor path-loss prediction", *Meas. Sci. Technol.*, v. 8, pp. 1166–1173, 1997.

[82] WANG, Z., BOVIK, A. C., SHEIK, H. R., et al. "Image Quality Assessment: From Error Visibility to Structural Similarity", *IEEE Transactions on Image Processing*, v. 13, n. 4, pp. 600–612, April 2004.

[83] MARTINEZ, W. L., MARTINEZ, A. R. *Computational Statistics Handbook with MATLAB*. 1st ed. Boca Raton , Florida, Chapman and Hall/CRC, 2002.

[84] LEWIS, C. Y. C. "Central Slice". 2011. Available[Online]: http://code.google.com/archive/p/centralslice/.

[85] CAMPOS, R. S., LOVISOLO, L., DE CAMPOS, M. L. R. "Physical Modeling of RF Through-the-Wall Mapping using FEM". In: *Proceedings of the 34th Brazilian Telecommunications Symposium - SBrT2016*, Santarém, PA, Brazil, August 2016.

[86] HULT, T., MOHAMMED, A. "Multipath Propagation Assessment for a 2.4 GHz Short-Range Wireless Communication System". In: *IEEE First European Conference on Antennas and Propagation*, pp. 1–5, Nice, France, Nov 2006.

[87] ANASTASSIU, H. T., VOUGIOUKAS, S., FRONIMOS, T., et al. "A Computational Model for Path Loss in Wireless Sensor Networks in Orchard Environments", *Sensors*, v. 1, n. 14, pp. 5118–5135, 2014.

[88] BARKANOV, E. *Introduction to the Finite Element Method*. 1st ed. Riga, Latvia, Institute of Materials and Structures - Faculty of Civil Engineering - Riga Technical University, 2001.

[89] A. TURA. "A Review of Finite Element Analysis Method". 2014. Computer Aided Design Course (Lecture Notes), University of Victoria.

[90] PETRA, C. G., SCHENK, O., LUBIN, M., et al. "An augmented incomplete factorization approach for computing the Schur complement in stochastic optimization", *SIAM Journal on Scientific Computing*, v. 36, n. 2, pp. C139–C162, 2014.

[91] COMSOL. "COMSOL Multiphysics Reference Guide, version 4.3". 2012. Tech. Manual, p. 651.

[92] WILLIAM H. HAYT, J., BUCK, J. A. *Engineering Electromagnetics*. 6th ed. Boston, USA, McGraw-Hill, 2001.

[93] COMSOL. "RF Module User's Guide, version 4.3". 2012. Tech. Manual, p. 31–37.

[94] SAHU, K. N., NAIDU, C. D., SANKAR, K. J. "Study of RF Propagation Losses in Homogeneous Brick and Concrete Walls using Analytical Frequency Dependent Models", *IOSR Journal of Electronics and Communication Engineering (IOSR-JECE)*, v. 9, n. 5, pp. 58–66, Sep-Oct 2014.

[95] VESELOV, A. P. "Huygens Principle". In: Routledge (Ed.), *Encyclopedia of Nonlinear Science*, 1st ed., Alwyn Scott, pp. 429–430, New York, NY, USA, 2005.

[96] BOITHIAS, L. *Radio Wave Propagation*. 1st ed. London, McGraw-Hill, 1987.

[97] ZALI, H. M., ALI, M. T., PASYA, I., et al. "Design of a Cylindrical Parabolic Reflector on Monopole Plasma Antenna". In: *Proceedings of IEEE International RF and Microwave Conference*, pp. 344–348, Penang, Malaysia, Dec 2013.

[98] STUTZMAN, W. L., THIELE, G. A. *Antenna Theory and Design*. 3rd ed. , Wiley, 2013.

[99] ANDREW. "Andrew Catalog 38-2001". 2001. pg. 52, Available[Online]: http://www.andrew.com.

[100] ZOSSO, D., CUADRA, M. B., THIRAN, J.-P. "Direct Fourier Tomographic Reconstruction Image-to-Image Filter", *The Insight Journal*, v. July-Dec, pp. 1–13, August 2007.

[101] MATHWORKS. "interp - Increase sampling rate by an integer factor (interpolation)". 2017. Available[Online]: http://www-rohan.sdsu.edu/doc/matlab/toolbox/signal/interp.html.

[102] INTERNATIONAL TELECOMMUNICATIONS UNION. "Evaluating fields from terrestrial broadcasting transmitting systems operating in any frequency band for assessing exposure to non-ionizing radiation", *Recommendation ITU-R BS.1698*, 2005.

[103] SAHOO, P. K., SOLTANI, S., WONG, A. K. C. "A Survey of Thresholding Techniques", *Computer Vision, Graphics, and Image Processing*, v. 41, n. 2, pp. 233–260, 1988.

[104] OTSU, N. "A Threshold Selection Method from Gray-Level Histograms", *IEEE Transaction on Systems, Man, and Cybernetics*, v. SMC-9, n. 1, pp. 62–66, January 1979.

[105] KAPUR, J. N. "A New Method for Gray-Level Picture Thresholding Using the Entropy of the Histogram", *Computer Vision, Graphics, and Image Processing*, v. 29, n. 3, pp. 273–285, 1985.

[106] CHOW, C. K., KANEKO, T. "Automatic Boundary Detection of the Left Ventricle from Cineangiograms", *Computers and Biomedical Research*, v. 5, n. 4, pp. 388–410, 1972.

[107] POLLAK, I., WILLSKY, A. S., KRIM, H. "Image Segmentation and Edge Enhancement with Stabilized Inverse Diffusion Equations", *IEEE Transactions on Image Processing*, v. 9, n. 2, pp. 256–266, February 2000.

[108] DAVIS, J. *ASM Specialty Handbook - Carbon and Alloy Steels*. Metals Park, OH, USA, ASM International, 1996.

[109] CHEN, M., SOHN, T., CHMELEV, D., et al. "Practical Metropolitan-Scale Positioning for GSM Phones". In: *Proceedings of 8th International Conference on Ubiquitous Computing*, pp. 225–242, Newport Beach, USA, September 2006.

[110] YAN, Y., MOSTOFI, Y. "Impact of Localization Errors on Wireless Channel Prediction in Mobile Robotic Networks". In: *Proceedings of 2013 IEEE Globecom Workshops*, pp. 1–6, Atlanta, USA, December 2013.

[111] CHLAMTAC, I., CONTI, M., LIU, J. J.-N. "Mobile ad hoc networking: imperatives and challenges", *Ad Hoc Networks*, v. 1, pp. 13–64, 2003.